ORNL/SPR-2014/532

Electrical and Electronics Systems Research Division

Oak Ridge National Laboratory Annual Progress Report for the Power Electronics and Electric Motors Program

Burak Ozpineci, Program Manager

November 2014

OAK RIDGE NATIONAL LABORATORY
MANAGED BY UT-BATTELLE FOR THE US DEPARTMENT OF ENERGY

US Department of Energy
Office of Vehicle Technologies, EE-2G
1000 Independence Avenue, S.W.
Washington, D.C. 20585-0121

FY 2014

Oak Ridge National Laboratory Annual Progress Report for the Power Electronics and Electric Motors Program

Prepared by:

Oak Ridge National Laboratory

Burak Ozpineci, Program Manager

Submitted to:

Energy Efficiency and Renewable Energy
Vehicle Technologies Office

Susan A. Rogers, Technology Development Manager

November 2014

CONTENTS

ACRONYMS AND ABBREVIATIONS

3D	three dimensional
ac	alternating current
A	ampere
AEV	all electric vehicle
Al	aluminum
AM	Additive manufacturing
APEEM	Advanced Power Electronics and Electric Motors (program, DOE)
APEEM	Advanced Power Electronics and Electric Machinery (subprogram, ORNL)
AWG	American wire gauge
BCC	body center cubic
BFE	brushless field excitation
CAD	computer-aided design
CAN	controller area network
CVD	chemical vapor deposition
DBC	direct bond copper
dc	direct current
DMLS	direct-melted laser-sintered
DOE	US Department of Energy
DSP	digital signal processing/processor
EMI	electromagnetic interference
EV	electric vehicle
FDM	fused deposition melting
FEA	finite element analysis
FET	field effect transistor
GaN	gallium nitride
HEV	hybrid electric vehicle
HR	high resolution
HSG	hybrid starter-generator
HV	high voltage
IGBT	insulated gate bipolar transistor
INC/CONV	inverter/converter
IPM	integrated power module
IR	insulation resistance
IR	International Rectifier
JBS	junction barrier Schottky
JFE	JFE Steel Corporation

JFET	junction field-effect transistor
K	thermal conductivity
K	degrees Kelvin
MC	Monte Carlo
M/G	motor/generator
MOSFET	metal oxide semiconductor field-effect transistor
MPH	miles per hour
Nd	neodymium
NREL	National Renewable Energy Laboratory (DOE)
OBC	onboard charger
OD	outer diameter
OEM	original equipment manufacturer
ORNL	Oak Ridge National Laboratory
PBA	planar bond-all
PCB	printed circuit board
PCU	power converter unit
PD	power density (peak)
PE	power electronics
PEV	plug-in electric vehicle
PF	power factor
PFC	power factor correction
PI	proportional integral
PID	proportional integral derivative
PM	permanent magnet
PWM	pulse width modulated/modulation
R&D	research and development
rms	root mean square
SBD	Schottky barrier diode
SDSR	sinusoidally driven synchronous reluctance
SEM	scanning electron microscope
Si	silicon
SiC	silicon carbide
SOI	silicon-on-insulator
SP	specific power
SRM	switched reluctance motor
TC	thermal conductivity
TDS	traction drive system

THD	total harmonic distortion
U.S. DRIVE	Driving Research and Innovation for Vehicle efficiency and Energy sustainability (cooperative research effort between DOE and industry partners)
V	volt
Vac	volts of alternating current
Vce	voltage across collector and emitter
Vdc	volts of direct current (operating voltage)
VTO	Vehicle Technologies Office (DOE)
WBG	wide bandgap
ZS	zero sequence
ZSIN	zero sequence impedance network

I. INTRODUCTION

The US Department of Energy (DOE) announced in May 2011 a new cooperative research effort comprising DOE, the US Council for Automotive Research (composed of automakers Ford Motor Company, General Motors Company, and Chrysler Group), Tesla Motors, and representatives of the electric utility and petroleum industries. Known as U.S. DRIVE (Driving Research and Innovation for Vehicle efficiency and Energy sustainability), it represents DOE's commitment to developing public–private partnerships to fund high-risk–high-reward research into advanced automotive technologies. The new partnership replaces and builds upon the partnership known as FreedomCAR (derived from "Freedom" and "Cooperative Automotive Research") that ran from 2002 through 2010 and the Partnership for a New Generation of Vehicles initiative that ran from 1993 through 2001.

Oak Ridge National Laboratory's (ORNL's) Advanced Power Electronics and Electric Motors (APEEM) subprogram within the DOE Vehicle Technologies Office (VTO) provides support and guidance for many cutting-edge automotive technologies now under development. Research is focused on developing revolutionary new power electronics (PE), electric motor, and traction drive system (TDS) technologies that will leapfrog current on-the-road technologies, leading to lower cost and better efficiency in transforming battery energy to useful work. The research and development (R&D) is also aimed at achieving a greater understanding of and improvements in the way the various new components of tomorrow's automobiles will function as a unified system to improve fuel efficiency through research in more efficient TDSs.

In supporting the development of advanced vehicle propulsion systems, the APEEM subprogram fosters the development of technologies that will significantly improve efficiency, costs, and fuel economy.

The APEEM subprogram supports the efforts of the U.S. DRIVE partnership through a three-phase approach intended to

- identify overall propulsion- and vehicle-related needs by analyzing programmatic goals and reviewing industry recommendations and requirements, and then develop and deliver the appropriate technical targets for systems, subsystems, and component R&D activities
- develop, test, and validate individual subsystems and components, including electric motors and PE
- estimate how well the components and subsystems work together in a vehicle environment or as a complete propulsion system and whether the efficiency and performance targets at the vehicle level have been achieved

The research performed under this subprogram addresses the technical and cost barriers that currently inhibit the introduction of advanced propulsion technologies into hybrid electric vehicles (HEVs), plug-in HEVs (PEVs), all-electric vehicles (AEVs), and fuel-cell-powered automobiles that meet the goals set by U.S. DRIVE.

A key element in making these advanced vehicles practical is providing an affordable electric TDS. This will require attaining weight, volume, efficiency, and cost targets for the PE and electric motor subsystems of the TDS. Areas of development include

- novel traction motor designs that result in increased power density and lower cost
- inverter technologies that incorporate advanced semiconductor devices to achieve higher efficiency while accommodating higher-temperature environments and delivering higher reliability
- converter concepts that leverage higher-switching-frequency semiconductors, nanocomposite magnetics, higher-temperature capacitors, and novel packaging techniques that integrate more functionality into applications offering reduced size, weight, and cost
- new onboard battery charging electronics that build from advances in converter architectures for decreased cost and size

- more compact and higher-performing thermal controls achieved through novel thermal materials and innovative packaging technologies
- integrated motor-inverter TDS architectures that optimize the technical strengths of the underlying PE and electric machine subsystems.

ORNL's APEEM research program conducts fundamental research, evaluates hardware, and assists in the technical direction of the VTO APEEM program and in setting national policy for future AEVs that addresses the overarching goal of petroleum and greenhouse gas reduction. In this role, ORNL serves on the U.S. DRIVE Electrical and Electronics Technical Team, evaluates proposals for DOE, and lends its technological expertise to the direction of projects and evaluation of developing technologies. ORNL also executes specific projects for DOE.

DOE's continuing R&D into advanced vehicle technologies supports the administration's goal to produce a five-passenger affordable AEV with a payback of less than 5 years and sufficient range and fast charging capability to enable average Americans everywhere to meet their daily transportation needs more conveniently and at lower cost by the year 2022.

Research Highlights

Task 2: Systems Research and Development

Task 2.1 Benchmarking EV and HEV Technologies

- Overall: Conducted thorough benchmark assessments and reported on many HEV/electric vehicle (EV) technologies:
  - 2004 Prius, 2006 Accord, 2007 Camry, 2008 Lexus LS 600h, 2010 Prius, 2011 Hyundai Sonata inverter/motor, 2012 Nissan LEAF inverter/motor, 2012 Hyundai Sonata hybrid starter-generator, 2013 Nissan LEAF charger, and 2014 Honda Accord (in progress).
- FY 2014
  - Continued and finalized assessments and testing/evaluation of the 2013 Nissan LEAF 6.6 kW on-board charger (OBC).
  - Conducted thorough teardown assessments of 2014 Honda Accord power converter unit and transmission/transaxle (includes electric motor and generator).
  - Initiated dynamometer testing of the 2014 Honda Accord inverter and motor.

Task 3: Power Electronics Research and Development

Task 3.1 Power Electronics Packaging

- Delivered first-generation silicon carbide (SiC) integrated power modules (IPMs) for system evaluation, leading to 30% overall volume and weight reductions.
- Developed an integrated cooling SiC 100 A/1200 V phase-leg module that enables 3× current density increases over its conventional silicon (Si) counterpart, resulting from a 35% reduction in the die size; 40 and 80% reductions in conduction and switching power losses, respectively; and a 35% reduction in package thermal resistance.
- Developed an innovative planar-bond-all SiC package that
  - integrates double-sided direct cooling that is 40% more efficient
  - realizes 3-dimensional planar interconnection with a 75% reduction in parasitic electrical inductance and a 90% reduction in resistance
  - incorporates advanced low-cost manufacturing
  - allows converter/inverter system-level functional integration

Task 3.2 Power Electronics Inverter R&D

- Acquired, tested, and characterized SiC metal oxide semiconductor field-effect transistors, an SiC junction field-effect transistor, and SiC junction barrier Schottky diodes.

- Completed the design, build, and testing of an all-SiC 10 kW inverter using a state-of-the-art commercial all-SiC module.

Task 3.3 Innovative Technologies for dc-dc Converters and On-board Chargers

- Characterized 1200 V/100 A SiC switch phase-leg modules developed in FY 2013 for use in the development of a 6.6 kW OBC prototype.
- Completed the design and fabrication of a 6.6 kW isolation converter using the ORNL-designed SiC phase-leg modules and planar ferrite cores.
- Completed tests of the 6.6 kW SiC-based isolation converter that showed a measured peak efficiency of 99.0%.
- Tested and characterized 600 V gallium nitride switches for use in on-board charger converter designs.
- Completed tests of a baseline 5.8 kW Si-based integrated charger that integrates the segmented traction drive, 14 V dc-dc converter, and high-voltage battery charger dc-dc converter. It showed a peak efficiency of 94.6 % when charged from a 240 V source and 92.0 % when charged from a 120 V source.

Task 4: Electric Motor Research and Technology Development

Task 4.1 Scalable Non–Rare Earth Electric Motor Development

- Machine design and development
  - Originated and designed two different novel machines (with several sub-designs of each)
  - Identified brushless field excitation and synchronous reluctance motor designs through modeling as high-potential candidates to meet targets.
  - Selected novel synchronous reluctance machine for fabrication.
- Material research and development
  - Continued research on electrical sheet steel with high silicon content (>6%).
  - Confirmed capability for ingot-based processing versus an expensive chemical vapor deposition process.
  - Developed and confirmed a novel processing technique to reduce brittleness; otherwise the workability of high-silicon steel is not suitable for mass production of motor laminations.
  - Developed new magnetic material characterization systems for innovative analysis of electrical steel magnetic properties.
- Advanced modeling
  - Incorporated findings from research on soft magnetic materials properties, using the new characterization system, into electromagnetics modeling.
  - Developed detailed micromagnetics code and a corresponding simulation environment to study the fundamental behavior and impact of various conditions upon magnetization and loss characteristics of electrical steel.
- Proof-of-principle fabrication and bench top testing
  - Fabricated a proof-of-principle prototype and began benchtop testing to verify basic parameters of the electromagnetic model.

II. RESEARCH AREAS

2.1 Benchmarking EV and HEV Technologies

Tim Burress (Principal Investigator)

Oak Ridge National Laboratory
National Transportation Research Center
2360 Cherahala Boulevard
Knoxville, TN 37932
Phone: (865) 946-1216; Fax: (865) 946-1262
E-mail: burressta@ornl.gov

Burak Ozpineci, ORNL APEEM Program Manager
Phone: (865) 946-1329; Fax: (865) 946-1262
E-mail: burak@ornl.gov

Susan A. Rogers, DOE APEEM Program Manager
Phone: (202) 586-8997; Fax: (202) 586-1600
E-mail: Susan.Rogers@ee.doe.gov

Start Date: October 2013
Projected End Date: Ongoing

Objectives

- Benchmark hybrid electric vehicle (HEV) and electric vehicle (EV) components.
  - Assess design, packaging, and fabrication innovations in subsystems and components.
    - Determine techniques used to improve specific power and power density and reduce cost.
    - Perform compositional analysis of key components.
  - Examine performance and operational characteristics during comprehensive tests and evaluations.
    - Obtain peak torque and power capability.
    - Identify detailed information regarding time-dependent and condition-dependent operation.
  - Compile information from evaluations and assessments.
    - Identify new areas of interest.
    - Compare results with other EV/HEV technologies and DOE targets.

Technical Barriers

- Integrating custom ORNL inverter-motor-controller with original equipment manufacturer (OEM) components.
  - Optimizing controls for nonlinear motors throughout operation range.
- Intercepting, decoding, and overtaking OEM controller area network signals.
- Adapting nonstandard motor shaft and assembly to dynamometer and test fixture.

Technical Targets

- This project helps with program planning and the establishment and verification of all DOE 2020 targets.

Accomplishments

- Overall: Conducted thorough benchmark assessments and reported on many HEV/EV technologies.
  - 2004 Prius, 2006 Accord, 2007 Camry, 2008 Lexus LS 600h, 2010 Prius, 2011 Hyundai Sonata inverter/motor, 2012 Nissan LEAF inverter/motor, 2012 Hyundai Sonata hybrid starter-generator (HSG), 2013 Nissan LEAF charger, and 2014 Honda Accord (in progress).
- FY 2014
  - Continued and finalized assessments and testing/evaluation of the 2013 Nissan LEAF 6.6 kW on-board charger (OBC).
  - Conducted thorough teardown assessments of 2014 Honda Accord power converter unit (PCU) and transmission/transaxle (includes electric motor and generator).
  - Initiated dynamometer testing of the 2014 Honda Accord inverter and motor.

✧ ✧ ✧ ✧ ✧

Introduction

Automotive manufacturers usually do not publish details about the design, functionality, and operation of EV/HEV technologies, and even published performance specifications need to be verified and clarified. For example, single-value power ratings for motors and inverters are often published; but they do not include information about the power capability throughout the operation range (e.g., versus speed), the duration for which this power can be maintained, the efficiency throughout the operation region, and many other important characteristics. Therefore, ORNL performs teardown assessments to obtain comprehensive information on design, functionality, and subcomponent characteristics. Furthermore, components are completely instrumented and tested in a dynamometer test cell to determine operational characteristics such as performance and efficiency.

These benchmarking activities play an important role in program planning efforts by defining the current state of the art for components and subsystems, defining performance and design metrics for DOE's competitive research and

development (R&D) efforts, and identifying technology gaps to provide guidance for future research focus areas. To establish practical targets, the baseline technological status must be obtained from subsystems currently in the marketplace. Therefore, benchmarking cutting-edge technologies in competitive global markets establishes a solid technology baseline for the DOE APEEM program. It also assists in determining whether performance goals established for the program are realistically achievable and present sufficient challenge to warrant a robust program.

Benchmarking activities also ensure that the DOE APEEM program will not duplicate technical innovations found in commercially available technologies. They provide technical insight, allowing the DOE program to move more rapidly by maintaining awareness of current trends and technical innovations in advancing on-the-road technologies. Findings and results from the benchmarking efforts are detailed in reports and presentations. These publications are frequently cited in technical conference papers and have a high level of recognition among industry, academia, and enthusiasts.

Approach

The general approach for benchmarking HEV and EV components is shown in Figure 1. Appropriate components are selected by DOE based on information from the Internet, technical publications, published specifications, and feedback from US automotive manufacturers and suppliers. After benchmarking of the 2012 Hyundai Sonata HSG/inverter and teardown of the 2013 Toyota Camry PCU were completed in FY 2013, initial assessment of the 2013 Nissan LEAF charger began in the latter part of FY 2013. Detailed testing and analysis of the 2013 Nissan LEAF was conducted in the first half of FY 2014. Some research was conducted on the 2014 Honda Accord in the first half of FY 2014, but because of the unavailability of parts, much of the benchmarking effort on the 2014 Accord occurred in the second half of FY 2014. The approach and findings from the 2013 Nissan LEAF charger and 2014 Honda Accord inverter/motor benchmarking are discussed in the following sections.

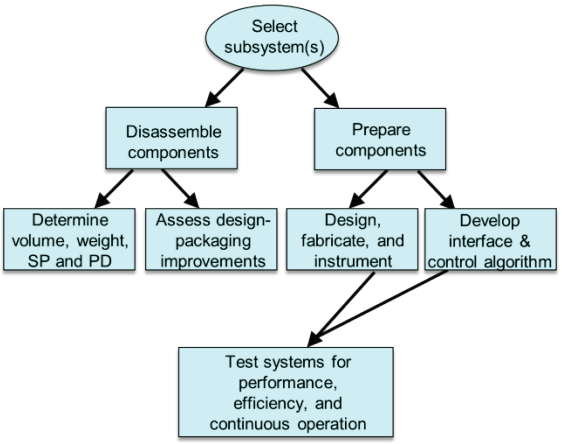

Figure 1: General approach for benchmarking components.

Results

2013 Nissan LEAF Charger

With the recent advent of the first mass-produced full EV, the Nissan LEAF, it is important to note that the OBC is a critical component that impacts overall efficiency and the cost of operating the vehicle. The charger requires several power stages and many components, so there are significant associated cost and design requirements. The Nissan LEAF inverter and motor were benchmarked by ORNL in FY 2012 and the results published. The 2012 LEAF includes a 3.3 kW OBC, and the 2013 LEAF upgraded to a 6.6 kW charger, both of which accept ac power in standard forms (i.e., 120 and 240 V). A separate "fast-charging" port is available that accepts dc power from a large off-board charger.

The focus of DOE's APEEM program is on components and subsystems; therefore, the entire vehicle was not procured and used during analyses of the LEAF's OBC. Various standards (namely SAE J1772) are in place to regulate charger functionality and impact on grid power quality. Since harmonic analysis for total harmonic distortion and other metrics related to standards requires the entire system, ORNL focused on obtaining design, functionality, and operational characteristics at a detailed subsystem level. Doing so required destructive teardown and invasive investigations to determine the layout and connectivity of all items in the charger. ORNL evaluated the operation of converter stages by implementing custom-developed control algorithms, and some information from FY 2013 is reviewed before detailed results are given.

Design and functionality assessments

The 2013 Nissan LEAF charger is shown on the upper left in Figure 2. As received, the mass of the charger was about 16.3 kg, which includes the mass of the external off-white line filter and its support bracket weighing a total of 3.2 kg. The main charger assembly width and length are about 9.9 and 10.9 in., and the height varies from about 3 to 4.5 in., giving a volume of approximately 11.1 L. Using these metrics with a power rating of 6.6 kW, the specific power and power density are 0.4 kW/kg and 0.6 kW/L, respectively. These figures seem quite low, but it should be noted that the charger can operate continuously at a power level of 6.6 kW, and isolation and power quality specifications required by standards ultimately require additional components.

The underside of the charger assembly is also shown in Figure 2, where cast (then machined) aluminum channels for liquid cooling with a water ethylene-glycol mixture are visible. The internal compartment includes a control-communication circuit board, a driver and signal conditioning board, a black power module, large passive components for various power stages, and many smaller devices and peripheral passive components. The control board includes a Renesas R5F71476FPV microcontroller, the type of microcontroller used for the Nissan LEAF motor controller.

The block diagram in Figure 2 describes the various stages of the OBC and indicates where the associated devices are located in the power module. The corresponding circuit schematic is shown in Figures 3 and 4. Note that the latter two figures are actually one schematic, but they are

separated for image clarity. Also note there is only one 310 V/1 uF and 420 V/2700 uF capacitor in the circuit, but it is shown in both figures as a reference item. After the external line filter, the ac input of the charger is fused and additional filtering (including common mode) is applied with relatively small passive components. A relay remains open until ac voltage has been applied for a certain amount of time, to avoid high in-rush currents by charging the system capacitors through three resistors. The first conversion stage of the charger is a conventional rectifier with four diodes. The next stage is a boosting power factor correction (PFC) stage, which includes three metal oxide semiconductor field-effect transistors (MOSFETs) in parallel for chopping action. It also includes two diodes in parallel to prevent reverse current and to allow energy to be stored in the inductor as the MOSFETs are active. The boosted voltage is regulated to between ~360 and 400 V, and a large 420 V/ 2700 uF electrolytic capacitor is located at the boosted output.

The final stages of the charger, shown in Figure 4, include an H-bridge inverter with two MOSFETS for each switch and one small anti-parallel diode for each switch. The inverter drives the primary coil of the large isolation transformer, which has two secondary windings. Output from the two secondary windings is fed to two full-bridge rectifiers, with outputs placed in series and balancing diodes in parallel with each rectifier. In total, ten diodes are located in the final rectification stage. The rectified output is fed through two large inductors, a diode (not located in the power module), a common mode filter, and small passive filters before passing through the output connector that connects to the battery.

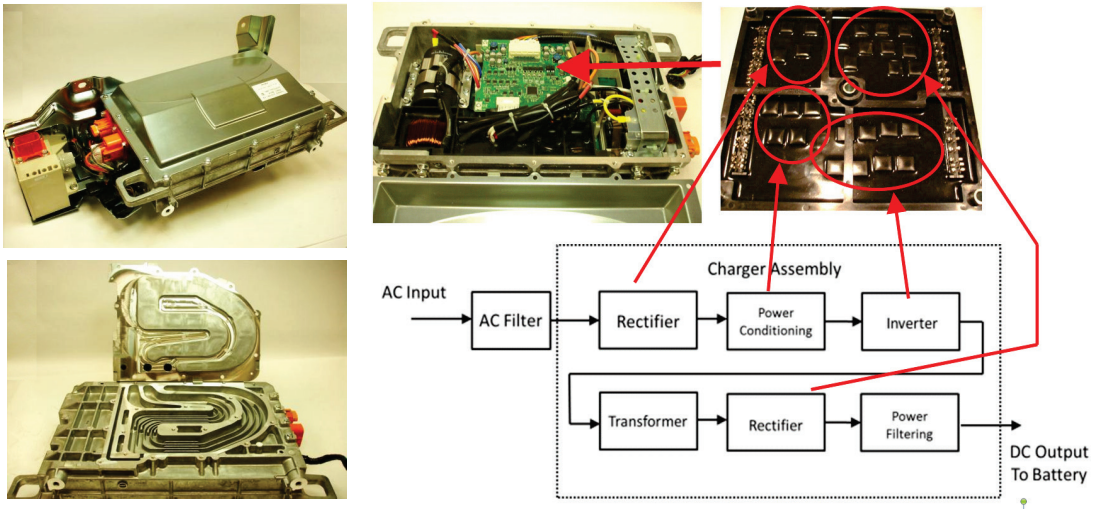

Figure 2: Nissan LEAF charger ac input and boost-PFC.

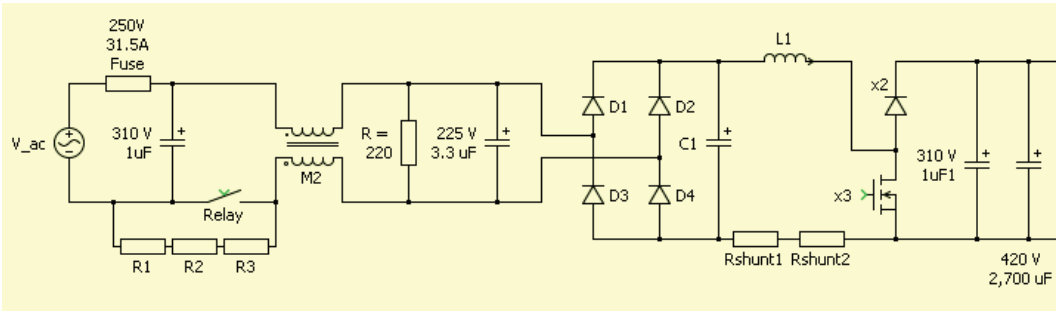

Figure 3: Nissan LEAF charger ac input and boost-PFC.

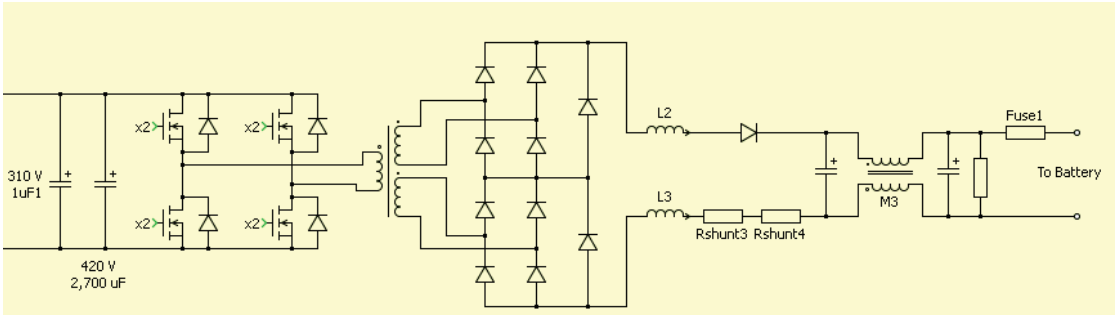

Figure 4: Nissan LEAF charger isolation and rectification stage.

The battery voltage varies with the state of charge; therefore, the output voltage of the charger must have a fairly wide range to maintain a constant charging power level and avoid overcharging conditions. It can be roughly estimated that the charger output voltage is in the range of 300–400 V for normal charging conditions.

Testing and characterization

In carrying out basic operational tests, it was discovered that the driver circuitry for the H-bridge inverter is relatively unconventional: the MOSFETs are controlled with only the power isolation transformer, and no additional control signal isolation (i.e., optocoupler) is used. This is possible largely because the H-bridge can be controlled with phase-shift control. Additionally, it appears that the dead-time is generated on the output of the secondary with passive components. The PFC chopper is operated at a frequency of about 30 kHz, and the input current is limited at about 2 Arms.

The image shown in Figure 5 displays the operational waveforms of the PFC during testing at a power level of 2.6 kW. The waveforms indicate high power factors with notable stability at the zero crossing, which can be a challenging area in which to maintain stability for PFC operation. The efficiency of the boost-PFC stage at a power level of 3.3 kW is about 92.1 and 96.5%, for 120 and 240 V input voltages, respectively. Similar waveforms are shown in Figure 6 for operation at 5.6 kW. For operation at 6.6 kW, the boost-PFC efficiency is about 96.5%. This power level is achievable only at 240 V because of the common residential current availability for 120 V receptacles.

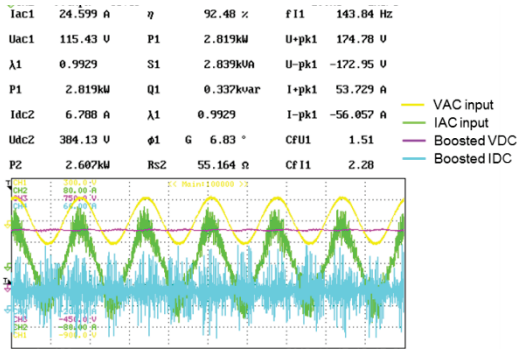

Figure 5: Power analyzer screenshot during PFC testing at 3.3 kW.

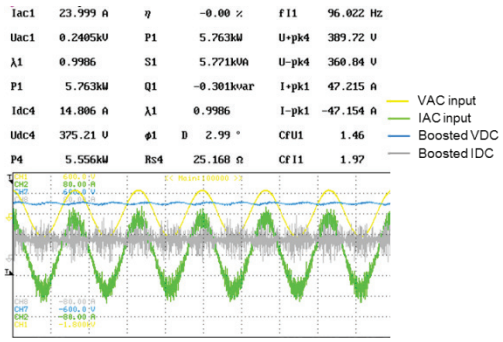

Figure 6: Power analyzer screenshot during PFC testing at 6.6 kW.

The graph in Figure 7 indicates the PFC efficiency versus dc output power for 120 and 240 V operation. It is clear that operation at 120 V correlates with efficiencies between 92 and 92.5% over the range of operation. Operation at 240 V correlates with an efficiency of 96 to 96.5% for all power levels above 3 kW. A similar graph is shown in Figure 8, where the power factor is plotted versus dc power for 120 and 240 V operation. The power factor is very high for 120 V operation and low power levels, but it quickly drops to about 0.92 as the power increases from about 2.5 to 3.3 kW. Operation at 240 V results in a gradual increase in the power factor from roughly 0.98 at 2.5 kW, approaching 1 near operation at 6 kW.

Test results indicate that the efficiency of the final charger stage is about 94% at 3.3 kW and 120 V and about 95% at 6.6 kW for 240 V operation. This yields a total system efficiency of about 87% for operation at a power level of 3.3 kW and 120 V and about 91.5% for operation at 6.6 kW and 240 V. Since the operation of the charger is largely dependent on battery characteristics and OEM controls, as the charger is operating with the battery pack, ORNL has worked with other organizations that perform full-vehicle assessments to verify and analyze in situ operational characteristics. However, the invasive effort required to obtain this information creates a difficulty: there is some risk of compromising vehicle integrity/value, and most test vehicles are borrowed or will be used in company fleets. Nonetheless, system-level efficiencies are easier to obtain. Argonne National Laboratory performed full-vehicle testing and reports that the 3.3 kW 2012 LEAF charger and EV service equipment have a total efficiency of about 86.3%, which is the efficiency from the ac receptacle to the dc power input to the battery. This is in close agreement with the measurements described above.

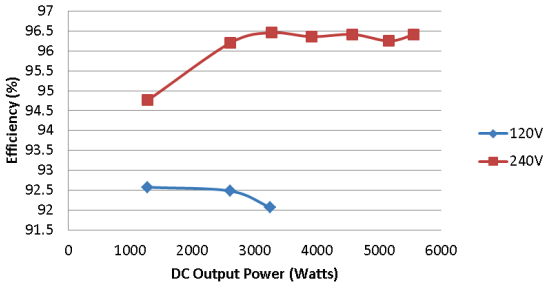

Figure 7: Nissan LEAF charger PFC efficiency vs dc power.

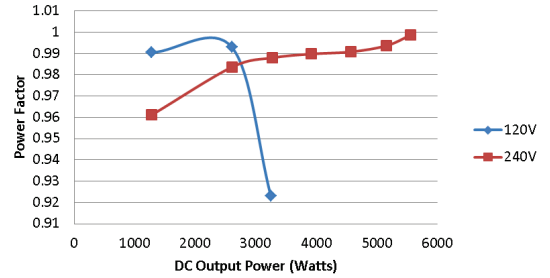

Figure 8: Nissan LEAF Charger PFC power factor vs dc power.

2014 Honda Accord PCU and Transmission/Transaxle

Honda was one of the first automotive manufacturers to mass-produce and sell hybrid vehicles in the United States. However, all of the mass-produced hybrid systems have been mild hybrids, with the electric portion of the powertrain operating at a power level of 14 kW or less. For model year 2014, Honda offered a full hybrid powertrain (termed the "Earth Dreams" hybrid system), one without plug-in and one with plug-in capability for recharging the battery. The 2014 plug-in HEV (PEV) had limited production numbers and was largely sold only in California and New York, where tax incentives were higher. The limited number of these vehicles caused significant difficulty and unexpected delays in obtaining PEV parts, of which the OBC was of particular interest. However, 2014 Accord HEV components were also of significant interest, as the motor has the same published power rating of 124 kW for both HEV and PEV powertrains.

Published specifications indicate that the PEV has a 6.7 kWh battery pack, compared with a 1.3 kWh rating for the HEV version, both with a published maximum output of 41 kW. The nominal battery pack voltages for the PEV and HEV are 320 and 259.2 V, respectively. The published engine maximum power rating is 105 kW, and the total system power is reported to be 146 kW, which is the sum of the maximum engine power and the maximum battery power. A detailed teardown and benchmarking analysis of the 2014 Honda Accord hybrid system was conducted, and dynamometer testing began in FY 2014.

The 2014 Accord transmission (Figure 9), has a total mass of about 113.5 kg (249.5 lb), quite close to that of the 2007 Camry hybrid transmission mass of 108 kg. This is a good comparison because both passenger vehicles are sedans of similar size and power requirements. As is the case for many hybrid transmissions, there is no torque converter between the internal combustion engine and the transmission. Other than the absence of a torque converter, the transmission mounts to the engine in a conventional manner with a flywheel attached to the spline. Various sections of the transmission are indicated in Figure 10, in which the engine input spline shafted is indicated. The gear section is adjacent to the engine mounting location, and it includes the differential gear that drives the left and right drive shafts and ultimately the front wheels. The section that houses the drive motor is located next to the gear section, and the generator section is located next to the motor section on the end of the transmission. The image in Figure 11 offers another view of the three primary sections of the transmission, as well as external components such as the motor terminals, resolver connectors, and clutch solenoid valves.

After the end plate of the generator section is removed, the generator is clearly visible, as shown in Figure 12. The generator end plate includes a position resolver that has 14 stator teeth, and the generator shaft has a soft-magnetic resolver rotor with four smooth lobes consisting of 8 laminations for position sensing. Also indicated in Figure 12 are four tubes used for oil spray cooling of the generator and motor end windings. The image on the right of Figure 12 shows one of the tubes after removal. Four groups of two holes are positioned so that they spray the end turns on both sides of the generator and motor. Since the generator is smaller than the motor, the two groupings for the generator are closer together than those for the motor spray holes. After the generator is removed, a clutch located between the generator and the motor is visible (Figure 13). The clutch does not have hydraulic activation and is used only as a torque limiter, most likely to mitigate transients and peak conditions when the generator is used to start the engine.

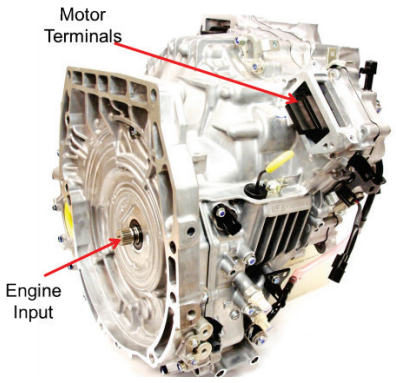

Figure 9: 2014 Honda Accord transmission.

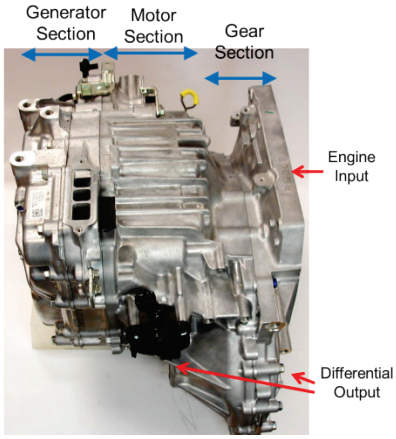

Figure 10: Sections of the 2014 Honda Accord transmission.

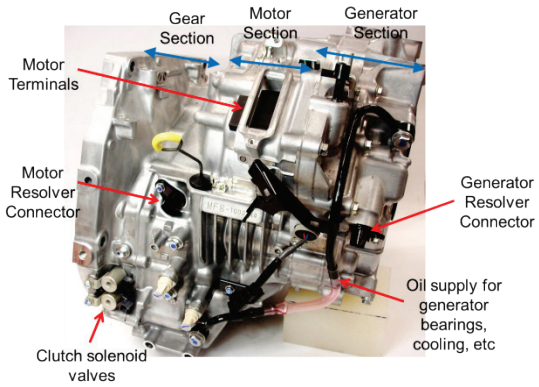

Figure 11: Sections and various exterior components of the 2014 Honda Accord transmission.

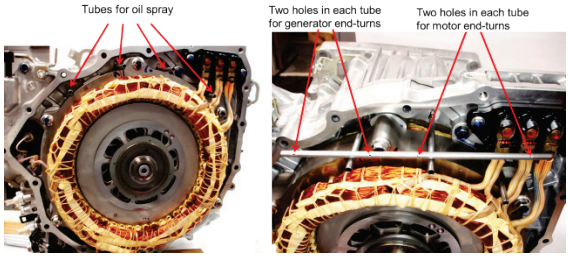

Figure 12: 2014 Accord transmission motor and generator oil spray cooling.

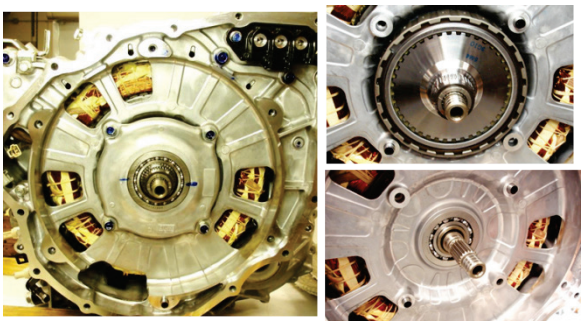

Figure 13: 2014 Accord torque-limiting clutch between engine and generator.

One side of the torque-limiting clutch is connected to the generator, and the other side is connected to a long shaft, shown in Figure 14, that feeds through the hollow motor rotor shaft and ultimately into the gear section of the transmission. At the end of the long generator clutch shaft, a small helical gear mates with a gear fixed to the splined engine input shaft, which is shown on the left in Figure 14. Additional components in the gear section include a large differential gear, a drive gear, an overdrive clutch, and a small motor gear. The image on the right in Figure 14 shows the gear section with the generator shaft removed so that the small motor gear is visible. Additionally, the overdrive clutch and engine input spline shaft/gear that mates with the generator shaft have been removed.

During normal operation, the Accord hybrid system operates as a series hybrid, in which power from the engine is absorbed by the generator and passed to the battery and the electric motor for vehicle propulsion. However, at high speeds, the overdrive clutch engages the engine to the drive wheels through a fixed gear ratio. With the overdrive clutch removed, as shown in Figure 14, the gear that mates the engine to the drive gear (when the clutch is activated) is visible. The number of gear teeth on each gear is indicated in Figure 15. The differential gear has 65 teeth, the driven gear has 39, the drive gear has 49, the clutched generator shaft has 34, the electric motor output shaft has 20, the clutched engine output has 61, and the engine input gear that mates with the generator gear has 66. Neglecting occasional slippage in the torque-limiting clutch, the generator rotational speed is 1.94 times faster than that of the engine.

Considering the OEM tire size, the differential axle rpm is about 13 times the vehicle speed in miles-per-hour (MPH). The total gear ratio from the electric motor to the differential output is 8.38; therefore, the rated motor speed of 14,000 rpm correlates with a vehicle speed of about 128 MPH. The common vehicle speed of 60 MPH correlates with an electric motor speed of about 6500 rpm. When the overdrive clutch is active, the gear ratio from the engine to the differential output is about 2.75, so engine speeds of 2000 rpm and 4000 rpm correlate with a vehicle speed of 66 MPH and 112 MPH, respectively.

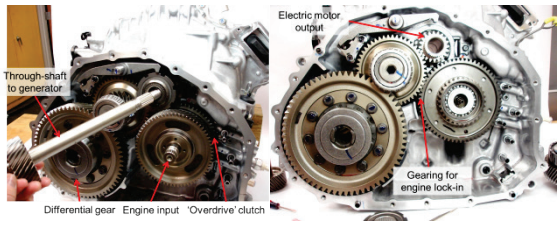

Figure 14: 2014 Accord transmission gear section.

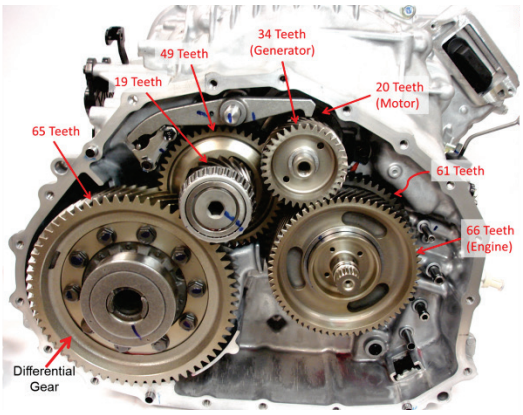

Figure 15: 2014 Accord transmission gear section.

The Accord motor and generator stator and rotor laminations appear to be identical—the stator outer diameters are 29.13 cm (11.469 in.), the rotor outer diameters are 19.502 cm (~7.678 in.), and the air gap is about 0.79 mm (0.031 in.). The motor stator stack length is 6.17 cm, which is about 1.64 times the generator stator stack length of 3.762 cm. These metrics and other motor and generator parameters are summarized in Table 1. The motor stator and rotor masses are 20.8 and 11.8 kg, respectively, versus the generator stator and rotor masses of 14.4 and 8.3 kg, respectively. Both stators, shown in Figure 16, have 48 slots with 8 poles with windings comprising wires that are 18 AWG in size. The motor has 20 wires in parallel for each phase, which split into two parallel paths, each of which has four poles in series before combining at the neutral point. The generator motor has 22 wires in parallel for each phase.

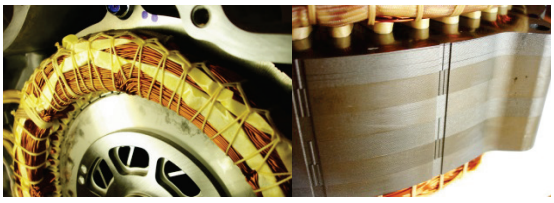

Figure 16: 2014 Accord motor stator.

The rotor lamination design for the Accord motor and generator rotor is shown at left in Figure 17. The design is similar in principle to the rotor lamination design used in the Toyota Prius(right in Figure 17). The inset magnets are in a "V" orientation, and slight dimples are located at the air gap near the tips of the magnets to prevent magnet flux leakage. Both 2014 Accord and 2010 Prius rotor laminations have large

Table. 1: Motor and generator design parameters for various HEVs and EVs

Parameter	Accord G	Accord M	LEAF	2010 Prius	LS 600h	Camry	2004 Prius	Comments
Lamination Dimensions								
Stator OD, cm	29.202	29.134	20.0	26.4	20.0	26.4	26.9	
Stator ID, cm	19.660	19.660	13.10	16.19	13.086	16.19	16.19	
Stator stack length, cm	3.762	6.17	15.1	5.08	13.54	6.07	8.4	
Rotor OD, cm	19.504	19.500	13.0	16.04	12.91	16.05	16.05	
Rotor lamination ID, cm	11.80			5.1	5.3	10.5	11.1	
Rotor stack length, cm				5.0165	13.59	6.2	8.36	
Air gap, mm	0.78	0.8		0.73	0.89	0.73025	0.73025	
Lamination thickness, mm	0.34			0.305	0.28	0.31	0.33	
Mass of Assemblies								
Rotor mass, kg	8.260	11.810	16.432	6.7	11.93	9.03	10.2	Includes rotor shaft.
Stator mass, kg	14.4	20.815		15.99	18.75	18.0	25.9	
Stator core mass, kg	Est			10.36	15.15	12.38	19.05	Laminations only.
Stator Wiring								
Number of stator slots	48	48	48	48	48	48	48	
Stator turns per coil		11?	8	11	7	14	9	
Parallel circuits per phase	2 legs		4 legs	0	2 legs	2 legs	0	
Coils in series per phase	4 per leg		2 per leg	8	4 per leg	4 per leg	8	
Number of wires in parallel	11 per leg	10	15 per leg	12	9 per leg	9 per leg	13	
Wire size, AWG	~18	~18	~20	20	~0.032" ≡ 20	20	19	
Phase resistance at 21°C, ohms			~0.00567	0.077	0.0225	0.023	0.069	Average of phase-to-phase divided by two.
Total mass of stator copper, kg	Est		5.616	4.93	3.59	5.6	6.8	
Slot depth, mm	~28.59	~28.19		30.9	19.25	30.9	33.5	Gap to slot bottom.
Slot opening, mm	~2.037	~2.037		1.88	1.88	1.88	1.93	At air-gap
Magnets (neodymium iron boron [NdFeB])								
Magnet dimensions, mm	26.5x6.28x ~37.62	26.5x6.28x ~61.7	21.3x8.34x2.29 and 28.9x8.36x3.79	49.3×17.88×7.16	66.4×18.7×3.05	60.6×19.1×6.6	83.1×18.9×6.5	
Magnet volume, cm^3	6.26	10.27		6.31	3.78	7.63	10.2	
Magnet mass, grams	~47.2	77.50		48	28.1	58	77	
Total mass of magnets, kg	0.755	1.24	1.895	0.768	1.349	0.928	1.232	Entire magnet mass in rotor.
Magnet mass per published power rating (grams/kW)		10.0	23.69	12.8	8.43	8.84	22.4	

holes in the center of the rotor where magnetic flux is not necessary and therefore rotor mass can be reduced substantially. The Accord has a considerably greater amount of material removed from the center section of the rotor, in a pattern that resembles a camera shutter. Another key distinction between the Accord and Prius rotors is the large gap between the magnetic poles of the Accord, along with an oval and a small hole at the tip of each oval. These features help reduce magnet flux leakage and change the magnetic saliency of the rotor, which can modify reluctance torque contributions and potentially yield a more smooth torque profile. The overall NdFeB magnet mass is 0.76 kg for the generator rotor and 1.24 for the motor rotor. A comparison is made in Table 1, where a ratio is computed with the magnet mass and the published power rating. This ratio is about 10 for the Accord motor, which is slightly higher than that of the Camry and first-generation Prius, but lower that that of the 2010 Prius.

Figure 17: 2014 Accord generator rotor lamination (left) and 2010 Toyota Prius lamination (right).

The 2014 Accord PCU, shown in Figure 18, includes an inverter for the generator, an inverter for the motor, and a boost converter to boost the battery voltage up to a level of 700 V, depending on driving conditions. The PCU, manufactured by Fuji Electric, has an overall mass of 17.5 kg and a volume of 12.37 L. Various views of the PCU are shown in Figure 19, where the dc input connector from the battery and 3-phase output connectors from the motor and generator inverters are visible. An electrical schematic that represents

the operation of the PCU is shown in Figure 20. The overall functionality of the PCU is nearly identical to that of the Toyota PCU, in that the boost converter operates similarly, and the output of the boost converter supplies a high-voltage dc link for the motor and generator inverters. The PEV version of the Accord has a nominal battery voltage of 320 V and the HEV Accord has a nominal battery voltage of 259 V.

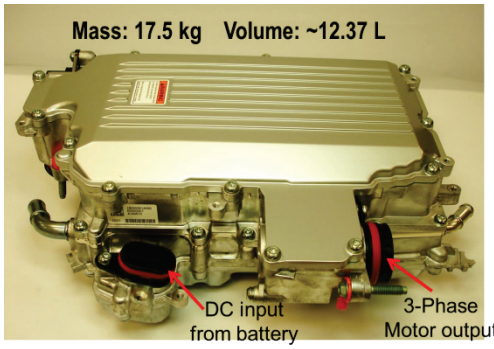

Figure 18: 2014 Accord PCU overview.

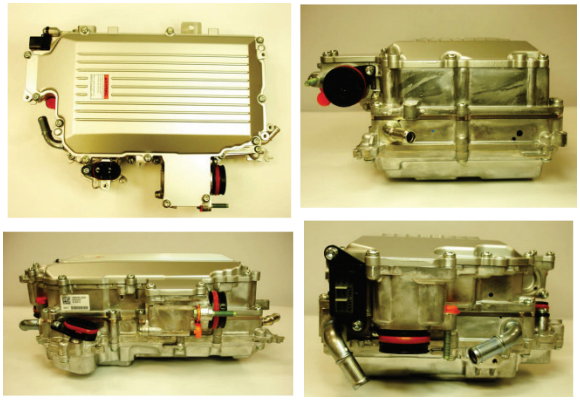

Figure 19: Various views of 2014 Accord PCU.

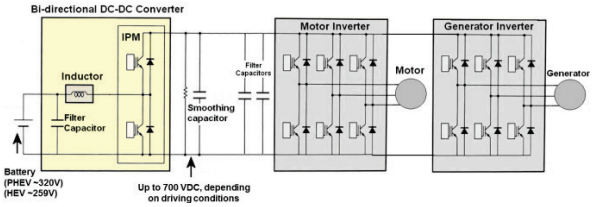

Figure 20: Electrical schematic of 2014 Accord PCU.

The bottom compartment of the Accord PCU, shown upside down in Figure 21, contains large bulk capacitors and the inductor for the boost converter. The boost inductor is mounted to the bottom of a heat exchanger, and white thermal paste is used to facilitate heat transfer from the inductor. The input from the battery is attached to a filter capacitor and fed through the boost inductor. The capacitor on the dc input from the battery is rated at 410 uF and 370 Vdc. The output of the boost converter passes through a current transducer for feedback control and connects to the input of the power electronics of the boost converter. The power module and control board are located in the top compartment, shown in Figure 22.

The output of the boost converter power electronics is directly connected to a dc link bus that connects to the motor

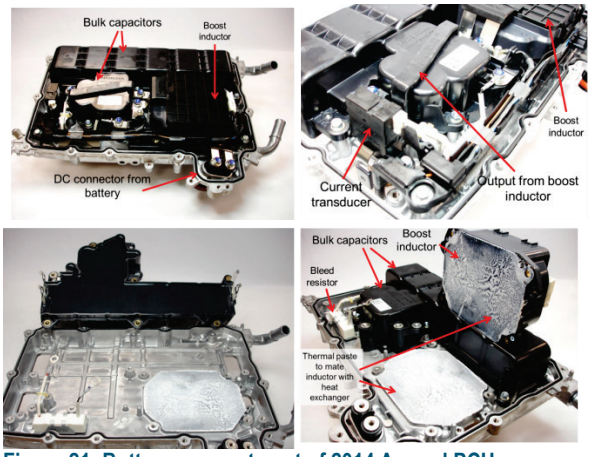

Figure 21: Bottom compartment of 2014 Accord PCU.

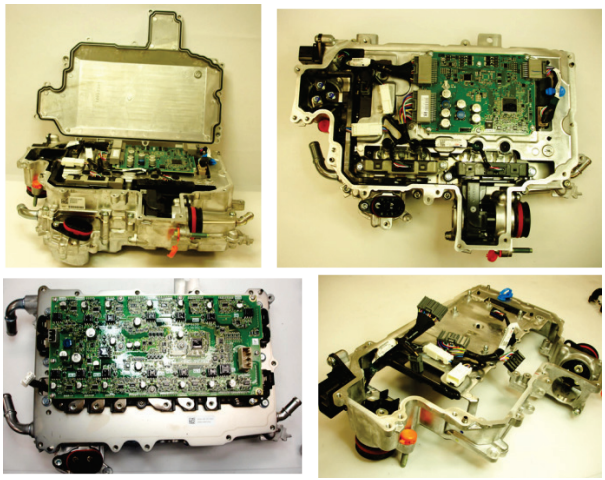

Figure 22: Top compartment of 2014 Accord PCU.

inverter and generator inverter power electronics. Both positive and negative high-voltage buses extend the width of the power module, shown in Figure 22 and Figure 23. This dc link extends from both ends of the power module in the top compartment to the capacitor in the bottom compartment. Several capacitor cells are vertically oriented to form a bulk capacitor rated at 1125 uF and 700 Vdc. There are also two small 700 Vdc, 0.047 uF capacitors attached to the high-voltage dc link. The high-voltage capacitors and the capacitor attached to the battery input are located within one potted module. There is no direct contact between the capacitor module and the heat exchanger.

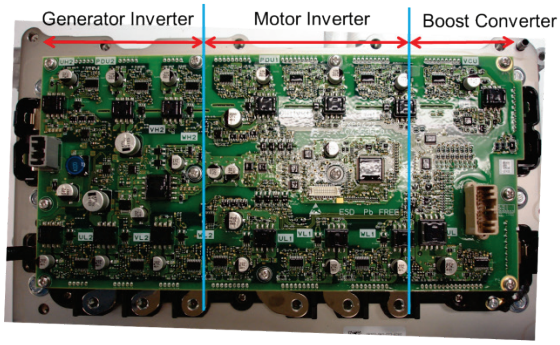

Figure 23: Power module and driver board in 2014 Accord PCU.

The control board includes two 32 bit, 32 MHz Renesas microcontrollers (D70F3507M1GJA2) for the control of the electric motor and generator. The board includes a Tamagawa AU6802 resolver to the digital chip to supply and convert analog signals for position feedback. The control board is mounted to a plate that is cast with the housing of the top compartment, as shown at lower right in Figure 22. Other benchmarked PCUs use a thinner sheet of metal that mounts to a cast housing. In addition to being used for support, the metal piece also mitigates the impact of electromagnetic interference from the power module on the control circuitry.

A similar 32 bit, 32 MHz Renesas microcontroller is located on the driver board shown in Figure 23. The driver board is mounted directly to the power module, and the locations of the power electronics devices for the motor inverter, generator inverter, and boost converter are indicated in Figure 23. The generator inverter includes one insulated gate bipolar transistor (IGBT) per switch, yielding a total of six IGBTs and diodes for the generator inverter. The motor inverter uses two IGBTs per switch, so the entire motor contains 12 IGBTs and diodes. Three IGBTs are used on the lower switch of the boost chopper, and only two IGBTs are used in the upper switch of the chopper, which is used during regenerative braking. All previously benchmarked PCUs include that same number of IGBTs for both upper and lower switches of the boost chopper. Current transient requirements for the lower switch and upper diode are more substantial than those of the upper switch; therefore, Honda was able to implement a slightly lower-cost solution for the boost converter power electronics.

The power module is directly integrated with the heat exchanger, as shown in Figure 24. Conventional power modules have heat spreaders. A layer of thermal paste is applied to the bottom of the power module and, in the case of many benchmarked PCUs, attached to a heat exchanger that is cast as a part of the housing. However, the Accord PCU has no thermal paste because the heat exchanger is directly integrated with the module, thereby greatly improving the heat transfer from the power electronics devices to the cooling medium. Fine fins, shown on the right in Figure 25, are machined on the bottom of the heat sink, which is cooled by a mixture of water and ethylene glycol. The other side of the heat exchanger is part of the bottom compartment, and the flow path of the coolant is indicated on the left in Figure 25. Slight indentions are located in the flow path adjacent to the boost inductor, and several fins are located in the flow path below a smaller portion of the boost inductor, by which the coolant passes just before exiting the PCU.

Detailed designs were developed to provide access to the electric motor shaft in the transmission while maintaining the cooling and lubrication functionality used in the original form. This integration requires special attention to detail because high speed and power levels are involved. The electric motor shaft is not normally externally accessible, and unique methods were required to obtain access for dynamometer testing. A custom plate was designed with high-tolerance alignment features and considerations for lubrication. A unique adapter shaft was also designed to adapt the motor shaft to ORNL's dynamometer. The graph in Figure 26 shows a comparison of back–electromotive force results, which are considerably lower for the Accord. The 2014 Accord hybrid system is currently being tested to verify performance and to obtain detailed characteristics across the entire operation range of the system.

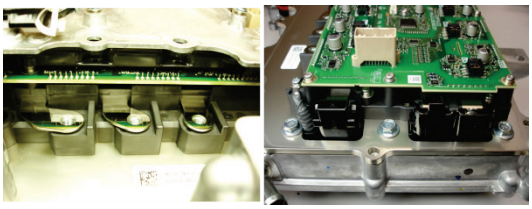

Figure 24: Power module and driver board in 2014 Accord PCU.

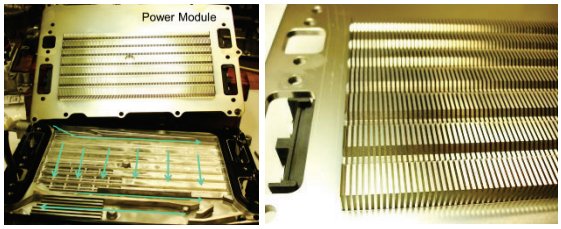

Figure 25: 2014 Accord PCU heat exchanger.

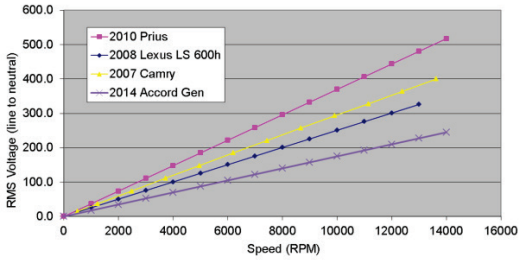

Figure 26: 2014 Accord back–electromotive force test results.

Conclusions and Future Directions

Detailed testing of the Nissan LEAF charger indicates that the efficiency of the charger varies greatly depending on the input voltage. For an input voltage of 120 V, the total charger efficiency at 3.3 kW is about 87%, versus an efficiency of about 91.3% for operation at 240 V. Operation at 6.6 kW and 120 V is not possible because of the current limitations of common household receptacles. A charger efficiency of 91.5% was observed for operation at 6.6 kW and 240 V.

The 2014 Honda Accord transmission/transaxle includes a 124 kW electric motor and a generator that absorbs energy from the combustion engine to recharge the battery and to supply energy to the electric motor for vehicle propulsion. For most conditions, the system operates as a series hybrid in that the combustion engine propels the vehicle only through the generator and motor. In some low to medium road load conditions and at high speeds, a clutch locks the engine into the drivetrain with a fixed gear ratio. A comparison of the ratio of magnet mass to published power rating indicates that the Accord motor has a slightly higher ratio than the Camry and first-generation Prius but a slightly lower ratio than the 2010 Prius.

The Accord PCU is very similar in principle to the PCU in the Toyota hybrid systems in that it has a boost converter that supplies the generator and motor inverters. The boosted voltage reaches up to 700 V, which is slightly higher than the boosted voltage of 650 V for the Toyota systems. The power module was directly integrated with the heat exchanger, thereby eliminating the use of thermal paste and greatly increasing heat transfer from the power electronics devices to the coolant medium.

ORNL has integrated custom motor controls with the PCU while maintaining the OEM driver circuitry. Detailed designs were developed to provide access to the electric motor shaft in the transmission while maintaining the cooling and lubrication functionality used in the original form. The 2014 Accord hybrid system is currently being tested to verify performance and to obtain detailed characteristics across the entire operating range of the system.

FY 2014 Publications/Presentations

[1] Tim Burress, "Trends and status of on-the-road HEV/EV technologies," IEEE Energy Conversion Congress and Exposition, September 2014.

[2] T. Burress, "Benchmarking EV and HEV technologies," 2014 Annual Merit Review and Peer Evaluation Meeting for the DOE Vehicle Technologies Office, Washington, D.C., June 2014.

[3] T. Burress, "Benchmarking EV and HEV technologies," Vehicle Technologies Office Advanced Power Electronics and Electric Motors R&D FY 2014 Kickoff Meeting, Oak Ridge, Tennessee, November 2013.

3.1 Power Electronics Packaging

Zhenxian Liang (Principal Investigator)

Oak Ridge National Laboratory
National Transportation Research Center
2360 Cherahala Boulevard
Knoxville, TN 37932
Phone: (865) 946-1467; Fax: (865) 946-1262
E-mail: liangz@ornl.gov

Burak Ozpineci, ORNL APEEM Program Manager
Phone: (865) 946-1329; Fax: (865) 946-1262
E-mail: burak@ornl.gov

Susan A. Rogers, DOE APEEM Program Manager
Phone: (202) 586-8997; Fax: (202) 586-1600
E-mail: Susan.Rogers@ee.doe.gov

Start Date: October 2012
Projected End Date: September 2014

Objectives

- Develop advanced packaging technologies that exploit the attributes of wide bandgap (WBG) power semiconductors, resulting in comprehensive improvements in the cost-effectiveness, efficiency, and power density of electric drive systems.
  - FY 2014: Develop process technologies and fabricate specific silicon carbide (SiC) power modules for inverter/converter integration with significant advances in performance.

Technical Barriers

- State-of-the-art automotive power modules and power inverters and converter packaging technologies have limitations in electrical performance, cooling capability, thermomechanical properties, and manufacturability. These are barriers to meeting the DOE APEEM 2020 targets for cost, efficiency, and density.

Technical Targets

- Develop packaging technologies for advanced WBG power modules with lower thermal resistance, small electric parasitic parameters, and temperature-tolerant capability that can be manufactured efficiently.
- Identify the performance attributes and limits of state-of-the-art WBG power devices in power conversion systems.
- Advance WBG automotive power electronics in electrical performance, cooling efficiency, and thermomechanical capability through highly functional packaging integration.

Accomplishments

- Delivered first-generation SiC integrated power modules (IPMs) for system evaluation, leading to 30% overall volume and weight reductions.
- Developed an integrated cooling SiC 100 A/1200 V phase-leg module that enables 3× current density increases over its conventional silicon (Si) counterpart, resulting from a 35% reduction in the die size; 40 and 80% reductions in conduction and switching power losses, respectively; and a 35% reduction in package thermal resistance.
- Developed an innovative planar-bond-all (PBA) SiC package that
  - integrates double-sided direct cooling that is 40% more efficient
  - realizes 3-dimensional (3D) planar interconnection with a 75% reduction in parasitic electrical inductance and a 90% reduction in resistance
  - incorporates advanced low-cost manufacturing
  - allows converter/inverter system-level functional integration

✧ ✧ ✧ ✧ ✧

Introduction

WBG power semiconductors, such as SiC and gallium nitride, are known to provide superior power switching features—high current density, low-loss high switching speed, and high operation temperature—compared with their silicon (Si) counterparts. State-of-the-art WBG discrete devices and multi-chip modules are manufactured using technologies that follow packaging schemes used for Si devices. The packaging processes include die attachment and top interconnection, power substrate, power and signal terminals, baseplate, and encapsulation. Specifically, interconnection and die attachment are accomplished by multiple bond wires (from the top of the die) and reflowed solder areas (from bottom of die) onto the power substrate, respectively. In power converter/inverter assembly, the modules need to be attached to a heat sink or cold plate using forced air or liquids for cooling of the semiconductors. In general, a thermal interface material such as thermal grease is usually applied between the modules and the heat sink for good thermal transfer. Although they fulfill well their designed electrical, thermal, and mechanical functions, these hybrid package technologies have limitations in electrical performance, cooling capability, thermomechanical properties, and manufacturability. In particular, they limit the full exploitation of the attributes of WBG semiconductors and, in turn, limit the benefits of WBG power electronics with regard to cost, efficiency, and power density in automotive electric drive systems. These limitations can be characterized by a set of technical metrics such as

thermal impedance (resistance and capacitance), electrical impedance (resistance and inductance), thermomechanical properties (power, thermal cycling numbers, and vibration ruggedness), and others. Establishing the relationships between these parameters and the power module performance criteria (e.g., efficiency, reliability, cost, and density) makes it easier to evaluate power module technologies and to identify the shortcomings of existing technologies and develop new concepts. In past years, many techniques in SiC power module packaging, focused on improving these technical parameters, have been developed to promote successfully the adoption of WBG power semiconductors in power electronics.

This project emphasizes the integration of advanced packaging concepts into all-SiC power modules, enabling the exploitation of SiC superior performance. Technical details such as packaging structure and associated packaging process technology were developed. Performance improvements were characterized by experimental measurements; and efficiency, cost, and reliability benefits to power electronics systems were evaluated.

Approach

The target all-SiC power module is a one-phase-leg configuration, composed of SiC metal-oxide-semiconductor field-effect transistors (MOSFETs) and SiC Schottky barrier diodes (SBDs) (see Figure 1), which is a basic building block for various automotive power converters and inverters. Power SiC MOSFETs and diodes are commercially available in the form of bare dies, both with ratings of 50 A and 1200 V. The current rating of the power module can be multiplied by paralleling more dies. Figure 1 shows the topology for a 100 A, 1200 V phase leg all-SiC power module. The switch units consist of two paralleled bare dies for each switch.

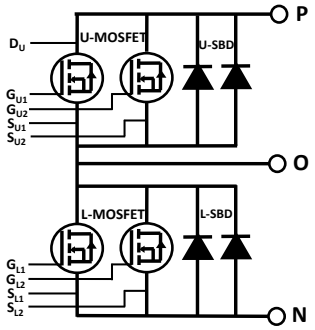

Figure 1: Electrical diagram of an all-SiC phase-leg power module (U=upper unit, L=lower unit) with multiple paralleled devices.

Two types of packaging for this module have been successfully prototyped in-house, as shown in Figure 2. Figure 2(a) presents a photo of this module fabricated using conventional packaging technology (first-gen module). Its structural details are schematically depicted in the cross-sectional view in Figure 2 (b). It is similar to most industrial SiC power module packages and was built as a baseline to identify the basis packaging parameters. Figure 2 (c) shows a photo of a second-gen SiC module. It is unique in that it features an integrated direct cooling configuration, schematically depicted in Figure 2 (d), in which a single cold-base plate replaces the base plate and cold plate in the first-gen package. The cold-base plate used is specially made of a flat copper tube with crisscrossing fins inside. In this module package, the power stage on the direct bond copper (DBC) ceramic power substrate is directly soldered onto the cold-base plate. Thus it not only eliminates the thermal grease and base plate, compared with the conventional power module thermal package scheme, but also realizes integrated, direct cooling.

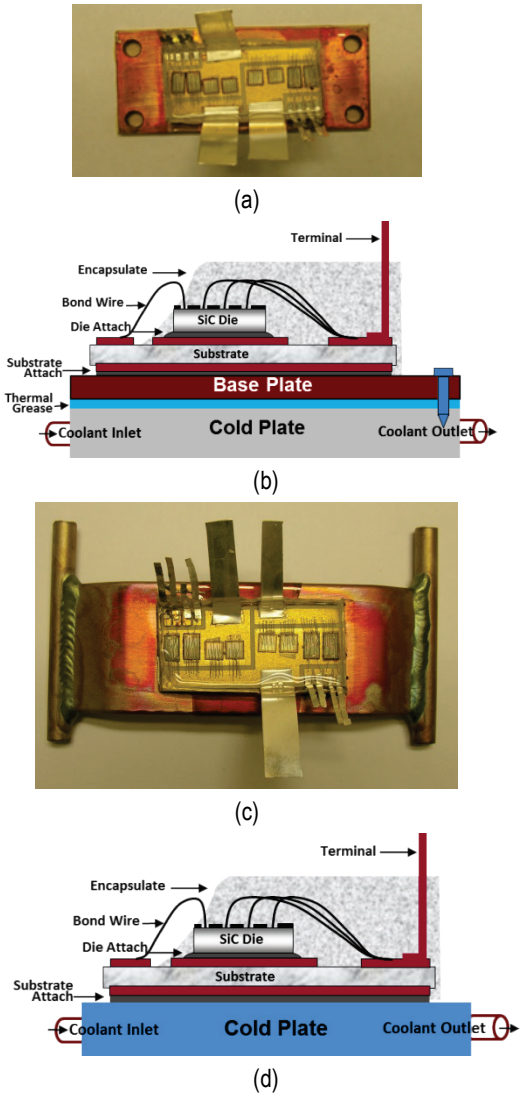

Figure 2: Two types of SiC phase-leg power module prototypes: (a) photo of a first-gen module with (b) conventional packaging configuration (cross-sectional view), (c) photo of second-gen module and (d) package with direct cooling from integrating a cold-base plate.

The result of the cooling integration is that the specific thermal resistance of the integrated cooling package is more than 14% lower than that of a conventional (first-gen) package. To assess the effect of this improvement and the advantages of SiC devices over their Si counterparts, four

samples with different package/device combinations were prototyped. Silicon insulated gate bipolar transistor (IGBT)/PiN diode dies have the same current and voltage ratings as SiC devices. The improvement resulting from highly efficient integrated cooling can be observed in the increase of allowed current density in the SiC die. With a fixed current density, for example 100 A/cm^2, the difference in the junction temperature ranges from ~36 to 170°C between the SiC/integrated cooling and Si/conventional cooling combinations. The higher temperatures, on the one hand, lead to a significant reduction of the power module lifetime. On other hand, if the maximum operational boundary is set based on temperature limits, the maximum handling current density of a power device for the four combinations increases from 66 to 185 A/cm^2 for a 100°C temperature increase, which can be a case for a coolant temperature of 65°C and a junction temperature of 165°C. These maximum current density values define the minimum die area of the power semiconductors for a designed system current (or power) rating. It is well known that die size is a dominant factor in power module cost. The 3× die area reduction for SiC/integrated cooling combination compared with Si/conventional cooling is significant for reducing the system cost.

In FY 2014, further development of SiC power electronics packaging was focused on two major aspects: (1) the packaging integration of gate drive circuitry and power module to produce IPMs and (2) PBA SiC power module packaging.

A. Integrated SiC Power Module

A prototype SiC IPM was designed to integrate the first – gen SiC power module and a two-channel gate driver board in one package, leading to a smart (or intelligent) SiC power module. Figure 3 shows the conceptual schematics of this IPM. The gate drive circuitry on board is assembled closely on top of the power module with transparent silicone gel encapsulation of power devices and interconnection. Such integration not only reduces the part number and increases the power density of the converters but also improves the package performance. The matched interconnection was designed to enable the shortest distance between the output of the gate driver and the input of the power devices. The effects of the tight interconnection can be observed in the lumped electrical element model of a packaging electrical interconnection, as shown in Figure 4. It was obtained by employing an electromagnetic simulation tool (MAXWELL Q3D Extractor) that calculates the electromagnetic field and extracts the parasitic components through current conduction paths. The components enclosed within the dashed line are related to the signal pins in a conventional discrete power module assembly. These parasitic components will degrade the signal fidelity from the gate drive to the device, causing undesired voltage and current ringing and limiting the switching speed of SiC devices to far from their maximum regime. In the IPM, these parasitic components were much reduced, making it possible to operate the SiC devices at higher frequency and higher efficiency.

The Si gate drive circuit in this IPM was designed in-house and fabricated specifically. It is based on silicon-on-insulator (SOI) technology, featuring a high operating temperature. A two-channel high-temperature gate drive board was built based on the chip-on-board technique, which also offers the shortest interconnection paths. The experimental results demonstrated the high-temperature operating capability of the gate drive circuitry at up to 200°C.

Furthermore, to promote SiC devices operating at higher temperatures (>200°C), a set of high-temperature packaging materials and associated technologies were used in fabricating this IPM.

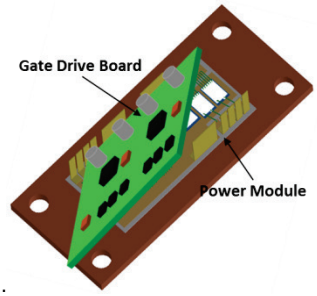

Figure 3: Schematics of an integrated SiC power module: the gate drive circuitry on the printed circuit board is closely connected to the power module.

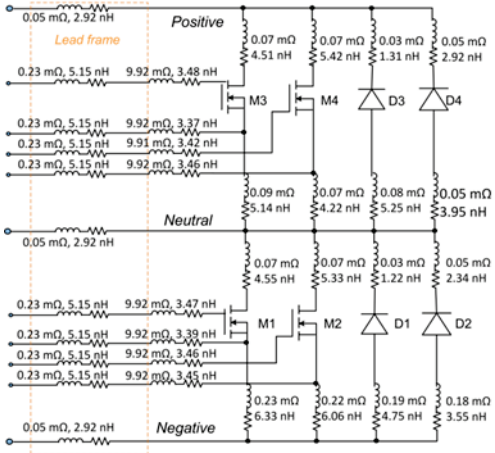

Figure 4: Lumped electric element model of packaging interconnections. The area enclosed by the dashed lines is related to the signal terminals.

B Planar-Bond-All SiC Power Module

A PBA is a power module packaging scheme that differs significantly from conventional packaging schemes (first- and second-gen). The key element is that the top interconnections use a planar, larger-area bond to the electrodes on the die instead of multiple tiny wire bonds. This change offers the possibility of integrating many superior packaging concepts into one module package.

B.1 Three-Dimensional Planar Power Interconnection

Figure 5 is a schematic of the planar interconnection configuration for the phase-leg power module. The four MOSFET and four diode dies are sandwiched between two DBC substrates. The electrical interconnection is achieved by conductively bonding these dies from both the top and bottom sides to the copper traces on the two substrates, which are patterned to form circuitry corresponding with the electrode

pad layout on the dies. The DBC substrates provide electrical insulation via the internal ceramics (such as aluminum nitride) between two copper layers. This symmetric planar-bonded package offers flexibility in the arrangement of the switch dies. As shown in Figure 5, the upper switch pair and lower switch pair in the phase-leg topology are oriented in a face-up/face-down configuration. This makes optimal use of the die's vertical electrode arrangement. Unlike in a traditional wire bond layout, in which all dies are placed in a face-up orientation, the main current flowing loops are also on the X-Y plane of the substrate. However, in the face-up/face-down orientation, the main current flowing loops fall in the X-Z plane of the package. The interconnection between dies is in a 3D planar pattern. The thickness (in Z direction) of the switch die is typically 0.1mm, and its length (X direction) or width (Y direction) is in the range of 10 mm. Thus the length and the enclosed area of the main current loops in the 3D interconnection configuration are reduced dramatically, leading to a significant reduction in electrically parasitic inductance and resistance.

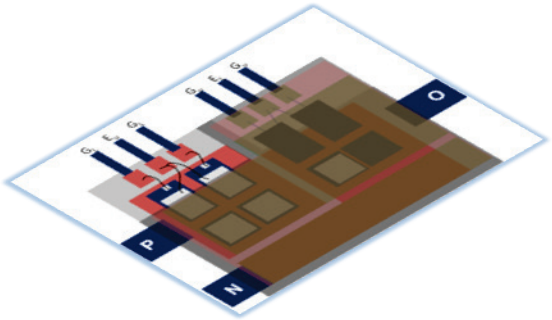

Figure 5: Three-dimensional planar power interconnection configuration in PBA SiC phase-leg power module.

The lumped circuit model of such an electrical interconnection is shown in Figure 5. The sums of the lumped elements along a main current path from the positive terminal through the upper MOSFET, and then from the lower diode to the negative terminal, are the representative parameters of the package structure. In this planar-bonded power module, the total inductance *L* is 13.58 nH and the total resistance *R* equals 0.25 mΩ. By comparison, the parasitic electrical parameters in a conventional wire-bonded power module are L=53.3 nH and R=2.45 mΩ, respectively.

B.2 Integrated Manufacture Process

In the module structure described, the numerous tiny wire bonds used in conventional packaging are replaced by a few identical planar area bonds. This arrangement makes batch processing possible. For batch processing, a special process method has been developed in which, as shown in Figure 6(a), all components are first assembled into a premade jig. The components include the patterned DBC substrates, multiple bare dies and shims, preformed bonding material (such as solder preform), power terminals and signal pins, and so on. The second processing step involves heating the assemblies simultaneously to form the bonds and creating the final package. The simplicity of the process helps reduce costs and improve the manufacturability of the modules. This technology is called PBA, representing the features inherent in the packaging structure as well as the fabrication process.

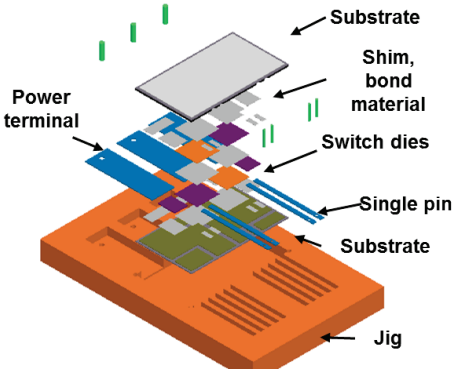

(a)

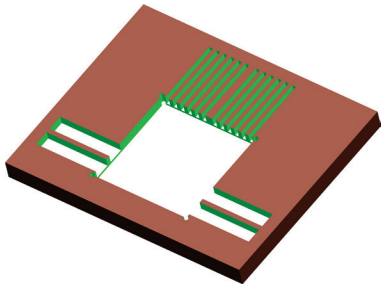

(b)

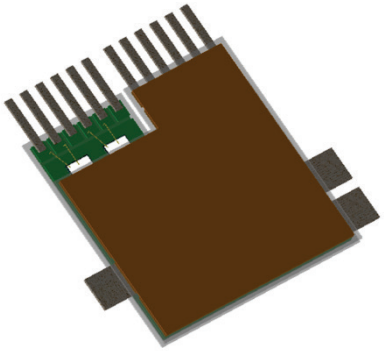

(c)

Figure 6: Manufacturing process of planar-bond-all packaging: (a) schematic of component assembling, (b) a specific jig for alignment of multiple components, (c) schematic of packaged SiC power module.

Figure 6(b) is the schematic of a specific jig designed for assembling PBA SiC power module packaging components. Figure 6(c) is a schematic of the PBA SiC power module design. The module body measures 40 ×40 × 2 mm, excluding the terminals and pins. A soldering process is employed to form the planar bonding because of its high electrical conductivity and ease of processing. The special top metallization of the power semiconductor dies required for reliable solder bonding was done during the wafer-level processing. The power terminals (positive, neutral, and negative) and signal pins are also mounted between the two substrates by soldering to form compact input/output connections.

B.3 Double-Sided Integrated Direct Cooling

The planar bond structure allows dual side thermal dissipation paths from both the top and bottom surfaces of the power package.

The internal assembly in Figure 7 is an example of an integrated double-sided cooling design, in which two pin-fin base plates made of copper are directly bonded to the power package (Figure 6c) from both sides by another soldering process.

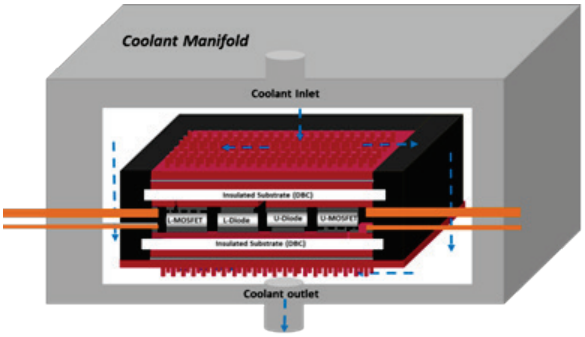

Figure 7: Double-sided integrated direct cooling of PBA module (internal) located in a coolant manifold.

The heat generated in the dies can be more efficiently removed by applying double-sided cooling through forced-air or liquid heat transfer. Additionally, direct attachment (bonding) of the heat sink or cold plate leads to further reduction in the thermal resistance, as discussed earlier.

This module can be directly cooled by air. For higher efficiency, forced liquid cooling is employed in most applications. Figure 7 shows schematically that the power module is assembled into a special coolant manifold. The manifold provides liquid passageways and allows coolant to pass through the pin fins efficiently.

Results

The benefits gained through the innovative packaging can be demonstrated by the system performance improvements of the prototype modules fabricated in our Advanced Power Electronics Packaging Lab.

A. Integrated SiC Power Module (IPM)

The prototype IPM based on the design in Figure 3 is shown in Figure 8 as a zoomed-in insert consisting of three parts: a 100 A/1200 V SiC phase-leg module on the bottom, a gate drive board in the middle, and a power supply board on the top. They are assembled to form one building block in a converter. Figure 8 presents a photo of a buck converter based on this SiC IPM. The other converter components include a 0.75 mH inductor and a 20 μF capacitor. The equivalent resistive load is around 18 Ω. Figure 9 illustrates the waveforms of the converter operating at a switching frequency of 100 kHz, a 600 V dc bus voltage, and a 0.25 duty-cycle.

To evaluate the high-temperature capability of this module, the IPM was mounted on a heat sink that was cooled by natural convection in ambient air at room temperature and heated through device self-heating. The switching frequency was gradually pushed from 10 to 100 kHz to raise the power MOSFET junction temperature above 225°C. Continuous power testing at each switching frequency point was carried out for 30 minutes to reach a steady state. The junction temperature at each step was measured by a method in which the turnoff delay time was used as a temperature sense parameter. Before continuous operation of the SiC MOSFET, a calibration curve of delay time versus junction temperature was obtained under identical operating conditions. For instance, in the SiC MOSFET under test, the delay time = 0.38 Tj + 231.7, where *Tj* was the junction temperature. As shown in the lower section of Figure 9, the zoomed-in turnoff transient, the measured turnoff delay time was 320 ns. It corresponds to a junction temperature of 232°C, according to the calibration relationship discussed above.

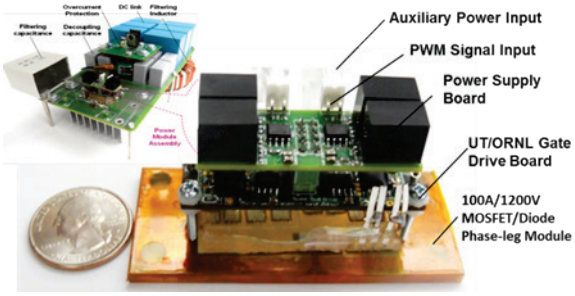

Figure 8: A buck converter based on the ORNL SiC integrated power module.

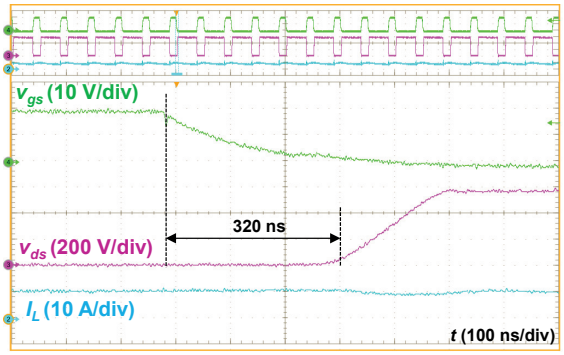

Figure 9: Voltage and current waveforms of SiC IPM converter operating at a frequency of 100 kHz, 600 V dc bus voltage, and 0.25 duty cycle.

Even though the SOI Si gate drive chip was operated successfully at 200°C separately, the performance of the IPM at a high ambient temperature (e.g., 150°C) has not yet been evaluated because some of its auxiliary components, such as isolation circuitry and power sources, were not rated for a high-temperature class. In the future, other strategies, such as integrating SOI Si chips and SiC devices, are proposed for further exploitation of the high-temperature features of SiC devices.

B. Planar-Bond-All SiC Power Module

The PBA SiC power module design is illustrated in Figure 6(c). The packaging components or/and parts schematically shown in Figure 6(a), including two DBC substrates, die shims, bonding foils and power terminals, and signal pins, must be specifically fabricated. The SiC dies are

required to have a specific type of metallization on the front surface, different from that for wire-bond interconnections. A specially designed jig, shown in Figure 6(b), was fabricated to assist the soldering process. Based on these efforts and intensive process development and optimization, a group of PBA SiC modules were prototyped. Figure 10 shows a photo of an exemplary one. The module measures 40 × 40 × 2 mm, excluding the terminals and pins.

Various experimental measurements and multi-physics simulation tools were used intensively to characterize the electrical and thermal performance of the module packaging. They are summarized in the following sections.

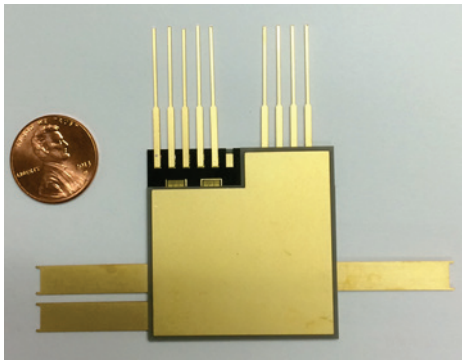

Figure 10: Photo of a PBA SiC power module (third-gen package) with dimensions of 40 × 40 × 2 mm, excluding the terminals and pins.

B.1 Electrical Characterization

The electrical performance of power modules can be drastically influenced by their "parasitic" electric parameters (resistance, inductance, and capacitance), adding to SiC's intrinsic electric parameter network. Parasitic inductances in the current loop will cause a voltage overshoot to be superimposed on the blocking voltages of the devices as they are turned on and off. From the current and voltage waveforms, it was observed that there is only 30 V of overshoot adding to a 600 V bus voltage. This is attributed to the smaller parasitic inductance (13.58 nH for the third-gen package) compared with a 53.3nH inductance in the conventional modules (first- and second-gen). On the other hand, the voltage overshoot is dependent on the switching speed (current decrease slope). The smaller inductance allows the MOSFETs in the PBA module to operate at a higher frequency, an important feature of SiC devices and an effective way to increase the power density of SiC inverters.

The parasitic inductance and resistance also increase the power losses of SiC switches. It has been demonstrated that the PBA module reduces these parasitic-related losses by 75% compared with conventional devices.

B.2 Thermal Characterization

The thermal performance of a power module can be modeled as thermal resistance and capacitance networks. The thermal capacitance determines the transient response of the power module to power dissipation in the switches, and the thermal resistance determines the cooling efficiency.

To implement double-sided cooling on the module shown in Figure 10, different configurations were designed based on applying different cooling devices. In one prototype (Figure11), two pin-fin cold plates were added from both sides. As illustrated in Figure 7, two cold plates were directly bonded to the back sides of the DBC substrates by reflowed solder. Once the cooling medium, forced air or liquid, goes through the pin fins, the heat generated in the package is efficiently removed because of the low thermal barriers between device and coolant. It can be seen that this design fully fulfills an integrated double-sided-direct cooling scheme, which will exploit efficiently the SiC feature of high current/power density. The effective pin fin array area in the pin-fin cold plate is 38×38 mm. The fin height is 7 mm. The outline of this assembly measures 50 × 50 ×18 mm, excluding terminals and pins.

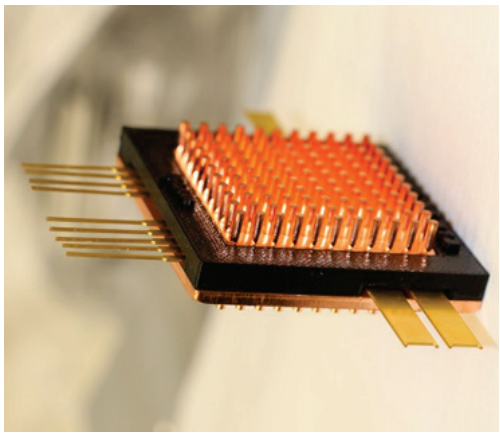

Figure 11: Photo of PBA SiC module packaged with integrated double-sided pin fin cold plates.

As illustrated schematically in Figure 7, double-sided forced-liquid cooling of this module can be achieved by assembling the module into a specially made coolant manifold. Figure 12 presents a final assembly of the PBA module and manifold. The open tube in front is a coolant inlet. The outlet tube is on the back side. The channels inside guide the coolant flow uniformly.

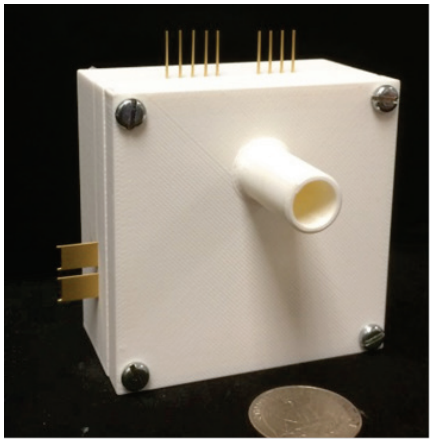

Figure 12: Photo of SiC integrated pin-fin PBA power module in a coolant manifold for double sided cooling.

The thermal parameters can be obtained by experimental thermal tests emulating the operation of the power modules. A method of determining junction temperatures was employed that uses the voltage drop of the body diode in the SiC MOSFET as a temperature sense parameter. By analyzing the cooldown temperature curves and input electric power value,

the thermal parameters (resistance and capacitance) of the module can be extracted. For a fair evaluation of the thermal performance of a packaging assembly, a specific thermal resistance, $\theta_{ja,sp}$, was taken as a figure of merit, which is a normalized parameter by die area i.e., $\theta_{ja,sp}$ = die area × thermal resistance). Here, the thermal resistance is the sum of those from all thermal stacking elements, including the coolant, the pin-fin substrate, the DBC substrates, and the switch dies.

Figure 13 shows the measured specific thermal resistance value of the PBA module with double-sided cooling. For comparison, the specific thermal resistances of the wire-bond package (first-gen) and single-sided cooling package (second-gen) are also presented. The first-gen module, as shown in Figure 2 (a), was mounted on a cold plate with thermal grease and has a specific thermal resistance of 0.54 $cm^2 \cdot °C/W$; the integrated single-side cooled module (second-gen), as shown in Figure 2(c), has a thermal resistance of 0.47 $cm^2 \cdot °C/W$. The double-sided cooling of the PBA module assembly reduces the specific thermal resistance to 0.33 $cm^2 \cdot °C/W$, which is 39% lower than that of the first-gen module assembly.

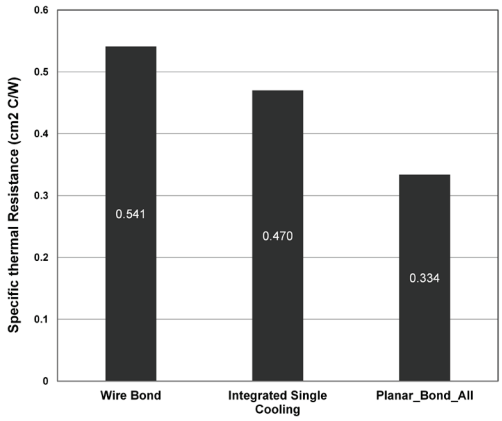

Figure 13: Specific thermal resistance and comparison with conventional and single-sided cooling modules.

B.3 Effects on Power Electronics System

The reduction in both parasitic power losses and thermal resistance helps increase the operational current (power) density in the SiC die. This can be seen in the graph of junction temperature versus current density (Figure 14). For a 100°C temperature increase, the characteristic current densities of the MOSFET in the module are 145 A/cm^2, 184 A/cm^2, and 220 A/cm^2, respectively, for a (first-gen) conventional cooling configuration, single-sided integrated cooling (second-gen), and double-sided direct cooling (third-gen). The third-gen package increases the current density of the SiC power device by 53%.

Die size is known to be a dominant factor in power module cost. The current density increase from the conventional first-gen package to the third-gen SiC integrated cooling package is significant for reducing the power electronics system cost.

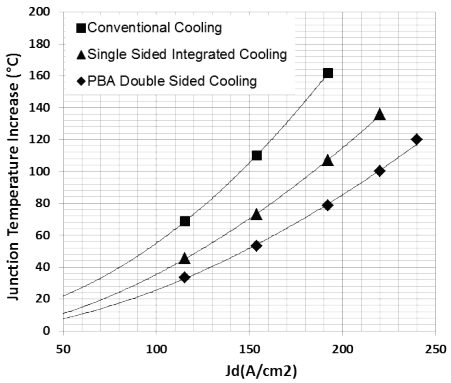

Figure 14: Performance of PBA SiC power module: (a) turn-off switching waveforms; (b) specific thermal resistance and comparison with conventional and single-sided cooling modules; and (c) comparison of junction temperature vs current density for different packages.

Conclusions and Future Directions

The advanced packaging technologies successfully developed in FY 2014 include gate drive circuitry integration, 3D planar interconnection, double-sided cooling, and simplified manufacturing processes. The resultant improvements in electrical parasitics and thermal impedance enable the efficient exploitation of WBG power devices. The benefits gained from these innovations are demonstrated by comprehensive upgrades in SiC packaging performance, leading to high-efficiency, high-density system operation beyond the limits of state-of-the-art technologies. These advances result in higher power conversion efficiency (low losses), and improved cost-effectiveness through reductions in power semiconductor size and higher productivity in manufacturing.

Further advancement of WBG automotive power electronics will depend greatly on improvements in power packaging technology through advances in structure, materials, and processing techniques. The focus will be on developing highly integrated functionality for WBG power inverter/converter modules with intelligence and improved operating performance (efficiency, density, and cost). The effort will include (1) incorporating advanced gate drive circuitry into the third-gen package, (2) implementing highly integrated cooling technologies for integrated multi-phase conversion systems, (3) optimizing interconnection layouts and embedding passives for electromagnetic interference containment and sensors; (4) developing processes for temperature-tolerant integrated SiC power module packages.

These advancements will enable considerable strides toward achieving DOE power density and cost targets for power electronics systems in electric drive vehicles.

FY 2014 Publications/Presentations

Publications

[1] Z. Liang, P. Ning, F. Wang, and L. Marlino, "A phase –leg power module packaging with optimized planar interconnection and integrated double sided cooling," *IEEE Journal of Emerging and Selected Topics in Power Electronics* **2**(3), 487–495, September 2014.

[2] P. Ning, Z. Liang, and F. Wang, "Power module and cooling system thermal performance evaluation for HEV application," *IEEE Journal of Emerging and Selected Topics in Power Electronics* **2**(3), 443–450, September 2014.

[3] Z. Liang, P. Ning, and F. Wang, "Development of advanced all-SiC power modules," *IEEE Transaction on Power Electronics* **29**(5), 2289–2294, May 2014.

[4] Z. Xu, D. Jiang, M. Li, P. Ning, F. Wang, and Z. Liang, "Development of Si IGBT phase-leg modules for operation at 200°C in hybrid electric vehicle applications," *IEEE Transaction on Power Electronics* **28**(12), 5557–5567, December 2013.

[5] A. A. Wereszczak, T. G. Morrissey, C. Volante, P. Farris, Jr., R. Groele, R. H. Wiles, and H. Wang, "Thermally conductive MgO-filled epoxy molding compounds," *IEEE Transactions on Components, Packaging and Manufacturing Technology* **3**(12),1994–2005 (2013).

[6] Z. Wang, X. Shi, L. Tolbert, F. Wang, Z. Liang, D. Costinett, and B. Blalock, "A high temperature silicon carbide MOSFET power module with integrated silicon-on-insulator based gate drive," *Proceedings of the Fifth IEEE Energy Conversion Congress and Exposition*, Pittsburgh, PA, September 14–18, 2014.

[7] B. Guo, F. Wang, P. Ning, E. Aeloiza and Z. Liang, "All-SiC power module for delta-type current source rectifier," *Proceedings of the Fifth IEEE Energy Conversion Congress and Exposition*, Pittsburgh, PA, September 14–18, 2014.

[8] D. DeVoto, P. Paret, and A. A. Wereszczak, "Stress intensity of delamination in a sintered-silver interconnection," Paper WA26, pp. 190–197 in *Proceedings of IMAPS HiTec*, Albuquerque, NM, May 13–15, 2014.

[9] A. A. Wereszczak, Z. Liang, M. K. Ferber, and L. D. Marlino, "Uniqueness and challenges of sintered silver as a bonded interface material," Paper WA23, pp. 178–187 in *Proceedings of IMAPS-HiTec 2014*, Albuquerque, NM, May 13–15, 2014.

[10] A. A. Wereszczak, Z. Liang, M. K. Ferber, and L. D. Marlino, "Uniqueness and challenges of sintered silver as a bonded interface material," in press, *Journal of Microelectronics and Electronic Packaging* 2014.

[11] Z. Zhang, B. Guo, F. Wang, L. M. Tolbert, B. J. Blalock, Z. Liang, and P. Ning, "Impact of ringing on switching losses of wide band-gap devices in a phase-leg configuration," *Proceedings of IEEE APEC'14*, Fort Worth, TX, March 17–21, 2014.

Presentations

[1] Z. Wang, X. Shi, L. Tolbert, F. Wang, Z. Liang, D. Costinett and B. Blalock, "A high temperature silicon carbide MOSFET power module with integrated silicon-on-insulator based gate drive," presented at the Fifth IEEE Energy Conversion Congress and Exposition, Pittsburgh, PA, September 14–18, 2014.

[2] Z. Liang, "Power electronics packaging," DOE Annual Merit Review, Washington, D.C., June 18, 2014.

[3] Z. Liang, "WBG power electronics packaging," Electrical and Electronics Technical Team meeting, April 16, 2014.

[4] Z. Liang, "Integration of cooling function into 3-D power module packaging," Industrial Session Presentation (invited), APEC'14, Fort Worth, TX, March 17–21, 2014.

[5] Z. Liang, "Power electronics packaging," Kick-off meeting, Oak Ridge, TN, November 5, 2013.

FY 2014 Patents/Disclosures

[1] A. A. Wereszczak, "Improved Sintered Silver Joints via Controlled Topography of Electronic Packaging Subcomponents," US Patent 8,822,036 B1, September 2, 2014.

[2] A. A. Wereszczak, D. J. DeVoto, and P. P. Paret, "Perimetric Structure for Improved Reliability in Electronic Device Interconnection," Invention Disclosure 201303197, DOE S-124,788, October 2013.

[3] R. Wiles and A. A. Wereszczak," Motor Size Reduction via Use of Novel Phase Change Materials," Invention Disclosure 201303197, DOE S-124,788, October, 2013.

[4] Z. Liang, "Integrated Packaging of Multiple Double Sided Cooling Planar Bond Power Modules," DOE S-number S-124,816, invention disclosure number 201303211, December 5, 2013.

[5] Z. Liang, P. Ning, F. Wang, and L. Marlino. "Power Module Packaging with Double Sided Planar Interconnection and Heat Exchangers," US Patent application publication, US 2013/0020694 A1, January 24, 2013.

3.2 Power Electronics Inverter R&D

Madhu Chinthavali (Principal Investigator)

Oak Ridge National Laboratory
National Transportation Research Center
2360 Cherahala Boulevard
Knoxville, TN 37932
Phone: 865-946-1467; Fax: 865-946-1262
Email: chinthavalim@ornl.gov

Burak Ozpineci, ORNL APEEM Program Manager
Phone: (865) 946-1329; Fax: (865) 946-1262
E-mail: burak@ornl.gov

Susan A. Rogers, DOE Program Manager
Phone: 202-586-8997; Fax: 202-586-1600
Email: Susan.Rogers@ee.doe.gov

Start Date: October 2013
Projected End Date: September 2015

Objectives

- Overall
  - Integrate wide bandgap (WBG) technology and novel circuit architectures with advanced packaging to reduce cost, improve efficiency, and increase power density.
- FY 2014
  - Design, build, and test two 10 kW WBG-based prototypes using advanced packages:
    - ORNL module-based liquid-cooled inverter
    - ORNL optimized air-cooled inverter

Technical Targets

- Evaluate WBG devices and develop loss models
  - Acquire, test, and characterize newer-technology WBG power devices, including static and dynamic characterization tests.
- Design, build, and test a 10 kW air-cooled inverter
  - A 10 kW air-cooled inverter will be designed using silicon carbide (SiC) metal oxide semiconductor field-effect transistors (MOSFETs) and Schottky diodes. The modules developed under the packaging project will be used in building the inverter.
- Design, build, and test a 10 kW liquid-based prototype with advanced packages
  - Design a 10 kW liquid-cooled inverter using SiC MOSFETs and Schottky diodes. The prototype will be a liquid-based system.

Accomplishments

- Acquired, tested, and characterized SiC MOSFETs, a SiC junction field-effect transistor (JFET), and SiC junction barrier Schottky (JBS) diodes.
- Completed design, build, and testing of an all-SiC 10 kW inverter using a state-of-the-art commercial all-SiC module.

✧ ✧ ✧ ✧ ✧

Introduction

There is an increasing need for higher-temperature operation of power electronics in automotive applications. The ability of components to operate reliably at elevated temperatures can enable cost and weight savings by making it feasible to reduce the sizes of heat sinks and eliminate secondary cooling loops. Additionally, devices capable of increased-frequency operation can reduce requirements for passive components, leading to further reductions in cost, weight, and volume. WBG devices, specifically SiC and gallium nitride semiconductors, are emerging technologies that enable operation at higher temperatures and frequencies, as well as efficiency and reliability improvements. The development of WBG devices promises to help achieve these goals as well as the VTO targets. WBG technology assessment performed under this project will help to determine when a viable market introduction of these devices for automotive use will occur. The independent assessment of devices for the automotive industry is carried out to monitor progress and provide data readily when the need arises.

It should be no surprise that none of the electric drive vehicle traction drive systems on the market can meet cost and efficiency goals. Efficiency is achieved by using lower-loss devices and materials, which tend to be expensive, even as quantity levels increase. A case in point is motor lamination steel, lower-loss grades of which are manufactured using novel processes that add more cost.

Problems associated with power electronics for advanced vehicle applications include

- Low efficiency at light load conditions for inverters and converters
- Low current density and device scaling issues for high-power converters
- Lack of reliable higher-junction-temperature devices
- High cost of devices and power modules, especially for WBG and advanced silicon (Si) devices
- High number of components for low-voltage electronics (e.g., gate drivers, controllers, sensors)
- Lack of standardized high-power-density, low-cost power modules for scalable and modular power converters
- Substrates that use expensive ceramics for thermal stability and reliability

- Low-cost, low-loss magnetics and high-temperature films for capacitors

The goal of this research is to reduce the size and weight of power converters to meet the 2015 and 2020 inverter targets. The overall strategy for cost reduction is shown in Figure 1. The specific strategy is shown in Figure 2. Cost reduction can be achieved by

- Reducing the size and weight of the power inverters to meet the 2015 inverter targets of 12 kW/l and 12 kW/kg.
- Reducing costs by
  - decreasing the component count by integrating functionality
  - eliminating the existing liquid cooling loop
  - cutting manufacturing costs (part count and steps)
  - reducing the use of high-cost materials, like copper, through bus bar optimization and current reduction

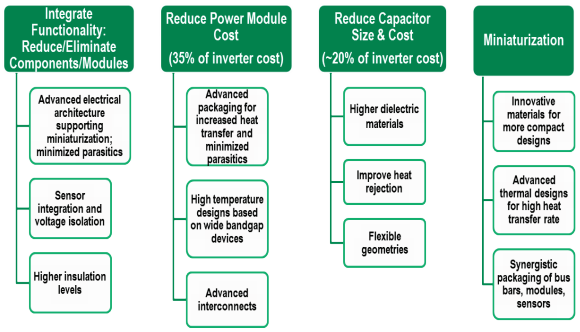

Figure 1: Overall strategy to address limitations of the state of the art.

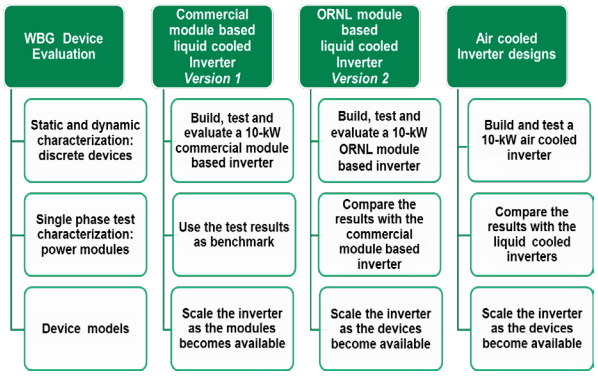

Figure 2: Specific strategy to address limitations of the state of the art.

Approach

The overall objective of this project is to design and develop a WBG 30 kW continuous 55 kW peak power inverter. WBG devices offer some distinct advantages over their Si counterparts. Primarily, they can operate at higher junction temperatures. This benefit allows for hotter coolant and smaller heat sinks and can potentially facilitate air cooling without sacrificing performance. Many of the typical components in a commercial inverter cannot withstand the desired operating temperature of WBG devices, i.e., the capacitor and gate driver. Thus the whole inverter must be considered in the development of new high-temperature packages.

The design innovations in this project include the following

- The design concept uses layers of high-temperature thermal insulating material to separate the low-temperature components from the high-temperature zone.
- It uses the high-temperature operating capability of WBG devices to enable air cooling and uses newer fast-switching Si insulated gate bipolar transistors for high-temperature-liquid designs.
- The innovative heat sink design minimizes thermal resistance.
- The design is optimized for the most frequently operated points.

These new concepts will increase the power density and decrease the volume and weight for electric-base vehicle traction-drive inverters and will achieve the DOE 2020 weight, volume, and efficiency targets.

Results

Device Testing

The new WBG devices acquired this year are 1200 V, 30 A SiC MOSFETs. On-state characteristics and switching energy losses of the devices were obtained over a wide temperature range. All the devices obtained were experimental samples. The static characteristics and switching energy losses of two types of SiC MOSFETs with a TO-247 packaging case are presented and compared. One is a single 1200 V, 30 A SiC MOSFET; the other is a 1200 V, 30 A SiC MOSFET co-packaged with an SiC Schottky barrier diode (SBD). Figure 3 illustrates the circuit configuration of the tested devices: M1, Db1, and M2, Db2 are the tested pure SiC MOSFETs and their internal body diodes; Ds1 and Ds2 represent the co-packaged SiC SBD.

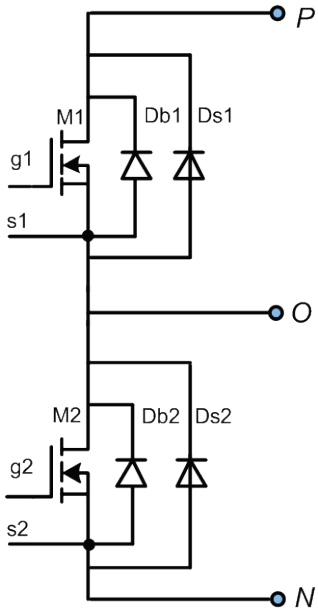

Figure 3: Circuit configuration of the tested SiC MOSFETs.

SiC 1200 V, 30 A SiC MOSFET with Schottky diode

The static characteristics of the 1200 V, 30 A SiC MOSFET and the anti-parallel Schottky diode were obtained over a temperature range of 25 to 175°C. The output characteristics of a 1200 V, 30 A SiC MOSFET at +20 V Vgs for different operating temperatures are shown in Figure 4. The on-state resistance and transconductance of the SiC MOSFET present a positive temperature coefficient, which is beneficial for device paralleling operation.

The forward characteristics of the co-packaged SiC SBD were obtained at +0 V of get bias, as shown in Figure 5. Similar to an Si Schottky diode, the built-in potential of the device is reduced and the equivalent resistance becomes larger at higher temperatures.

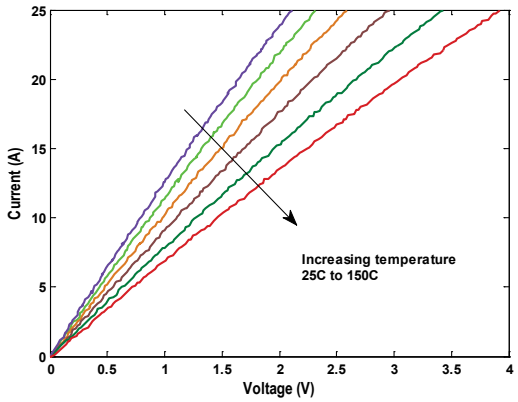

Figure 4: The i-v curves of a 1200 V, 30 A SiC MOSFET.

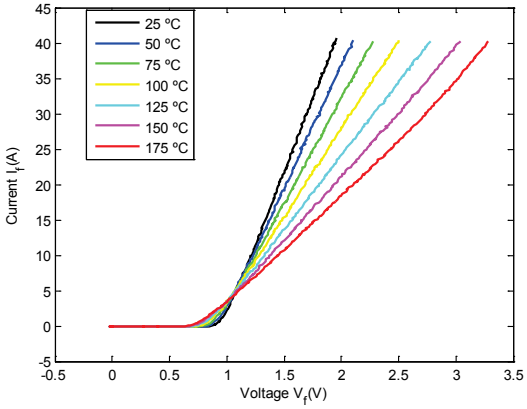

Figure 5: The i-v curves of the co-packaged SiC SBD.

The turn-on and turn-off energy losses of the MOSFET and the Schottky diode were obtained using a double-pulse circuit with a load inductance of 360 µH, as shown in Figure 6. The co-packaged anti-parallel diode was used as the clamping diode in the circuit. The gate driver used for this testing was a commercial gate driver chip.

The data were obtained at 600 Vdc for various currents at 25 and 175°C. As can be observed, the turn-on, turn-off, and total energy losses increase with an increase in current. With a rise in temperature, the turn-on energy loss decreased as a result of a faster switching speed, whereas the turn-off energy loss increased as a result of a slower switching speed. The net result was that the total switching energy loss became somewhat lower at higher temperatures.

The reverse recovery loss of the SiC SBD during the off transient was also evaluated with different current and temperature levels (Figure 7). Compared with the SiC MOSFET, the energy losses of the SiC SBD were negligible since there was almost no reverse recovery phenomenon for the SiC SBD.

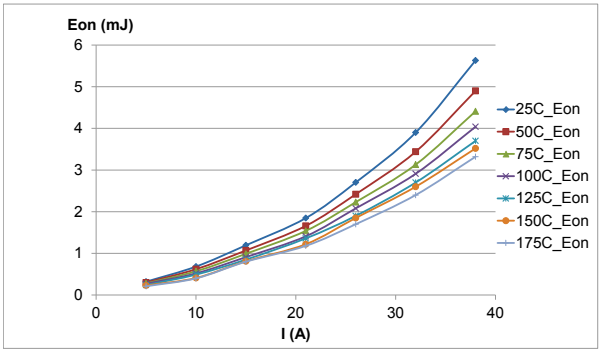

(a) Turn-on loss

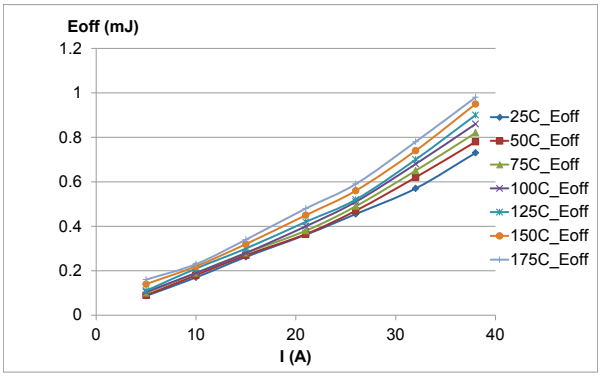

(b) Turn-off loss

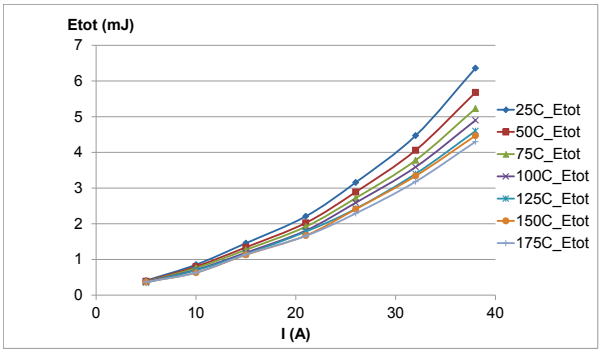

(c) Total loss

Figure 6: Energy losses of 1200 V, 30 A SiC MOSFET with SiC SBD at 600 V.

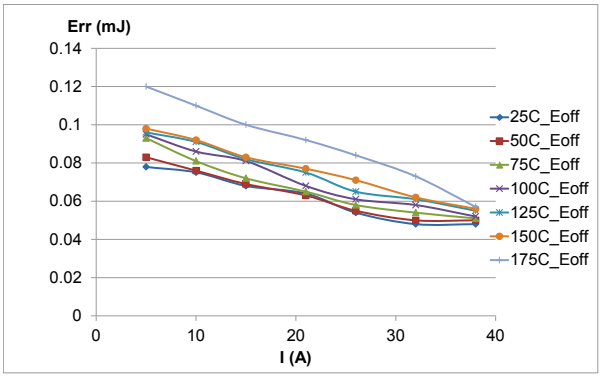

Figure 7: Energy losses of the co-packaged SiC SBD at 600 V.

SiC 1200 V, 30 A SiC MOSFET without Schottky diode

Similarly, the static characteristics of the 1200 V, 30 A SiC MOSFET without a Schottky diode were obtained over a temperature range of 25 to 175°C. The output characteristics of the 1200 V, 30 A SiC MOSFET are shown in Figure 8 with a gate voltage of +20 V. The output characteristics remained nearly the same as those of the SiC MOSFET with the SiC SBD, since the SiC MOSFET dies are the same.

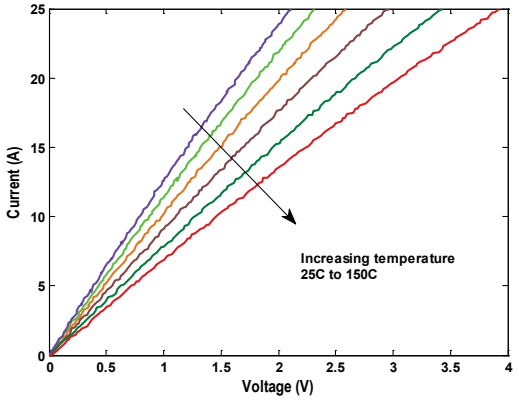

Figure 8: The i-v curves of a 1200 V, 30 A SiC MOSFET.

The forward characteristics of the body diode are shown in Figure 9. With a rise in temperature, the built-in potential decreased as a result of the increase in intrinsic concentration. However, unlike in the SiC SBD, the bulky resistance of the body diode presents a negative temperature coefficient, which may cause a thermal runaway issue during parallel operation. Another issue for the body diode is its high built-in voltage, resulting in much higher conduction losses compared with the SiC SBD.

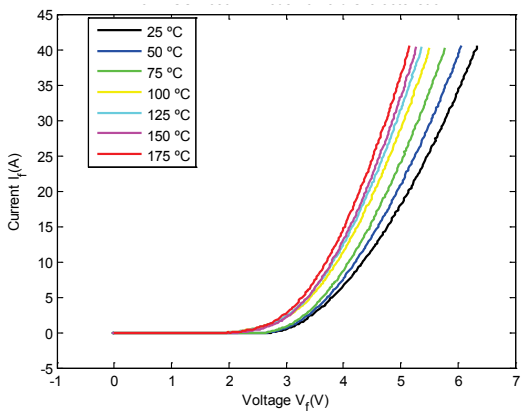

Figure 9: The i-v curves of the body diode of the SiC MOSFET.

The turn-on and turn-off energy losses of the SiC MOSFET without a SiC SBD were obtained under the same testing conditions (600 V, 25 to 175°C), as shown in Figure 10. Compared with the SiC MOSFET with a co-packaged SiC SBD, the total energy loss was a little lower because of a smaller equivalent junction capacitance across the drain to source terminals.

The reverse recovery loss of the body diode of the SiC MOSFET during the off transient was also evaluated at different current and temperature levels (Figure 11). The energy loss of the body diode was somewhat higher than that of the SiC SBD because of the more severe reverse recovery phenomenon; however, it was still negligible.

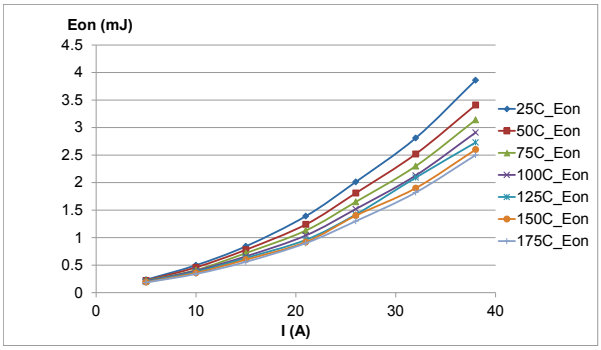

(a) Turn-on loss

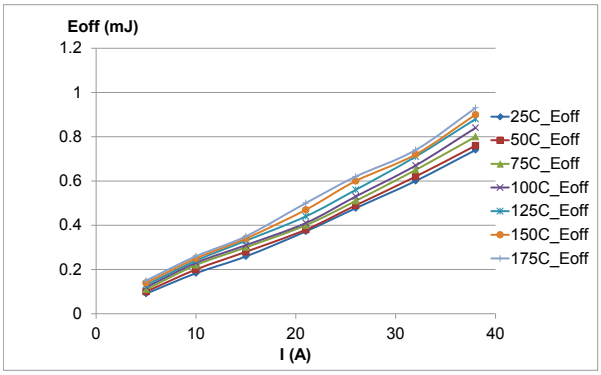

(b) Turn-off loss

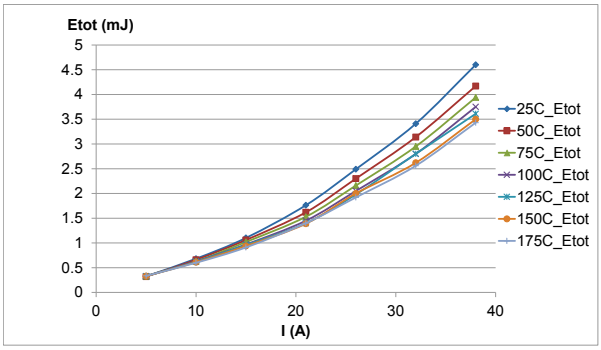

(c) Total loss

Figure 10: Energy losses of 1200 V, 30 A SiC MOSFET without SiC SBD at 600 V.

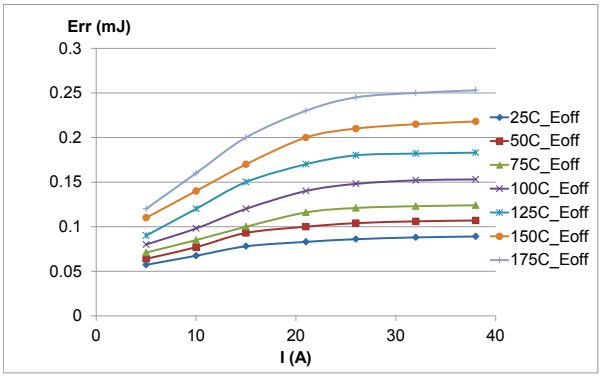

Figure 11: Energy losses of the body diode of the SiC MOSFET.

WBG Inverter Design and Development

Device packages able to withstand high temperatures are required to take advantage of the high-temperature operating capability of WBG devices. Various organizations are working on high-temperature packaging for high-temperature devices. Several high-temperature packages, which include discrete device packages for power modules, have been reported in the past several years. Novel packaging concepts focus primarily on improving the existing packages or on designing new packages using new materials and or processing techniques for better reliability and performance. Even though the novel packages enable the devices to work at higher temperatures, theoretical advantages such as the current density of WBG devices are not realized because of the interconnects needed for the power module to access the device terminals. In addition, the novel designed packages need further development to be used in full systems.

Other factors that limit the system designers from reaping the benefits of WBG technology are the low-voltage electronics and the passive components. This is because even though the packages and the power devices can handle high temperatures, the low-power electronics that drive the power devices, Si-on-insulator (SOI) -based technologies, are limited to a maximum temperature of 200°C. Si-based electronics are limited to 125°C operating temperatures. Although SOI-based electronics can work at up to 200°C, they are expensive. High-temperature (over 200°C) electronics have been reported as being feasible; however, they have not been built to demonstrate their performance capabilities. It could be many years before a logic-level high-temperature transistor can be built. This time lag creates a void in the power module industry, especially for intelligent power module products, which include the electronics inside the module.

Similarly, the passive components in an inverter have a low operating temperature and cannot be operated in close proximity to high-temperature WBG devices. This situation leads to an increase in the volume and a reduction in the power density of the system. High-temperature passive components are currently being developed to address the high-temperature-operation requirement. However, as with the electronic components, they will be much more expensive than the low-temperature components.

To address these problems, a system-level approach for packaging design needs to be developed. Complex 3-dimensional packaging structures with integrated interconnects can reduce the required assembly steps and increase the power densities of power electronic systems. Recent advancements in additive manufacturing (AM) promise an exciting future trend for WBG technology to make inroads into the power electronics industry. AM techniques enable the development of complex 3-dimensional geometries that will result in size and volume reductions at the system level by integrating low-temperature components with high-temperature active devices and reducing the material needed to build the heat exchangers in inverters. ORNL has developed expertise in AM in the last few years. ORNL's PEEM team recognized the potential of this technology for power electronics system packaging and took the first step toward achieving a completely printed inverter concept.

A 10 kW all SiC inverter incorporating an aluminum-based printed power module with an integrated cooling system and a printed plastic lead frame was built using AM techniques. This is the first inverter prototype built using AM. This paper presents the design and development of the inverter and characterization of a high-temperature 1200 V, 100 A all-SiC module. The module development was presented in the FY 2013 VTO annual report. The inverter development and testing are discussed in the following sections.

Inverter Design

Overall design

The current required for a 10 kW inverter can be calculated to be approximately 37 A peak current per phase, assuming the battery voltage to be 350 Vdc with a square mode of operation and a power factor of 0.6. This operating condition represents the worst-case scenario for peak power through the inverter, required to drive the motor. The dc bus capacitors were designed to handle a maximum rms ripple current (~90 A). The capacitors used in this design are not a brick type but are smaller individual capacitors connected in parallel to ensure better cooling and to reduce costs. The cost reduction results from their being off-the-shelf components as opposed to custom-designed brick capacitors with integrated bus bars. A total capacitance of 200 uF was obtained with five 900 V, 40 uF capacitors. The dc bus bars for this inverter were laminated and designed with inserts for each individual capacitor.

The power loss of the 1200 V, 100 A devices (two 50 A SiC MOSFETs and two 50 A diodes) was calculated using the test data obtained through device characterization, as shown in Figures 12 and 13. The loss per device was calculated as a function of power factor, operating voltage, peak current through each device (37/2=~16.5 A per switch), switching frequency, and modulation index. It can be clearly seen that for M=1, the maximum loss for a 175°C maximum junction temperature design was ~30 W. The loss through the diode for M=1 was approximately 16 W. The total loss per switch was ~46 W. This number set the design specifications for the heat removal system for the entire inverter at an operating junction temperature of 175°C maximum. The total loss for the inverter was simply six times the loss per module, which is approximately 276 W. It should be noted that for different values of M and different power factors, the losses would vary between the MOSFET and the diodes. Based on the simulated values, the average efficiency of this inverter is estimated to be around 98–99% over a wide range of operating conditions. A CAD model of the overall inverter design is shown in Figure 14.

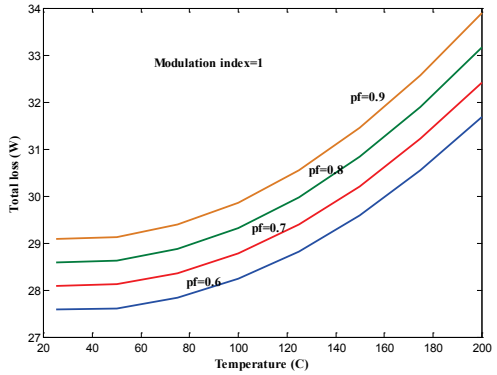

Figure 12: Loss per switch in a 1200 V, 100 A SiC MOSFET module at 350 Vdc, 37 A,10 kHz, and M=1.

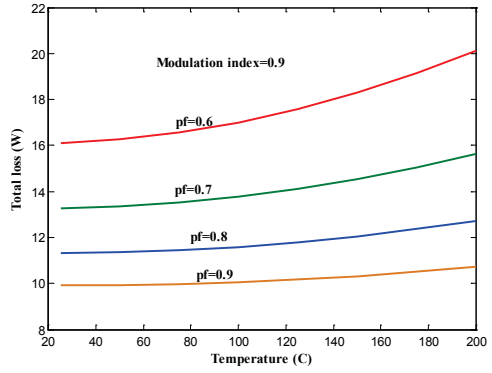

Figure 13: Loss per switch in a 1200 V, 100 A SiC diode module at 350 Vdc, 37 A,10 kHz, and M=0.9.

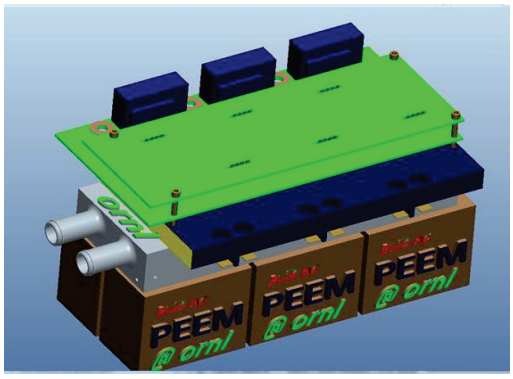

Figure 14: CAD model of the inverter design.

Gate driver design for the module

The gate driver boards were individually designed for each phase leg with separate gate drivers for upper and lower switches (Figure 15). Commercially available gate driver chips from Rohm were used in this inverter. The gate driver has galvanic isolation at up to 3000 Vrms, integrated overcurrent protection under voltage lockout, and temperature feedback features. One important feature of this gate driver is that it has miller clamp protection, which is very important for fast-switching devices like SiC MOSFETs. This feature prevents the upper and lower switch from faulting through switching transients.

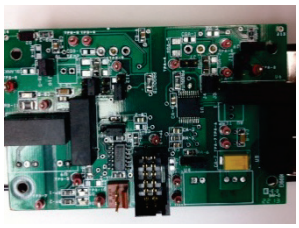

Figure 15: Gate driver board for a single-phase power module.

The driver can provide a peak output current of 5 A with a maximum output resistance of 1 Ω. The maximum rise time is 45 ns for a capacitive load of 10 nF with VCC=24 V, according to the data sheet specifications. Each switch in the phase leg was designed for a gate voltage of 25 V (+20 V to −5 V). The devices were switched with an external gate resistance of 4 Ω to ensure fast turn-on and turn off switching. The peak current required was slightly higher than 6 A, and a buffer stage was added to the output of the gate driver to handle it. The over-current protection circuit was designed using the desaturation detection feature of the gate driver chip. The gate driver protection features were designed and tested using a single-phase test bed.

Cooling system design

The cooling system for this prototype is single-sided cooling for the power module substrates. The heat sink is not a simple conventional structure but capitalizes on AM capabilities to build complex internal structures for better heat transfer capability throughout the unit. This design was used because it allows lower-temperature components to be placed as close to the high-temperature devices as physically possible to achieve two goals: (1) reduce electrical parasitics and (2) reduced volume and mass of the overall system

package. AM (using printed metals) will allow optimized design for heat transfer in the smallest possible package.

With AM, complexity is basically free, so any shape or grouping of shapes can be imagined and modeled for performance. The heat sink used for this inverter is a complex unit made using a direct-melted laser-sintered (DMLS) process, which incorporates flow paths inside the heat sink that allow a complex geometry around the heat-generating paths. Figure 16 shows an x-ray of the internal structure of the printed power module. The x-ray confirms that there are no clogged channels inside the module with unremoved powder or bridged metal structures. Since this is still a maturing technology, it is very important to understand the material properties and compare them with those of conventional aluminum alloys to further improve or optimize the design. A material analysis was performed on the AM power module and compared with analysis results for a regular 6061 aluminum alloy. Figures 17 and 18 show materials analysis results for AM aluminum compared with 6061 aluminum. The results show that the strength of the AM alloy is very similar to that of the 6061 alloy.

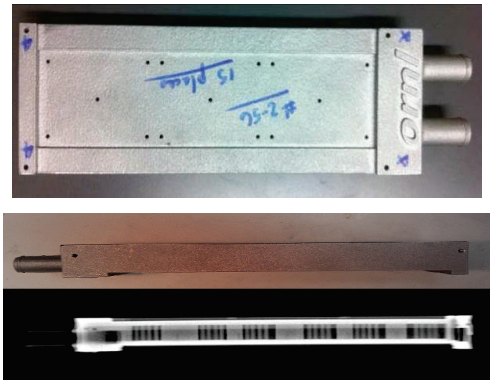

Figure 16: cross-section view of AM model heat sink and x-ray of that view.

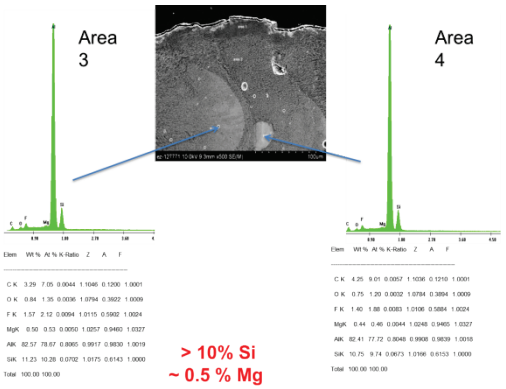

Figure 17: Material composition of AM aluminum ($AlSi_{10}Mg$).

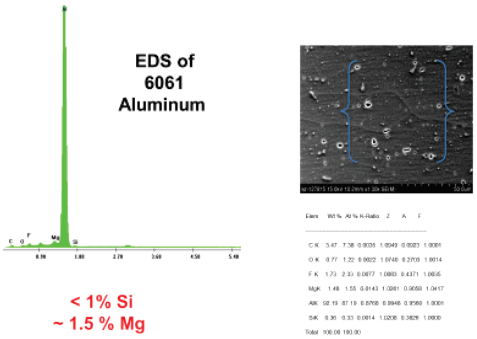

Figure 18: Material composition of 6061 aluminum.

Additional test results in Figure 19 show thermal conductivity comparisons between conventional 6061 aluminum, which is used on many ORNL prototype heat sinks, and the typical AM aluminum alloy used in DMLS, $AlSi_{10}Mg$. ORNL will pursue the development of an aluminum alloy material that works well in the DMLS process and has improved thermal performance. At lower temperatures, 6061 aluminum has a significantly better thermal conductivity than does the AM aluminum, but the conductivity of the two becomes close to equal around 150°C, which is near the center of this inverter's operating range. It would be beneficial to improve the performance in the 100–150°C range for this application.

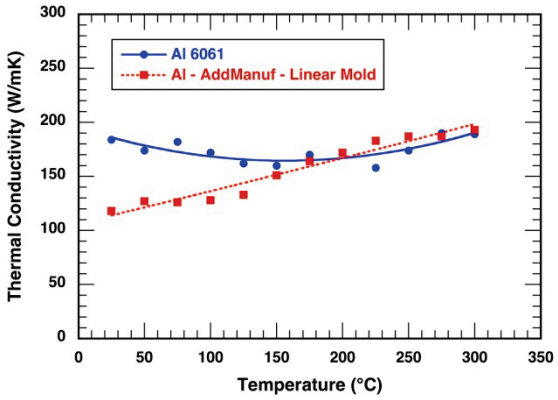

Figure 19: ORNL test results for thermal conductivity for AM aluminum sample ($AlSi_{10}Mg$) vs conventional 6061 aluminum

Inverter Assembly and Testing

The final power module assembly is shown in Figure 20. The direct-bonded copper substrates were directly mounted to the printed module enclosure using spring pressure and thermal grease as the heat transfer medium from the lower side of the direct-bonded copper substrates. The lead frame was built using a plastic printer at the ORNL Manufacturing Demonstration Facility. The bolt holes in the lead frame served as the strain relief structure for the power leads from the substrates. The plastic lead frame also provided the support for the gate driver printed circuit boards and the control board through integrated plastic stand-offs. The material for this first prototype was made using fused deposition melting (FDM) and is common ABS plastic; it can be replaced on the next prototype with an FDM plastic that

has a temperature rating near 200°C. The gate driver leads were soldered to flexible wires and were connected to the gate driver boards. The total volume of the inverter is ~1.5 L. (9.2 × 9.1 × 17.8 cm).

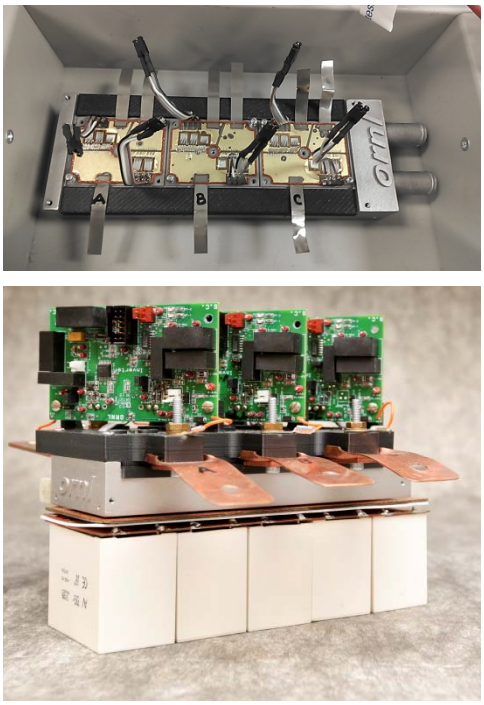

Figure 20: Final assembled inverter and the power module prototype.

The experimental test setup is shown in Figure 21. The test equipment used for this experiment included a Tektronix DPO 7104 1 GHz, TEK differential probe P5205 with 100 MHz bandwidth, and a Tektronix 404 XL current probe. A PZ4000 power analyzer from Yokogawa was used for the power measurements. The neutral point connection from the three-phase resistive load was used for the power measurement setup in the power analyzer. For this test, the dc-link voltage was fixed at a nominal operating voltage (350 V) to the maximum bus voltage (450 V). The load resistance was set to the minimum value, and changing the modulation index controlled the current. The coolant was set at 20°C at a flow rate of 1.5 gpm. The open-loop frequency of operation and the pulse width modulation frequency were fixed, and the current command was varied for a particular dc-link voltage. The command current was increased in steps without exceeding the power rating of the inverter or of the load. The coolant temperature was changed to 60°C, and data were recorded for a wide range of current and switching frequencies. The experimental waveforms for 350 and 450 V operation are shown in Figure 22.

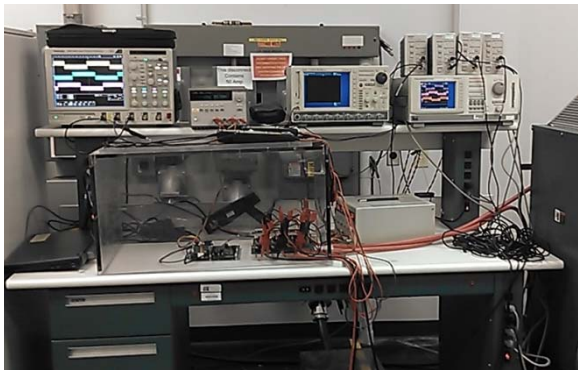

Figure 21: Experimental setup for evaluating inverter performance.

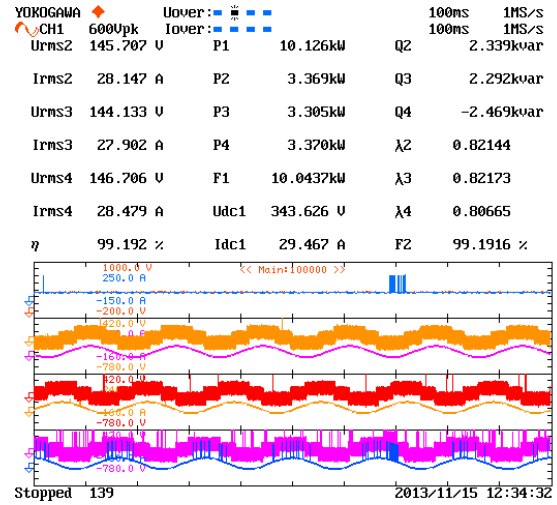

(a)

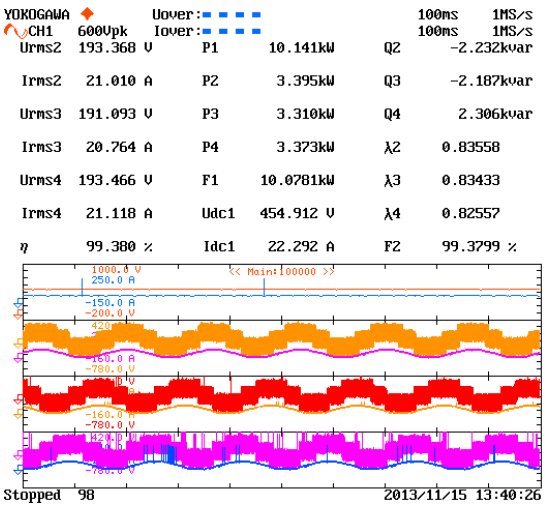

(b)

Figure 22: Experimental waveforms of 10 kW SiC inverter. (a) Screen shot of 350 V dc-link operation; (b) screen shot of 450 V dc-link operation.

The plot of efficiency vs output power for several operating conditions is shown in Figure 23. Inverter efficiencies were higher at the 450 V than at the 325 V operating condition, as expected. Figure 24 shows that the inverter efficiency did not change much as the switching frequency increased. The overall inverter efficiency was ~99% for different operating conditions. The total operating power density based on the test conditions for the inverter was ~7 kW/L, and the designed power density was much higher. This inverter can be further pushed to a higher operating power by increasing the dc-link voltage and current, and a power density at least four times greater can be realized.

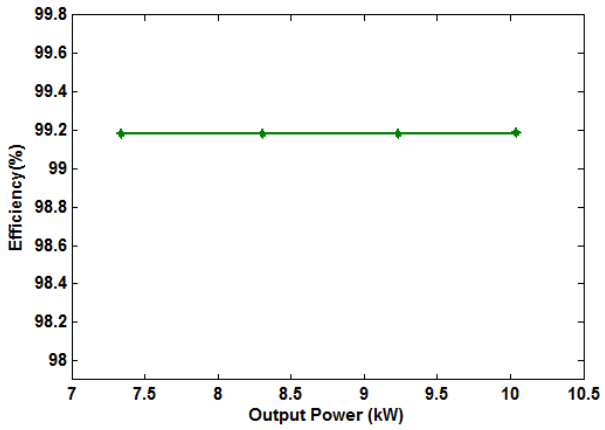

Figure 23: Inverter efficiency vs. output power.

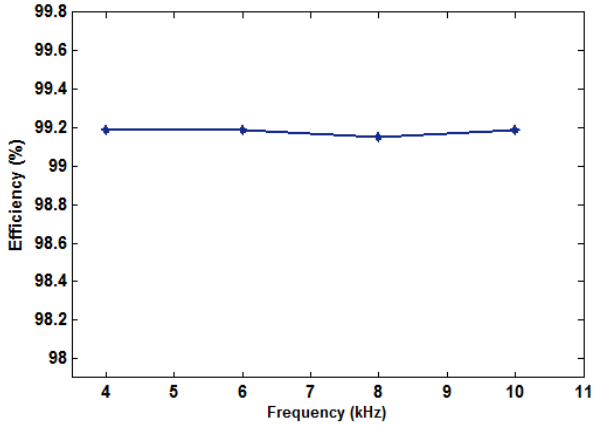

Figure 24: Inverter efficiency vs. switching frequency.

Air-Cooled inverter

ORNL worked with the National Renewable Energy Laboratory (NREL) to develop an air-cooled inverter to further optimize the thermal design. The air-cooled inverter developed in FY 2013 was redesigned using thermal simulations from NREL. The initial inverter size was reduced by 33% through fin design optimization. A balance-of-plant analysis is currently being conducted to establish the feasibility of air cooling at the system level. The new module design has been fabricated and tested for heat transfer. The design was modified by ORNL and redesigned with 1200 V, 100 A MOSFET and Schottky diodes. The module and the inverter assembly are shown in Figures 25 and 26.

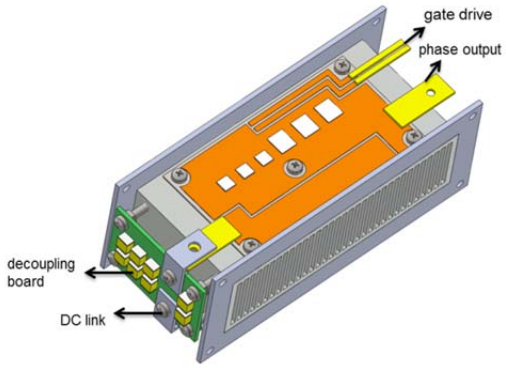

Figure 25: Air-cooled inverter module layout.

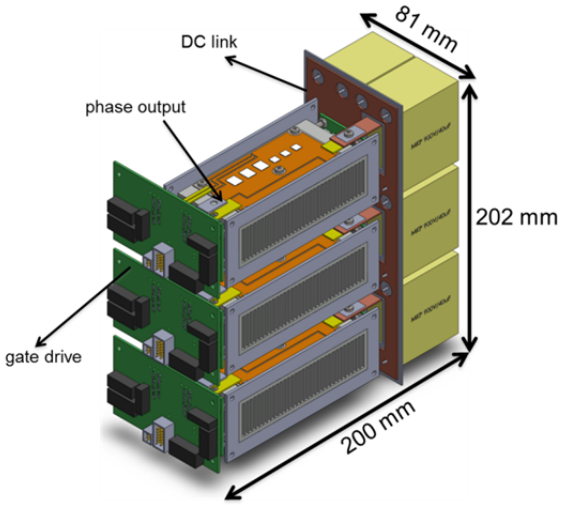

Figure 26: Air-cooled inverter design layout.

Conclusion and Future Directions

WBG device evaluation will continue until the technology transitions to industry. Design, development, and testing of a SiC inverter with a printed power module AM heat sink was presented. The total operating power density of the laboratory prototype inverter is ~7 kW/L and the average operating efficiency of the inverter for a wide range of operating conditions is around 99%. However, based on the design, the power density can potentially be four times greater for higher power with the same power module. This prototype is the first inverter built using AM techniques. The material analysis showed there is no issue with the strength of the AM material compared with that of Al-6061. It was also shown that there is no compromise in the performance of the inverter because of the different material used. From ORNL's perspective, this is the first step toward realizing a full inverter built using AM techniques

The inverter test results obtained this year will be used as a benchmark for next-generation higher power inverters to be built using ORNL's WBG package. The results obtained show that if the inverter is scaled to 30 kW, it will meet the 2020 VTO targets. They also show that WBG technology will aid in achieving U.S. DRIVE targets for volume, efficiency, power density, and system costs.

3.3 Innovative Technologies for dc-dc Converters and On-board Chargers

Gui-Jia Su (Principal Investigator)

Oak Ridge National Laboratory
National Transportation Research Center
2360 Cherahala Boulevard
Knoxville, TN 37932
Phone: (865) 946-1330; Fax: (865) 946-1262
Email: sugj@ornl.gov

Burak Ozpineci, ORNL APEEM Program Manager
Phone: (865) 946-1329; Fax: (865) 946-1262
Email: burak@ornl.gov

Susan A. Rogers, DOE APEEM Program Manager
Phone: (202) 586-8997; Fax: (202) 586-1600
Email: Susan.Rogers@ee.doe.gov

Start Date: October 2013
Projected End Date: September 2016

Objectives

- Overall project objective
  - Develop low-cost, high-efficiency, high-power-density all-wide bandgap (WBG) dc-dc converters and on-board chargers (OBCs). The aim is to reduce charger converter cost by 50% and weight and volume by a factor of 2 compared with the state of the art and provide charger efficiency of more than 96%.
- FY 2014 objective
  - Design, build, and test a 6.6 kW silicon carbide (SiC) isolation converter.
  - Characterize gallium nitride (GaN) devices for OBC and dc-dc converter designs.

Technical Barriers

- Reducing OBC and dc-dc converter cost, weight, and volume.
- Achieving high efficiency.
- Overcoming the limitations of existing semiconductor and magnetic materials to address charger and converter cost, weight, volume, and efficiency targets.

Accomplishments

- Characterized 1200 V/100 A SiC switch phase-leg modules developed in FY 2013 for use in the development of a 6.6 kW OBC prototype.
- Completed design and fabrication of a 6.6 kW isolation converter using the ORNL-designed SiC phase-leg modules and planar ferrite cores.
- Completed tests of the 6.6 kW SiC-based isolation converter that showed a measured peak efficiency of 99.0%.
- Tested and characterized 600 V GaN switches for use in OBC converter designs.
- Completed tests of a baseline 5.8 kW Si-based integrated charger that integrates the segmented traction drive, 14 V dc-dc converter, and high-voltage battery charger dc-dc converter. It showed a peak efficiency of 94.6 % when charged from a 240 V source and 92.0 % when charged from a 120 V source.

✧ ✧ ✧ ✧ ✧

Introduction

The stand-alone OBCs that currently dominate plug-in electric vehicles (EVs) are not cost-effective and have performance limitations that stem from the large component counts of the topologies and limitations in existing semiconductor and magnetic materials. The result is a plateau in charger and converter performance because (1) silicon (Si) switches constrain switching frequencies to less than 100 kHz at power levels of several kilowatts, and (2) inductors and transformers based on soft ferrite magnetic materials further limit power density and efficiency because of low saturation flux densities (~0.38 T) and high core losses at high frequencies. The limitations in switching frequency and material properties result in bulky and expensive passive components—including ac filter capacitors, inductors, and transformers—in currently available OBCs. And passive components contribute more than 30% to the charger cost in state-of-the-art Si-based technology.

As a result, OBCs

- add significant cost (~$106/kW)
- have low power density and specific power numbers (e.g., the 2012 Nissan LEAF 6.6 kW OBC: 0.41 kW/kg, 0.66 kW/L)
- are relatively inefficient (85–92%)
- are unidirectional (can charge the battery but are incapable of vehicle-to-grid support, a highly desirable function in future smart grids)

Emerging WBG devices, including SiC and GaN and advanced soft magnetic materials, are poised to offer significant improvements in ac-dc and dc-dc converters. Their ability to operate with enhanced efficiency over higher frequencies and temperatures minimizes passive component requirements and reduces cooling demands, providing opportunities for revolutionary strides in power conversion.

This project is targeted at leapfrogging existing Si-based charger technology to address charger and converter cost, weight, volume, and efficiency requirements. It proposes to overcome the limitations of existing semiconductor and magnetic materials by using WBG devices, advanced

magnetic materials, and novel integrated charger topologies and control strategies to significantly increase power density, specific power, and efficiency at lower cost.

Approach

The strategy to address the limitations of state-of-the-art OBCs and dc-dc converters is multifold:

- Push the envelope on functional integration of the traction drive, 14 V dc-dc converter, and OBC.
- Take up the challenge of introducing WBG materials, specifically GaN, into automotive applications to determine what performance, packaging, cost, and efficiency benefits can be gained.
- Perform analysis, modeling, and simulation that lead to a functional prototype meeting VTO OBC specific power, power density, and efficiency requirements while significantly reducing the current cost levels.
- Design, build, test, and demonstrate prototypes.
- Work with U.S. DRIVE to develop insights and lessons learned from the automotive community pertinent to dc-dc converters and OBCs.
- Collaborate with industry stakeholders, universities, and other national laboratories to maximize the impact of this work.

Three technical approaches are being pursued. First, integrated bidirectional WBG OBCs will be developed that (a) provide galvanic isolation; (b) provide an integrated function for dc-dc conversion of high voltage to 14 V; (c) use soft switching at the dc-dc stage to reduce electromagnetic interference (EMI) and improve efficiency. Figure 1 shows an integrated dc-dc converter and charger architecture consisting mainly of an ac filter, a WBG front active converter, a dc bus capacitor, and a WBG isolation converter. The isolation converter integrates the functions for charging both the high-voltage traction battery and the 14 V battery for vehicle accessory loads. It includes high-frequency transformers and dc filters as well as WBG switches.

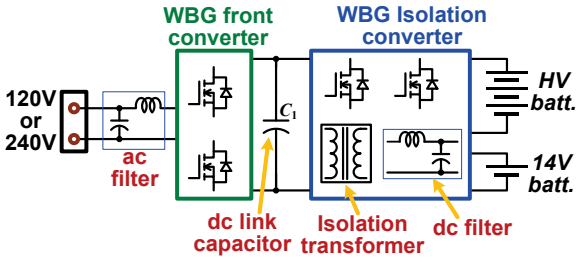

Figure 2: An integrated dc-dc converter and charger architecture.

Second, increasing power density and specific power without compromising efficiency is aggressively pursued by exploiting high switching frequency with WBG devices (especially GaN switches) and using advanced soft magnetic materials (nanocomposites) to drastically reduce the cost, weight, and volume of the ac and dc filters and isolation transformer. Because the availability of WBG power modules is limited, SiC and GaN devices are purchased or obtained directly from device vendors and tested, characterized, and packaged for use in converter design and prototype development. Prototypes will be built and tested first using SiC devices—for which wafer processing and device fabrication technologies have advanced to the stage that SiC metal oxide semiconductor field-effect transistors (MOSFETs) and other switches are available commercially—and then GaN switches as that technology matures and devices with high current ratings become available.

Third, further integration with traction drive systems is employed to reduce the component count for OBCs. For instance, WBG traction drive inverters and motors will be operated as the active front converter and used to replace the ac filter inductor, significantly reducing OBC cost, weight, and volume.

Finally, a control strategy for the isolation converter has been developed to shrink the bulky dc link capacitor. Without the control, this bulky capacitor is necessary to filter out the large voltage ripple— with twice the grid supply frequency—inherent in single-phase ac-dc converters. The proposed control strategy enables a 60% reduction in the ripple current and thereby a significant size reduction in the bulky dc link capacitor in the front ac-dc converter.

Figure 2 shows the integrated isolation converter topology selected through simulation. It consists of a dual H-bridge phase shift dc-dc converter and a 14 V buck converter coupled through a high-frequency transformer. One H-bridge is connected to the high-voltage traction battery and the other to the active front ac-dc converter. Sharing of the transformer (for galvanic isolation) and other switch components between the OBC and the 14 V converter leads to substantial cost, weight, and volume savings for the OBC compared with a stand-alone counterpart. Other features of the integrated charger include these:

- It provides bidirectional power flow and thus can offer additional desired functions, such as vehicle-to-grid and vehicle-to-home applications.
- It can charge the 14 V battery from the grid in addition to normal operation from the high-voltage traction battery.
- It uses the parasitic capacitance of the switches and the transformer leakage inductance to achieve zero-voltage switching for EMI noise reduction and efficiency improvement.
- The dual H-bridge converter enables the OBC to charge the battery over a wide range of voltages by providing a voltage buck and boost function through phase shift and duty ratio control.

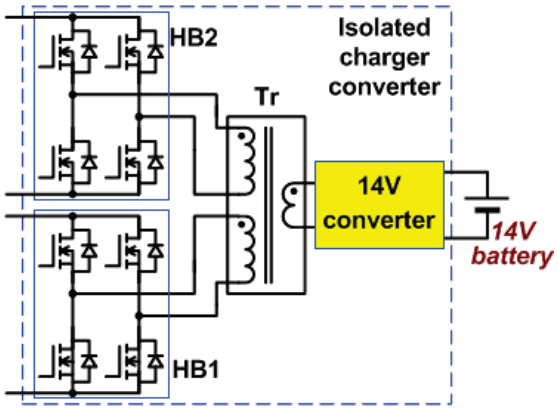

Figure 3: Isolated charger converter topology.

Figure 3 shows an example of the proposed integrated architecture, in which an OBC is integrated into an electrical drive system based on the segmented traction drive topology. Specifically, it consists of a high-voltage (HV) battery, a segmented traction drive system, two sets of contact switches (CS_1 and CS_2), and an isolated charger converter. The segmented traction drive system is formed by splitting the switches of the inverter/converter (INV/CONV) and the stator windings of the motor/generator (MG) into two groups and connecting each group of switches and windings to form a drive unit. The major benefit of the segmented traction drive is the significant (>60 %) size reduction of the dc bus capacitor enabled by interleaved switching by the two drive units [1].

The neutral points of the two stator winding groups (N_1 and N_2) are brought out to a charging port through a third contact switch (CS_3). In addition, as in a stand-alone charger, a filter of common mode and differential mode is usually needed to filter out switching harmonics and common mode noises to meet power quality standards and safety regulations. The differential mode filter is typically realized with a capacitor and an inductor connected across and in series, respectively, with the charging port. One advantage of the integrated charger is that the motor is used as the filter inductor (as described later), thus eliminating the external filter inductor altogether or significantly reducing its inductance if the motor leakage inductance is not sufficient.

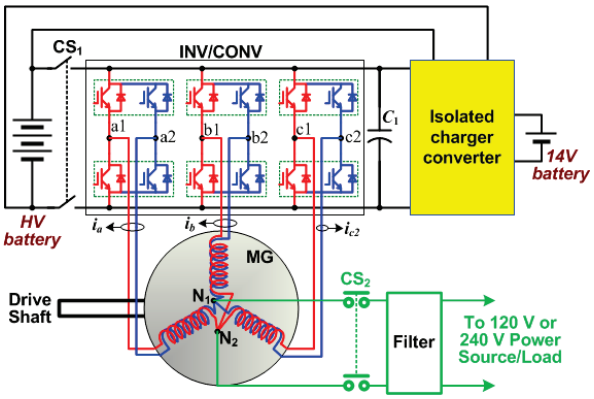

Figure 4: An example of the proposed integrated OBC based on the segmented traction drive topology.

The drive system operates in one of the three modes: (1) providing the propulsion force for driving the vehicle (propulsion mode), (2) charging the HV battery (charging mode), or (3) supplying power to external loads (sourcing mode).

In the propulsion mode, contact switch CS_1 is closed and CS_2 is open, connecting the HV battery to the drive units while disconnecting the charging port from the drive units. The two drive units operate with interleaved switching to reduce the dc bus ripple current, and thus the required size for the dc bus capacitor, and to control the speed and/or torque of the MG according to the amount of power required to propel the vehicle. Two current sensors, i_a and i_b, that measure the combined current of phases *a* and *b*, respectively, are used in the motor control. In the meantime, the H-bridge, HB2, and 14 V converter operate to charge the 14 V battery from the HV battery.

In the charging mode, contact switch CS_1 is open and CS_2 is closed, disconnecting the HV battery from the drive units while connecting the charging port to the drive units. All the switch legs in each INV/CONV of each drive unit collectively function as a single switch leg. The MG functions as an inductor, which is made possible by the motor's zero sequence (ZS) impedance network (ZSIN). Together, the two drive units form a single-phase front converter to regulate the dc bus voltage and perform power factor correction, drawing power from the external source. A third, smaller current sensor, i_{c2}, is used to sense the grid current for use in the controller of the front converter. Moreover, the H-bridge, HB1, operates off the dc bus and supplies, through the transformer, a high-frequency voltage to HB2, which converts the high-frequency voltage to a dc voltage to charge the HV battery. If needed, the 14 V converter can also convert the high-frequency voltage to a dc voltage to charge the 14 V battery. In this mode, the motor functions as a coupled inductor; and the ZS current will not generate a rotating air-gap flux and thus will not produce any torque.

In the sourcing mode, the power flow is reversed from that in the charging mode. The two drive units form a single-phase inverter to supply external loads or the utility grid. In this mode, the H-bridges operate to supply dc power from the HV battery to the single-phase inverter, which in turn converts the dc power to ac power to the external load. If needed, the 14 V converter can be activated to charge the 14 V battery.

During operation in the charging and sourcing modes, the motor is used as a filter inductor that is the ZS network. The grid current splits into three equal parts, and each part flows in each branch of the motor ZS network; therefore, the currents do not produce air-gap flux or generate any torque in the motor.

Figure 4 shows a control block diagram for INV/CONV1 and INV/CONV2. The purpose of these control blocks is twofold: to maintain a constant dc bus voltage at a commanded level of V_{dc}^* and maintain a near-sinusoidal grid current with a near-unity power factor (or a commanded value for reactive power compensation) and a low harmonic distortion factor. The dc bus voltage control loop is implemented with a proportional integral (PI) regulator, which generates a portion of the amplitude (I_s^*) of the current command, i_s^*, for the grid current control loop. The other part of the amplitude of the current command is provided by a feed-forward compensation determined by the battery charging power command, P_{bat}^*, modified by a feed-forward gain, k_{ff}. The battery charging power command is generated in the charger converter controller and is described below. The current regulator, GI, can be a simple gain block of a relatively high value; and a sine-triangle comparator can be used to generate pulse width modulated (PWM) gating signals for the two INV/CONVs. It was found, however, that hysteresis control yields better performance in terms of lower switching losses and current harmonic contents, and it was thus employed in the test setup.

As shown in Figure 4, low pass filters (LPFs) are used in the feedback paths to remove the high-frequency components in the sensed voltages and currents. Since only a portion of the grid current is directly measured with the smaller current

sensor, i_{c2}, the grid current can be computed—assuming the grid current is shared evenly among the three leads—by

$$i_s = 3i_{c2}, \quad (1)$$

where i_{c2} is half-phase *c* motor current. Note the three-phase structure of the INV/CONVs and ZSINs enables the use of interleaved switching to reduce switching losses.

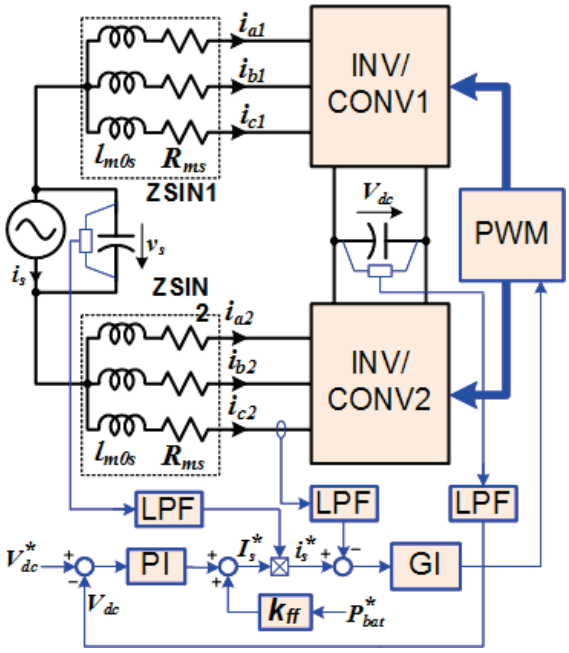

Figure 5: Control block diagram for INV/CONV1 and INV/CONV2.

Figure 5 shows a control block diagram for the charger converters, HB1 and HB2. The purpose of this control is to maintain a constant battery terminal voltage at a commanded level of V_{bat}^* in the CV charging mode or a constant current at a commanded level of I_{bat}^* in the CI charging mode. A software switch, $\mathbf{S}_{VI}$, is used to select the charging mode according to the state of charge of the battery. Again, a PI controller is used to regulate the battery voltage or current. Because of the significantly smaller dc bus capacitor in the segmented inverter, the dc bus voltage, V_{dc}, will fluctuate to a greater degree during operation in the single-phase charger mode. To prevent it from causing a large ripple component in the battery charging current, the PI output is divided by the high-frequency component of V_{dc}, obtained with a band-pass filter (BPF) and then fed to the PWM block, which controls the duty cycles. It also regulates the phase shift between the two H-bridges, if needed.

In addition, the battery charging power command, P_{bat}^*, is computed by

$$P_{bat}^* = \begin{cases} V_{bat}^* I_{bat}, \text{in CV charging mode} \\ I_{bat}^* V_{bat}, \text{in CI charging mode} \end{cases}, \quad (2)$$

where V_{bat} and I_{bat} are the measured battery terminal voltage and current. As mentioned, P_{bat}^* is used in the feed-forward compensation in the grid current control loop to improve the dynamic response of the dc bus voltage loop.

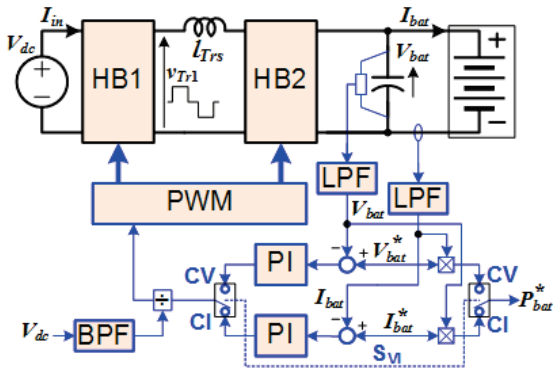

Figure 6: Control block diagram for HB1 and HB2.

An Si-based 5.8 kW prototype consisting of an electrical drive system and an isolation converter was built to test the charging function and verify the selected topology. The isolation converter and the experimental results will serve as the baseline for comparison with WBG-based prototypes being developed under this project. The drive system consists of a segmented inverter rated at 55 kW and a commercial, off-the-shelf, induction motor rated at 14.9 kW, 230 Vrms, 45.4 Arms. The motor has two poles and two sets of stator windings with all leads accessible. Figure 6 shows photos of the inverter and test motor. The 55 kW segmented inverter was fabricated with two pieces of 600 V/300 A six-pack of intelligent IGBT modules and two film dc bus capacitors, each rated at 500 V and 200 µF. These components are mounted on a 6×7 in. (15.24 × 17.78 cm) water-cooled cold plate.

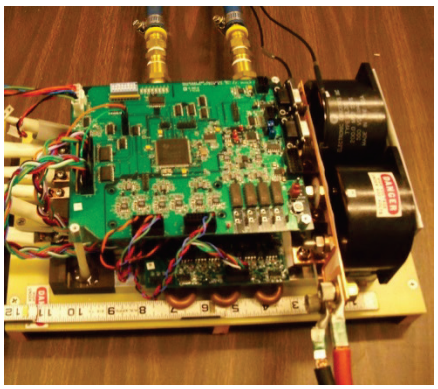

(a) Segmented inverter

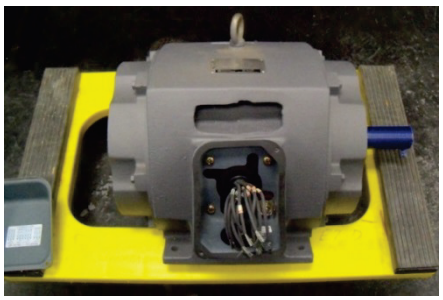

(b) Induction motor

Figure 7: Photos of the traction drive inverter and motor used in the integrated charger tests.

Because of its relatively low power rating, the measured ZS resistance of the motor is quite large. The plots in Figure 7 show the measured ZS resistance and inductance of the test motor at 60 Hz. The ZS inductance, decreasing from 1.9 to 1.1 mH as the currents increases from 5 to 30 A and the motor cores saturate, is sufficient for the inductor-capacitor filter. Because of its relatively low power rating, the measured ZS resistance of the motor is quite large, around 315 mΩ, compared with those of production EV/hybrid EV motors. For example, the measured ZS resistance of the Toyota Camry motor is 10.75 mΩ. The high-resistance test motor will have a significant impact on the measured charger system efficiency in the following test results.

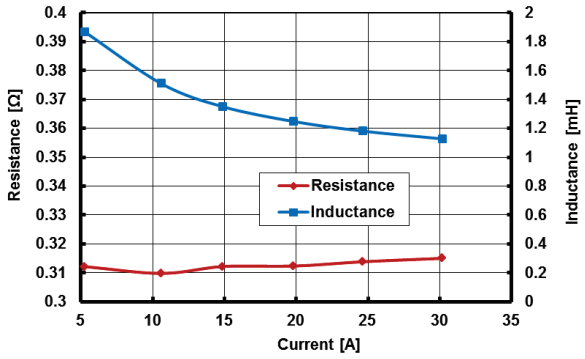

Figure 8: Measured ZS resistance and inductance of the test motor.

The charger converter prototype is rated at 5.8 kW and was fabricated using Si power MOSFETs and a planar transformer that has two HV windings and one 14 V printed circuit board (PCB) winding using heavy copper traces. The parasitic capacitances of the MOSFETs are used for zero voltage switching. Figure 8 is a photo of the charger converter prototype. All the components are mounted on an aluminum cold plate with a foot print of 6×7 in. Gate driver PCBs are then mounted directly over the MOSFETs to eliminate wire connections between them. In addition, a control PCB using a TI TMS320F1208 fixed-point digital signal processor (DSP) controller located on the top is used to implement the dc bus voltage, grid current, battery charging voltage, and current control blocks.

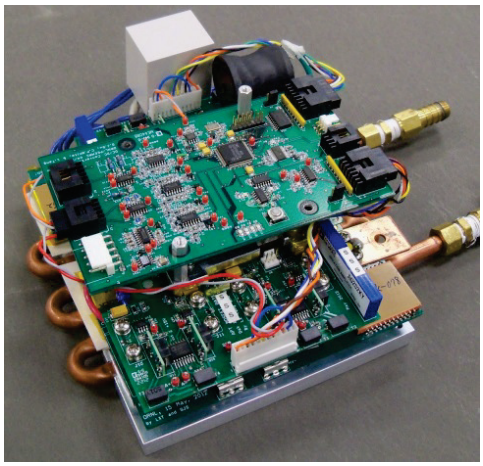

Figure 9: Photo of the 5.8 kW Si-based charger converter.

Results

Si-based isolation converter and charger system tests

The charger converter and the segmented traction inverter and test motor were combined to create an integrated OBC, and the whole charging system was tested successfully with a resistive load bank at both 120 and 240 V grid voltages. Representative waveforms are included here to illustrate the operations of the integrated charger. Figures 9 and 10 show typical operating waveforms of the system with a 120 V input voltage and charging power of 1.0 kW and 2.9 kW, respectively. Figures 11 and 12 give waveforms of the system with a 240 V grid voltage and charging power of 3.3 and 5.8 kW, respectively.

Figure 13 plots measured and estimated system efficiencies of the integrated charger. The estimated efficiency numbers are computed using a ZS resistance of 22 mΩ and considering only the differences in the copper losses. The maximum measured efficiency is 92.9% at a grid voltage of 240 V and 87.0% at 120 V, with respective estimated maximum efficiencies of 94.6 and 92.0%. The fast drop in the measured efficiencies as the input current increases illustrates the impact of the copper losses in the high-resistance motor. It is thus reasonable to expect higher efficiency numbers with production EV/hybrid EV motors, which have much lower stator resistances.

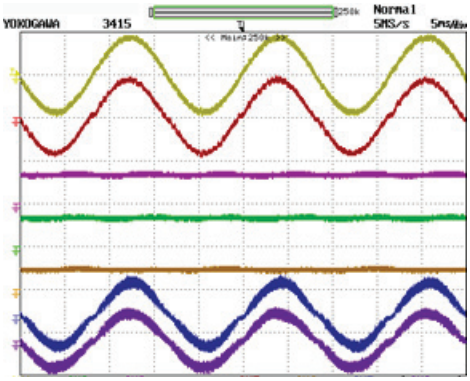

Figure 10: Waveforms of the charger system with 120 V input and 2.9 kW charging power. From top, grid voltage (v_s, 200 V/div, CH1), grid current (i_s, 50 A/div, CH5), dc bus voltage (V_{dc}, 500 V/div, CH3), charging voltage (V_{bat}, 500 V/div, CH2), charging current (I_{bat}, 20 A/div, CH6) and motor phase *a1* and *a2* currents (i_{a1}, CH7, i_{a2}, CH8, 20 A/div).

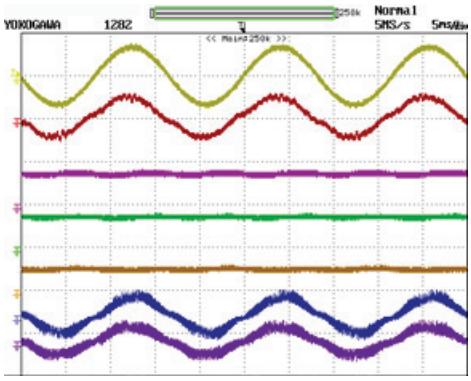

Figure 11: Waveforms of the charger system at 240 V input and 3.3 kW charging power. From top, grid voltage (v_s, 500 V/div, CH1), grid current (i_s, 50 A/div, CH5), dc bus voltage ($V_{dc,}$ 500 V/div, CH3), charging voltage (V_{bat}, 500 V/div, CH2), charging current (I_{bat}, 20 A/div, CH6) and motor phase *a1* and *a2* currents (i_{a1}, CH7, i_{a2}, CH8, 20 A/div).

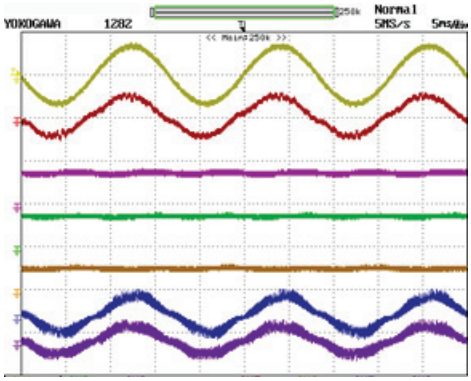

Figure 12: Waveforms of the charger system at 240 V input and 3.3 kW charging power. From top, grid voltage (v_s, 500 V/div, CH1), grid current (i_s, 50 A/div, CH5), dc bus voltage ($V_{dc,}$ 500 V/div, CH3), charging voltage (V_{bat}, 500 V/div, CH2), charging current (I_{bat}, 20 A/div, CH6) and motor phase *a1* and *a2* currents (i_{a1}, CH7, i_{a2}, CH8, 20 A/div).

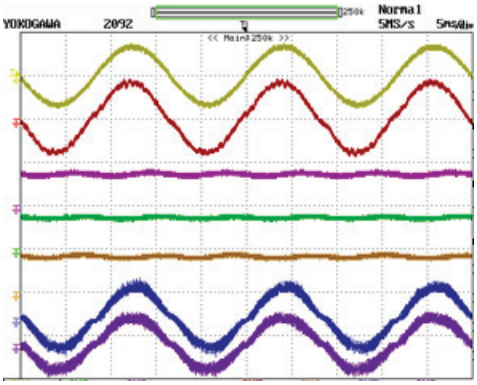

Figure 13: Waveforms of the charger system at 240 V input and 5.8 kW charging power. From top, grid voltage (v_s, 500 V/div, CH1), grid current (i_s, 50 A/div, CH5), dc bus voltage ($V_{dc,}$ 500 V/div, CH3), charging voltage (V_{bat}, 500 V/div, CH2), charging current (I_{bat}, 20 A/div, CH6) and motor phase *a1* and *a2* currents (i_{a1}, CH7, i_{a2}, CH8, 20 A/div).

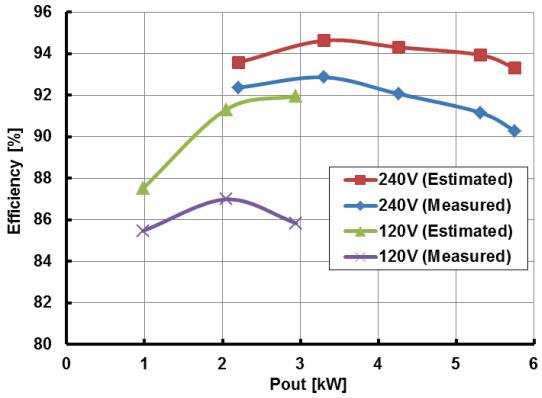

Figure 14: Measured and estimated charger system efficiencies at grid voltages of 120 and 240 V.

GaN device tests

For use in high-voltage charger converter designs, 600 V GaN switches manufactured by International Rectifier (IR) and packaged by Delphi were tested and evaluated for static and switching performance. A test board for characterizing the IR GaN switches was designed and fabricated. The test circuit (Figure 14) is flexible and can be reconfigured for double-pulse tests to measure switching losses and test loads in a half-bridge configuration for efficiency measurement. The IR devices are packaged in a cascade connection of a normally-on GaN high-electron mobility transistor fabricated on an Si substrate, and a low-voltage Si MOSFET, which makes them operate as normally-off switches.

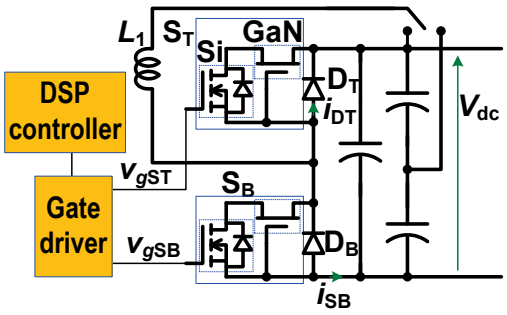

Figure 15: IR 600 V GaN switch test circuit.

Figure 15 plots typical I-V curves for the IR/Delphi 600 V medium-size GaN switches measured with a curve tracer. The medium-size GaN field-effect transistor has a package size of 1.7×3.1cm and a typical R_{dson}=17 mΩ, translating to a specific on resistance of 89.6 mΩ/cm^2. In comparison, the similarly rated Infineon CoolMOS IPW60R041C6 has a package size of 2.1×1.6 cm and R_{dson}=41 mΩ, resulting in a specific on resistance of 137.8 mΩ/cm^2.

Double-pulse tests were performed with the top switch, S_T, kept off or switched complementarily. Figure 16 shows double-pulse test results with S_T kept off and V_{dc}=300 V. Measured switching losses were 275.8 µJ for turn-off and 69.5 µJ for turn-on.

After the double-pulse tests, further experiments were carried out by operating the IR GaN switches in a half-bridge inverter with an inductor load at a dc bus voltage of 320 V and switching frequencies of 100–300 kHz. Figure 17 shows

typical operation waveforms at a switching frequency of 150 kHz. The estimated efficiency is about 98.5% at 1.8 kVA.

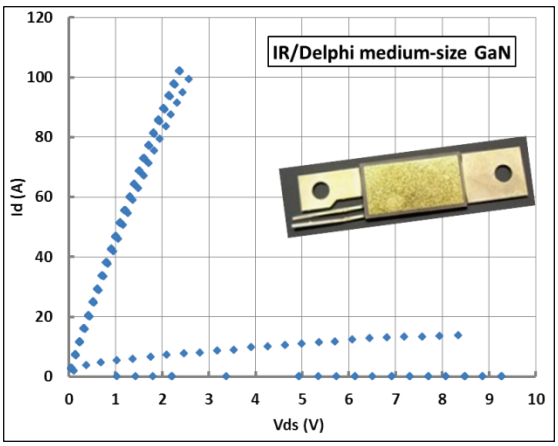

Figure 17: Typical I-V curve for IR/Delphi 600 V medium-size GaN switch.

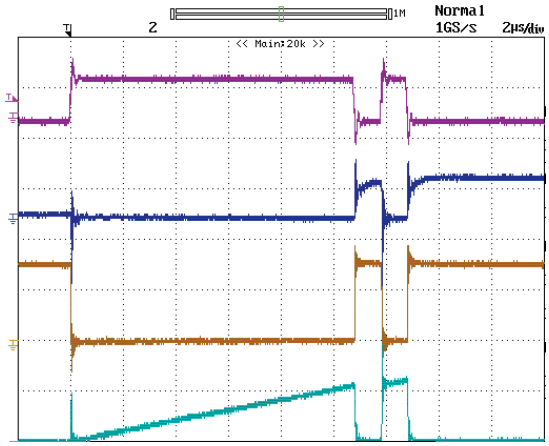

Figure 16: Double-pulse test results with S_T kept off. From top, v_{gSB}, 10 V/div; i_{DT}, 50 A/div; v_{DSB}, 200 V/div; i_{SB}, 50 A/div; 2 us/div.

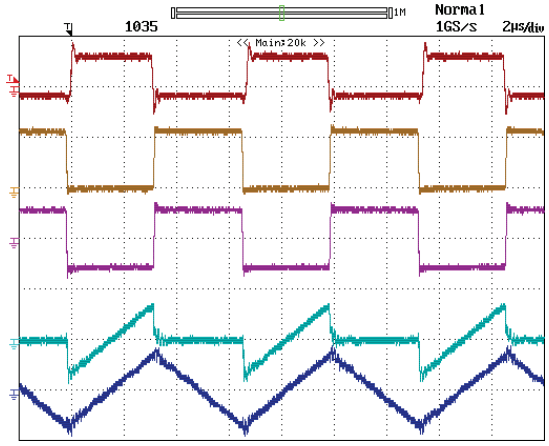

Figure 17: IR GaN switch operation waveforms in a half-bridge inverter with an inductor load. From top, v_{gSB}, 20 V/div; v_{DSB}, 300 V/div; v_{out}, 300 V/div; i_{SB}, 100 A/div; i_{L1}, 100 A/div; 2us/div.

6.6 kW SiC-based isolation converter

SiC switch phase-leg modules rated at 1200 V/100 A were fabricated on ORNL-designed direct bond copper substrates using Cree SiC MOSFETs and Schottky barrier diodes and characterized using a Tektronix curve tracer (Figure 18).

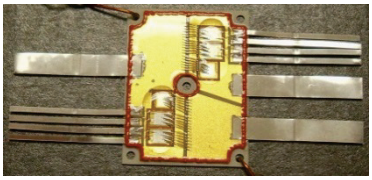

(a) Assembled SiC MOSFET module

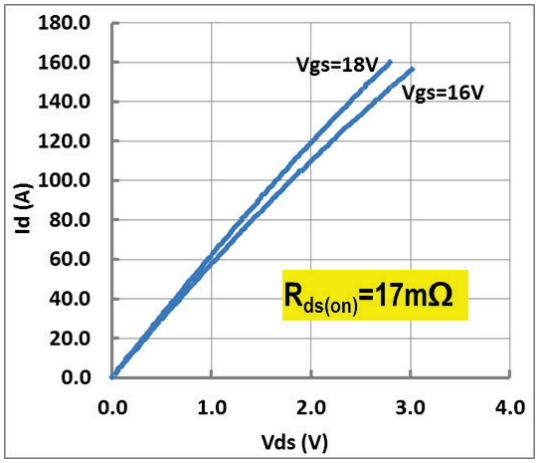

(b) Static characteristics

Figure 18: SiC switch phase-leg modules.

Incorporating the results from the simulation study, a power circuit design for a 6.6 kW isolation converter using the ORNL-designed SiC phase-leg modules and planar ferrite cores was completed and a prototype fabricated. Figure 19 is a photo of the isolation converter. It comprises a primary switch PCB and its gate driver board, a secondary switch PCB and its gate driver board, a 14 V converter board, a DSP control board (top), and a planar transformer assembly. All the components are mounted on a 7×5 in. heat exchanger.

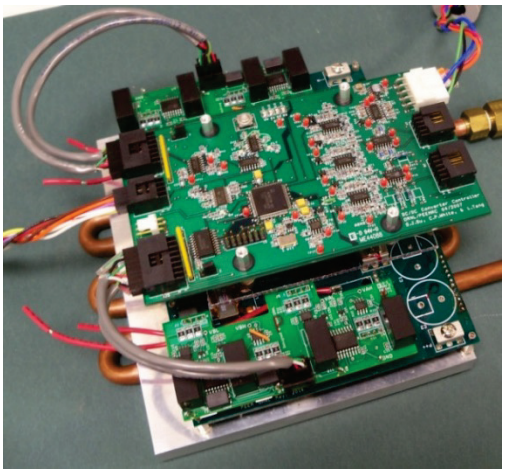

Figure 19: Photo of a 6.6 kW SiC isolation converter.

The DSP control board is based on a TI TMS320F2809 chip, which enables high-resolution (HR) PWM (180 ps vs 10 ns for HRPWM-incapable chips) for the more accurate duty/phase shift control that is needed for high-switching-frequency operation. Converter control code was developed that uses the chip's HRPWM hardware for accurate phase shift control under high-switching-frequency operation with WBG devices.

The SiC-based isolation converter prototype was tested with a resistive load bank. Figure 20 is a photo of the test setup. A programmable dc power supply was used to power the isolation converter. Operating waveforms were recorded with a digital oscilloscope; and input and output voltages, currents, and power were measured with a digital power meter. Figure 21 gives typical operating waveforms, in which V_{dc}, V_{bat}, v_{Tr1}, v_{Tr2}, I_{bat}, and I_{in} are input dc voltage, output dc voltage, transformer primary voltage, transformer secondary voltage, output dc current, and input dc current, respectively.

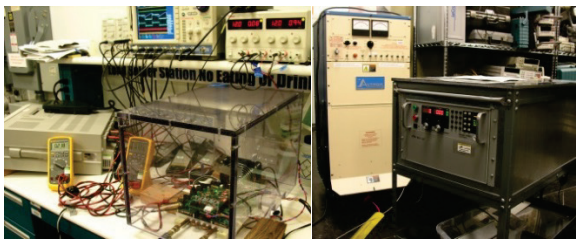

Figure 20: Test setup for the 6.6 kW SiC-based isolation charger converter.

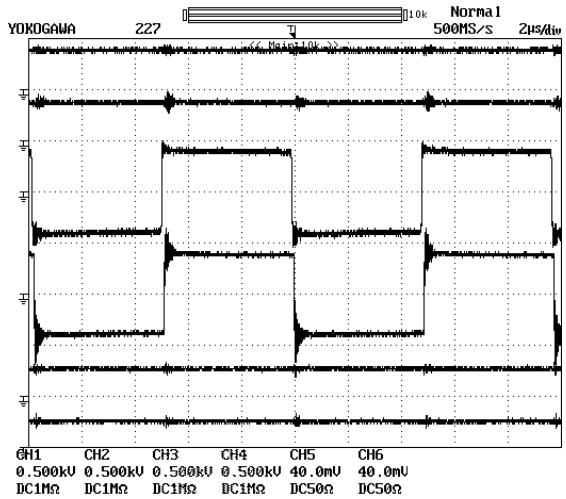

Figure 21: Isolation converter operating waveforms showing, from top, input dc voltage, V_{dc}, 500 V/div; output dc voltage, V_{bat}, 500 V/div; transformer primary voltage, v_{Tr1}, 500 V/div; transformer secondary voltage, v_{Tr2}, 500 V/div; input dc current, I_{in}, 40 A/div; and output dc current, I_{bat}; 40 A/div.

Figure 22 plots measured isolation converter efficiency vs output power. The efficiencies are greater than 97% for output power levels up to 6.66 kW, and the maximum value is 99.0 %.

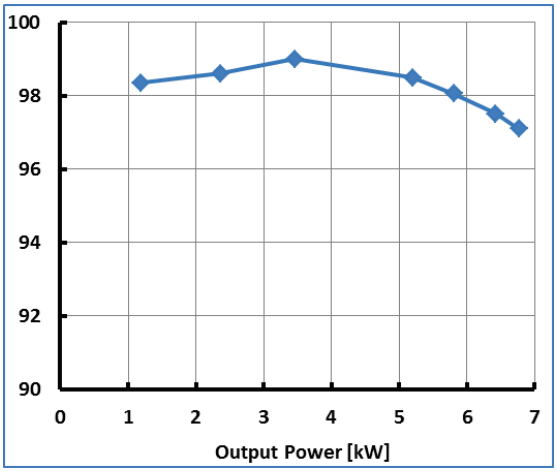

Figure 22: Measured efficiency of the 6.6 kW SiC-based isolation charger converter.

Conclusions and Future Directions

This project is aimed at leapfrogging existing Si-based charger technology to address charger and converter cost, weight, volume, and efficiency. It proposes to overcome the limitations of Si semiconductor and magnetic materials by using WBG devices, including SiC and GaN; using advanced magnetic materials; and employing a novel integrated charger architecture and control strategy.

ORNL has developed a new integrated OBC and dc-dc converter architecture that integrates the segmented traction drive, 14 V dc-dc converter, and HV battery charger dc-dc converter. The new topology significantly reduces the number of components (power circuit components alone are reduced by 47%, not counting savings in gate driver and control logic circuits). ORNL has built and tested a 5.8 kW Si-based prototype employing the new topology, which showed a peak efficiency of 94.6 % when charged from a 240 V source and 92.0 % when charged from a 120 V source. Test results validated the new integrated charger and dc-dc converter architecture and provided a baseline for measuring the benefits of WBG counterparts. ORNL also developed a control strategy for the charger isolation converter to reduce the battery ripple current inherent in single-phase ac-dc converters. Simulation results show the control strategy reduces the ripple current by 60%, enabling a corresponding reduction of the bulky dc link capacitor in the active front end converter.

Emerging GaN devices fabricated on Si substrates are poised to offer significant improvements in charger and dc-dc converters at a cost comparable to that of Si devices. Their enhanced switching speed and reduced switching and conduction losses may enable these switches to minimize passive component requirements, a major driver of cost, weight, and volume in charger and dc-dc converters. ORNL has characterized both low-voltage (<200 V) and high-voltage (600 V) GaN switches and collected valuable design data for hardware development of OBCs and dc-dc converters.

Incorporating the simulation results, ORNL has designed, fabricated, and tested a 6.6 kW isolation converter using the

ORNL-designed SiC phase-leg modules and planar ferrite cores. Test results demonstrated efficiencies of greater than 97% with a peak value of 99.0 %.

Future work will be directed at designing, building, and testing prototypes for a 6.6 kW SiC OBC, a 6.6 kW GaN isolation converter and OBC, and a 2 kW GaN 14 V converter.

FY 2014 Publications/Presentations

[1] G. J. Su and L. Tang, "A new integrated onboard charger and accessory power converter for plug-in electric vehicles," pp. 4790–4796 in *Proceedings of the 6th IEEE Energy Conversion Congress and Exposition (ECCE 2014)*, Pittsburgh, September 14–18, 2014.

[2] G. J. Su, "Innovative technologies for dc-dc converters and on-board chargers," presented at the DOE Vehicle Technologies Program Advanced Power Electronics and Electric Motors R&D FY 2014 Kickoff Meeting, November 5–7, 2013.

[3] G. J. Su, "WBG converters and on-board charger," presented at the 2014 DOE Hydrogen and Fuel Cells Program and Vehicle Technologies Program Annual Merit Review and Peer Evaluation Meeting, June 16–20, 2014.

References

[1] G. J. Su and L. Tang, "A segmented traction drive system with a small dc bus capacitor," pp. 2847–2853 in Proceedings *of the 4th IEEE Energy Conversion Congress and Exposition (ECCE 2012)*, Raleigh, North Carolina, September 16–20, 2012.

[2] Datasheet: http://www.infineon.com/cms/en/product/mosfets/power-mosfets/n-channel-mosfets-coolmos-tm-500v-900v/IPW60R041C6/productType.html?productType=*db3a304426e7f13b0127f2050dcb45ac*.

4.1 Scalable Non–Rare Earth Motor Development

Tim Burress (Principal Investigator)

Oak Ridge National Laboratory
National Transportation Research Center
2360 Cherahala Boulevard
Knoxville, TN 37932
Phone: (865) 946-1216; Fax: (865) 946-1262
E-mail: burressta@ornl.gov

Burak Ozpineci, ORNL APEEM Program Manager
Phone: (865) 946-1329; Fax: (865) 946-1262
E-mail: burak@ornl.gov

Susan A. Rogers, DOE APEEM Program Manager
Phone: (202) 586-8997; Fax: (202) 586-1600
E-mail: Susan.Rogers@ee.doe.gov

Start Date: October 2013
Projected End Date:September 2016

Objectives

- Develop low-cost non–rare earth motor solutions while maintaining high power density, specific power, and efficiency.
  - Develop or utilize new materials.
  - Perform fundamental research to improve motor modeling accuracy
    - Evaluate impacts of factory stamping upon magnetic properties and motor performance
    - Develop advanced modeling algorithms
  - Employ high performance computational tools and resources
  - Design unconventional motor technologies that address DOE 2022 targets

Technical Barriers

- Even without using rare earth permanent magnet (PM) materials, 2022 DOE cost targets are challenging.
- Power density, specific power, and efficiency targets are difficult to meet with alternative motor technologies such as induction, synchronous reluctance, switched reluctance, non–rare earth PM, and field excitation.

Technical Targets

- DOE 2022 motor targets
  - Power density: 5.7 kW/L
  - Specific power: 1.6 kW/kg
  - Cost: 4.7 $/kW

Accomplishments

- Machine design and development
  - Originated and designed two different novel machines (with several sub-designs of each).
  - Identified brushless field excitation (BFE) and synchronous reluctance motor designs through modeling as high-potential candidates to meet targets.
  - Selected a novel synchronous reluctance machine for fabrication.
- Material research and development (R&D)
  - Continued research on electrical sheet steel with high silicon (Si) content (>6%).
    - Confirmed capability for ingot-based processing vs expensive chemical vapor deposition (CVD) process.
    - Developed and confirmed a novel processing technique to reduce brittleness; otherwise, the workability of high-Si steel is not suitable for mass production of motor laminations.
  - Developed new magnetic material characterization systems for innovative analysis of electrical steel magnetic properties.
- Advanced modeling
  - Incorporated findings from research on soft magnetic materials properties, using the new characterization system, into electromagnetics modeling.
  - Developed detailed micromagnetics code and a corresponding simulation environment to study the fundamental behavior and impact of various conditions upon the magnetization and loss characteristics of electrical steel.
- Proof-of-principle fabrication and bench top testing
  - Fabricated a proof-of-principle prototype and began benchtop testing to verify basic parameters of the electromagnetic model.

✧ ✧ ✧ ✧ ✧

Introduction

The electric motor is one of the main components of electrified drivetrains; therefore, improving its efficiency, performance, and cost-effectiveness is crucial to the hybridization and electrification of vehicles. PM motors are not easily surpassed in terms of efficiency, power density, and specific power; that is why almost all hybrid electric vehicles (HEVs) and electric vehicles (EVs) use them. However, the cost of rare-earth PM materials accounts for at least 40% of the entire motor cost; and in the past decade, there has been significant volatility in the price and availability of the rare-earth materials used in PM motors. As a result, automotive manufacturers around the world are seeking alternative non-

rare earth motor technologies that facilitate cost-effectiveness as the HEV and EV markets continue to expand. Therefore, the development of alternative non–rare earth motor technologies has an important role in the future of economic stability, clean energy, and energy independence.

Approach

The primary objective of ORNL's motor R&D is to develop low-cost non–rare earth motor solutions with high power density, specific power, and efficiency. The overall structure of the efforts in the project is described by the diagram in Figure 1. A key task for FY 2014 is motor design and optimization with conventional tools and optimization algorithms, which includes commercial electromagnetic finite element analysis (FEA) packages as well as other design tools developed by ORNL on previous projects.

Many novel electric motor concepts were considered. After candidates with high potential were selected, design optimization algorithms were applied to optimize machine designs with respect to DOE's 2020 power density, specific power, efficiency, and cost targets. For the second level of optimization, beginning in FY 2015, the development process will use feedback from advanced materials research, which will implement the advantages of new materials and improved modeling techniques.

Additionally, as a part of second level of optimization, ORNL is expanding upon its work in the area of high performance computing and parallel processing, using resources ranging from PC/workstation platforms to computational clusters and ultimately to large-scale supercomputing resources at ORNL. Fabrication and dynamometer testing of full-size prototypes will be carried out when motor designs are ready for prototyping. One proof-of-principle prototype was fabricated in FY 2014. Advanced materials research on the project includes the investigation and development of new materials (e.g., low-loss steel) and/or new processes to facilitate the incorporation of high-efficiency materials in electric motors. Another important part of the materials research effort is the characterization and analysis of electrical steel and other materials used in electric motors. Feedback from these characterizations will help improve the fundamental understanding of electrical steel magnetization and loss characteristics, which are critical for accurate motor modeling and development.

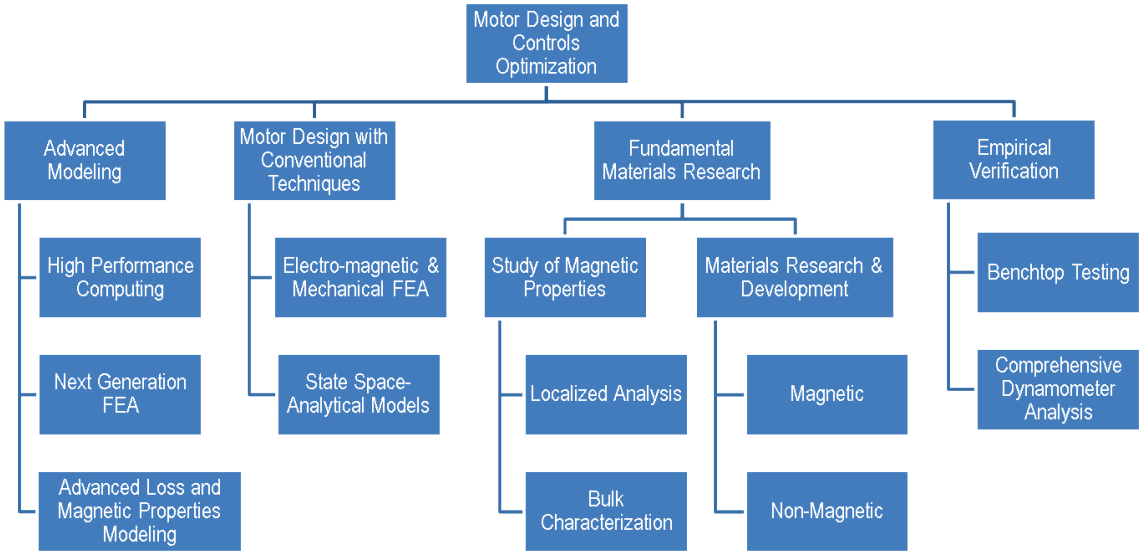

Figure 1: Block diagram of project structure, approach, and technical focus areas.

Results

Motor design optimization in FY 2014 was conducted with commercial FEA packages, in combination with other software packages, for external parametric optimization algorithms as well as state space simulations. The progress and results in the area of motor design are discussed after the following sections describing the parallel efforts in materials R&D. These parallel efforts are ultimately in support of improving motor designs by developing or facilitating the use of more efficient materials and by conducting fundamental research to improve the modeling accuracy of electrical steel characteristics. Findings from this research will begin to be incorporated into new modeling tools in FY 2015.

Materials Research and Development—6.5% Silicon Steel

ORNL is developing ways to facilitate the use of electrical steel with high Si content. Conventional electrical steel has about 2–3% Si content, and there are some expensive products with 6.5% Si content. A higher amount of Si increases resistivity and therefore reduces eddy current and hysteresis losses. The comparison in Figure 2 indicates that an increase from 3% to 6.5% Si yields an average core loss reduction of about 35%. This reduction of core loss is nearly

indirectly proportional to resistance; thus the specific resistance of the 3% Si steel (labeled "Non-oriented SiFe") is about 44% lower than the specific resistance of 6.5% Si (labeled "JNEX-Core"). The loss reduction holds true for the various frequencies and flux density levels indicated.

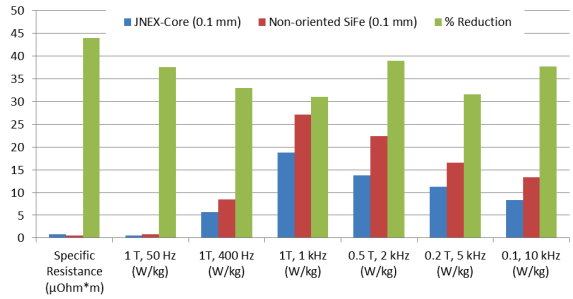

Figure 2: Comparison of electrical steel core losses: 6.5% Si vs 3% Si.

Currently, 6.5% Si is commercially available, but it is expensive because it is made by an intensive CVD process. Silicon steel is rolled into sheets with thicknesses of about 0.1 to 1 mm, depending on application requirements. The CVD process is used because conventional 6.5% Si steel is so brittle that it cannot be rolled and mechanically worked with conventional methods. Therefore, 6.5% Si sheet processing begins with 3% Si sheets, and the CVD process is used to increase the Si content to 6.5%. It remains a challenge to produce motor laminations from conventional 6.5% Si sheet steel since a stamping process is used for mass-produced motors. The brittle 6.5% Si sheet steel is difficult to stamp consistently without undesirable fracturing, and stamping tool lifetime is also reduced because the material is harder.

Research on this project aims to facilitate the production of 6.5% Si sheet steel from ingot form using processing techniques that are similar to conventional methods. Trace elements can be added to enhance strain softening behavior. This phenomenon was confirmed with experimental measurements as samples were prepared with trace amounts of various materials, including boron. Results confirmed that ductility can be recovered during warm rolling, in which certain crystalline phase ordering is destroyed.

In addition to developing methods to produce 6.5% Si from ingots, ORNL is developing processing techniques to facilitate the rolling process, as well as lamination production. This is a critical part of the development, because lamination quality control and tool lifetime are key considerations for motor production. Hardness measurements confirm that ORNL's new processing method softens 6.5% Si to a level similar to the softness of 3% Si without significant modification of conventional processing methods.

Near the end of FY 2014, this effort began to be a joint project with the Propulsion Materials Program of DOE's VTO. Plans for the joint project in FY 2015 include molecular dynamics simulations to determine the impact of various compositions of trace elements, analysis to gain a better understanding of ordering/disordering, and more experimental results to further validate novel processing techniques.

Materials Research and Development—Characterization Of Electrical Steel

Advanced materials characterization was conducted to facilitate improved modeling of magnetization and loss characteristics in conventional electrical steel (~3% Si) and to aid in the development of new materials and processes. A custom magnetic characterization tool was developed to observe localized properties in electrical steel. The measurement stage of the characterization system, shown in Figure 3, includes excitation coils that apply a magnetic field on a single sheet sample as the local magnetic field on the surface of the sample is measured. Conventional motor simulation techniques assume that the material properties are homogeneous for the bulk of the material. However, many things can impact magnetic properties, such as residual stress from stamping or laser cutting. Additionally, stamped or laser-cut edges are near the air gap, which is a critical location for the magnetic circuit and operation of the motor.

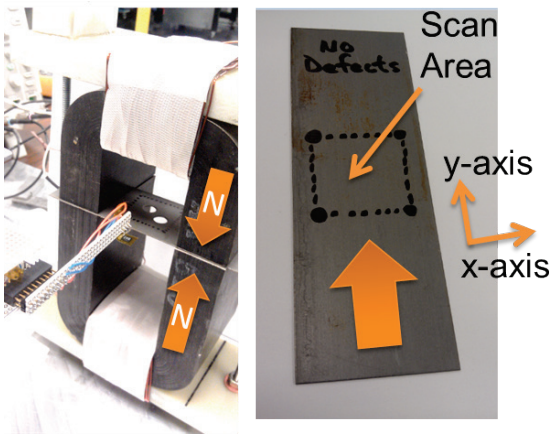

Figure 3: Measurement stage of magnetic characterization system.

This characterization tool provides the capability to observe the correlation between various deformations and disturbances and the non-homogeneity of magnetic properties in a sample. For example, results from scanning an unmodified sample at a flux density of 1.4 Tesla are shown in Figure 4, in which considerable variations in the magnetic field are observed, even in an undisturbed sample.

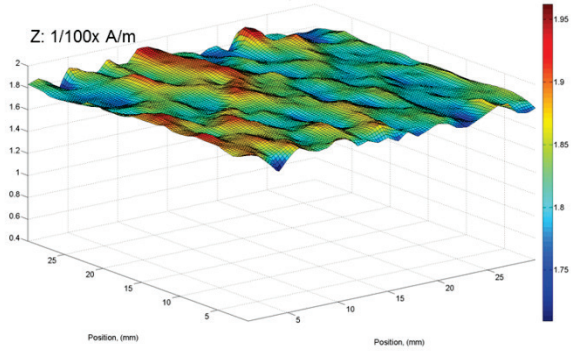

Figure 4: Magnetic field results from unmodified control sample.

The plot in Figure 5 shows the resulting magnetic field with a flux density of 1.4 Tesla after a brief application of laser pulses in five different areas of the sample. Although the disturbed areas are barely visible on the physical sample, five distinct areas are visible in the plot of the scanning results where the magnetic properties are significantly impacted.

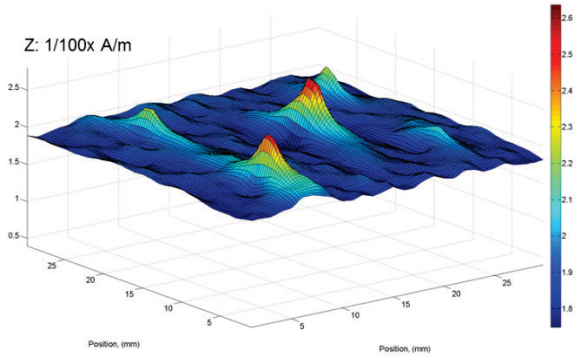

Figure 5: Magnetic field results after brief application of laser pulses.

A more significant deformation was applied to the sample shown on the left in Figure 6, in which two large holes were made with a punching tool. The results, shown on the right, clearly indicate the impact upon the magnetic field—levels of variation near the deformation zone are up to 3.5 times those in undeformed areas of the sample.

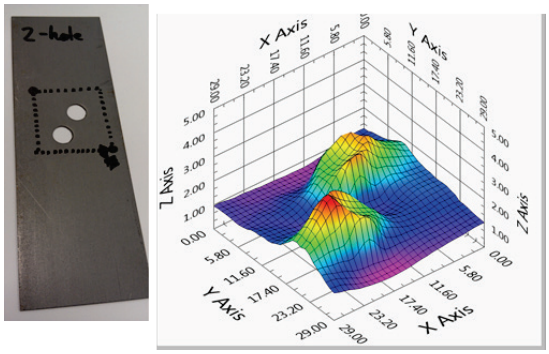

Figure 6: Magnetic field results after punching of two large holes.

Many types of deformations were applied and corresponding analyses were conducted. One of the more interesting and perhaps more meaningful studies in regard to electric motors involved shearing and rejoining a sample, as shown in Figure 7; the magnetic flux was forced across the deformation zone, which extends the entire width of the sample. Researchers were careful not to leave any noticeable air gap between the rejoined pieces, so the nonuniformities in the magnetic field in Figure 7 are due to residual stresses in the material. The magnetic field is up to five times higher at the deformation zone than it is at undisturbed areas of the sample. In other samples, it is more difficult to determine the impact upon permeability because the localized flux density changes across the area of the sample; but in this case, permeability can be more readily determined since the deformation extends across the sample in a direction that is perpendicular to the magnetic flux. Therefore, the local magnetic flux density is also consistent across the sample. Similar results were received regardless of whether the sheared edge or two laser cut edges were joined together. Additionally, short-term annealing of the sample was conducted for 15 minutes at 840°C and no significant changes were noticed in the magnetic field measurements.

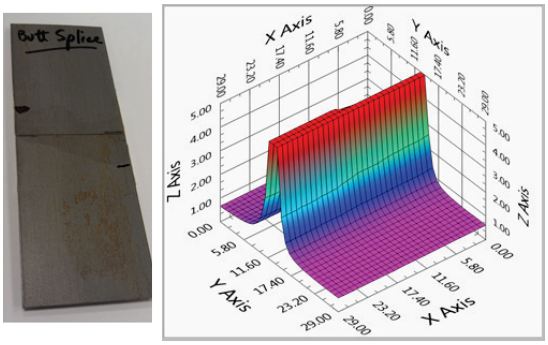

Figure 7: Magnetic field results after shearing and rejoining.

Samples were prepared for analysis with a scanning electron microscope (SEM) to identify the extent of the deformation zone by observing damage to the crystal lattices of the grains within the electrical steel microstructure. A back-scatter analysis method was used to visually represent where damaged areas are located. Normal grains should have a uniform color, as is shown for many of the grains on the left in Figure 8. However, near the edge (which is the point of deformation by laser cutting), discoloration within the grains is noticeable. This discoloration directly correlates with the amount of deformation within the grain. The image on the right in Figure 8 shows the amount of deformation: blue grains indicate normal undisturbed lattice, and green, yellow, and red coloration indicates the level of damage and dislocations within the lattices of the grains. A qualitative value of intra-grain stress can be determined by observing the misorientation spread, which is directly associated with the deformation within each grain. The graph in Figure 9 shows the misorientation spread vs the distance away from the laser cut edge (into the sample). According to this technique, the intra-grain residual stress reaches nominal levels within 150 µm.

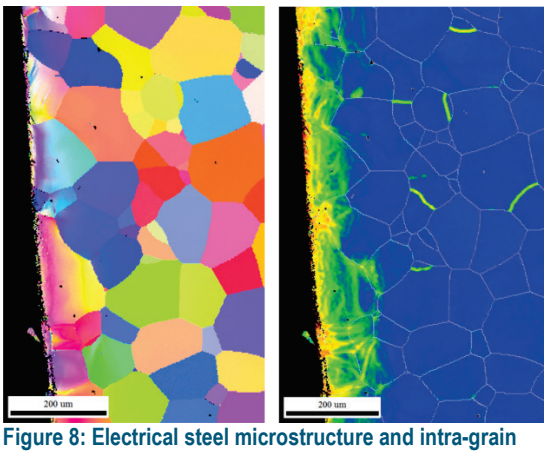

Figure 8: Electrical steel microstructure and intra-grain residual stress.

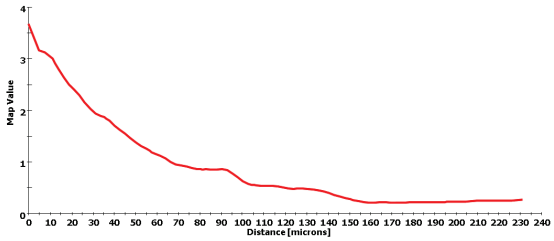

Figure 9: Misorientation spread representing residual stress within grains versus distance from cut edge.

It is important to realize that this technique provides a qualitative measure of intra-grain residual stress, but it does not include stresses that occur between the grains. Even if intra-grain stress is the only contributor to reduced magnetic performance, it is easy to see how it could impact electric motor operation, considering that air gaps in electric motors are on the order of 500 to 1000 µm. In comparing these results with findings from the magnetic characterization tool, where impacts upon magnetic properties are found to be on the order of millimeters, it appears that much of the degradation is caused by residual stress that is maintained at and throughout grain boundaries.

Magnetic domains were observed with a magnetic force microscope in the same samples and deformation areas that were observed with the SEM. To begin to identify correlations between deformation and magnetic domain behavior, domain images were superimposed on the deformation images, as shown in Figure 10. Domain behavior should be somewhat consistent within an undisturbed grain, but it is clear that the behavior within the deformation zone is not very consistent. This phenomenon is more noticeable in Figure 11, where magnetic domain patterns are more consistent within grains away from severe deformation zones, and patterns are more erratic near the edges of the sample. The patterns shown in Figure 12 indicate the rough correlation between magnetic domain pattern and crystal lattice orientation in undamaged grains. There is some variance, but the orientations of the magnetic domains correlate with the lattice structure. Although these observations are mostly qualitative, they are key indicators of the impacts of residual stress upon magnetic characteristics. Furthermore, techniques are being implemented to quantitatively determine magnetic properties through domain observation.

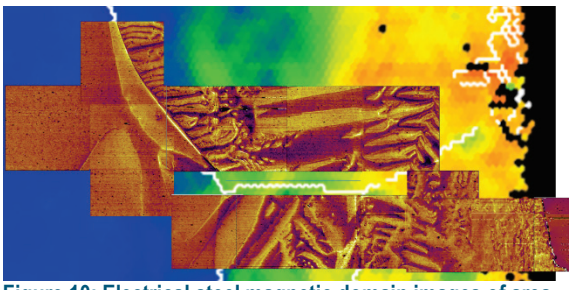

Figure 10: Electrical steel magnetic domain images of area near damage zone.

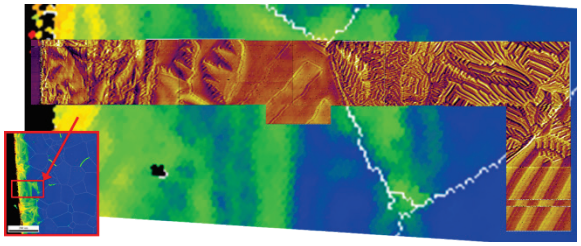

Figure 11: Electrical steel magnetic domain images of area near damage zone.

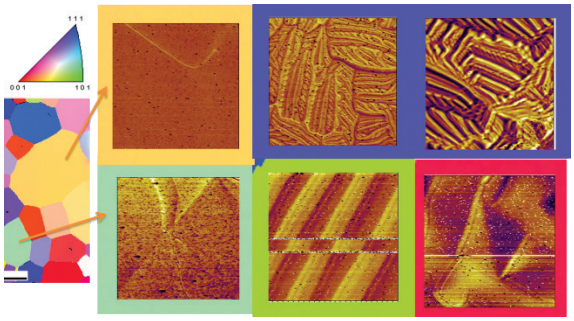

Figure 12: Association between crystal lattice and magnetic domains.

Materials Research and Development —Modeling of Electrical Steel

The fundamental behavior of magnetic domains in non-oriented Si steel is an area that has not been thoroughly explored or defined. Monte Carlo (MC) simulations are being conducted to examine some of these fundamental behaviors, and ultimately feedback will be provided for models that are being developed on a much larger scale. In ferromagnetic materials, the interaction energy between the magnetic moments is given by the following micro-magnetics equations.

$$E_{ext} = -H.M \quad [1]$$

$$E_{exch} = J_1 \sum_{n1=1}^{6} Ma_i a_{n1} + J_2 \sum_{n2=1}^{6} Ma_i a_{n2} + J_3 \sum_{n3=1}^{12} Ma_i a_{n3} + J_4 \sum_{n4=1}^{6} Ma_i a_{n4} \quad [2]$$

$$E_{dip} = M^2 \sum_{j=1}^{n} \sum_{k \neq j}^{n} \frac{(a_i a_k - 3a_j e_{jk} a_k e_{jk})}{4\pi\mu_0 r^3} \quad [3]$$

$$E_{an} = K_1(a_1^2 a_2^2 + a_2^2 a_3^2 + a_1^2 a_3^2) + K_2 a_1^2 a_2^2 a_3^2 \quad [4]$$

In Eq. (1), *H* is the external magnetic field strength, *M* is the magnetic moment of the atoms in the crystal, and E_{ext} is the energy due to the presence of the external field. According to Eq.(1), the energy is minimized when the magnetic moments are parallel to the magnetic field. In Eq. (2), E_{exch} is the spin exchange energy for each atom *i* where a_i is the magnetic moment vector of each atom and a_{n1} to a_{n4} are the magnetic moment vectors of atoms in the first through the fourth nearest neighbors of the atoms. J_1 through J_4 are the exchange coefficients. In the present work, exchange

coefficients were used that correctly reproduce the Curie temperature of BCC iron.

The spin exchange energy is responsible for the spontaneous magnetization of ferromagnetic materials. In Eq. (3), E_{dip} is the dipole-dipole interaction energy where *a*'s are the magnetic moment vectors, e_{jk} is the unit vector of the displacement that connects an atom *i* with atom *k*, and μ_0 is the permeability of space. The formation of the magnetic domains is due to a balance between E_{exch} and E_{dip}. When the particle size is small, the E_{exch} contribution dominates and the entire particle exists as a single domain. As the particle size increases, the contribution from E_{dip} increases. E_{dip} specifically increases at the surfaces normal to the moments. This is the origin of the demagnetizing field that raises the system energy. This allows for the moments to align in directions away from those dictated by E_{exch}, resulting in the formation of various types of domains separated by the domain boundary.

In the current MC simulations, the total system Hamiltonian is the sum of these four energy contributions. The simulation domain is aligned with the global x, y, and z directions. The simulation volume can be a single crystal, a bicrystal, or a polycrystal. The local direction within each grain is defined by three Euler angles, ψ, θ, and ϕ. The magnetic moment vectors for sites within each grain are defined with respect to the local grain orientation. The MC move is a random rotation attempt of the magnetic moment of a randomly picked single atom keeping the orientation of the particle constant. The change in energy ΔE is calculated and the move is accepted with a probability of $\exp(-\Delta E/kT)$ when $\Delta E > 0.0$ and 1.0 when $\Delta E \leq 0.0$. The system size was scaled by replacing the atoms in the BCC crystal structure by a collection of BCC unit cells placed in a BCC arrangement. By computing the exchange energy as a function of the size of the lattice site, it was shown that the scaling factor for the exchange energy K_{exch} followed the empirical equation

$$K_{exch} = 6.810 - 11.587\,K_{size} + 5.776\,K_{size}^2 \quad [5]$$

where K_{size} is the size factor. The effective lattice parameter due to scaling, LP_{size} is given by

$$LP_{size} = LP_1 2^{K_{size}-1} \quad [6]$$

where *LP* is the lattice parameter of the BCC unit cell. The effective magnetic moment at each lattice site, a_{size}, in the scaled lattice is given by

$$a_{size} = \begin{cases} a & K_{size} = 1 \\ 2a & K_{size} = 2 \\ 2a2^{3(K_{size}-2)} & K_{size} > 2 \end{cases} \quad [7]$$

Figure 13 shows the grain structure with superimposed tangent vectors of the magnetic domain in a random x, y, and z plane. The image on the left shows the magnetic moment vectors in the absence of external field. The image at the right shows the magnetic moments in the presence of a 0.25 T magnetic field in the z direction.

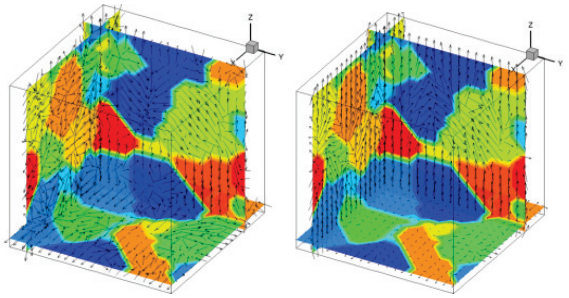

Figure 13: Three-dimensional grain structure with magnetic moment vectors indicating random orientation without magnetic field (left) and alignment with magnetic field (right).

It is clear that the application of the magnetic field causes some alignment of the magnetic moments, although the alignment is not very effective in certain grains. This indicates that the magnetic field intensity required to align the moments depends on the local grain orientation, which is well known.

Figure 14 shows the same simulation results as in Figure 13 but with the grain structure replaced by the magnetic domains obtained by a contour plot based on one of the direction cosines of the magnetic moment vector. These plots help with the visualization of magnetic domain growth as external fields are applied.

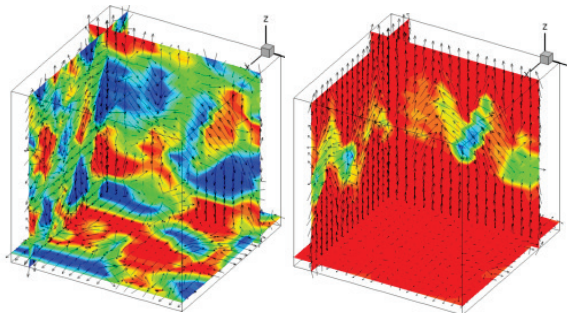

Figure 14: Domain structure and magnetic moment vectors from polycrystalline simulations without magnetic field (left) and the growth of the domains with external field (right).

The MC simulations are able to minimize the total energy of the system by reorienting the magnetic moments. Figures 15 and 16 show the total energy and the relative magnetization, respectively, as functions of the simulation time. The total magnetization in the absence of the field is negligible, although there is a clear indication of magnetic domains within the grain structure as shown in Figure 14. However, application of the 0.25 T field has a significant effect on the magnetization, which relates to the unbalanced domain structure shown in Figure 14. The graph in Figure 15 shows that the total energy of the system decreases with simulation steps, although with the magnetic field, the reduction is much higher as a result of the contribution from Eq. (1).

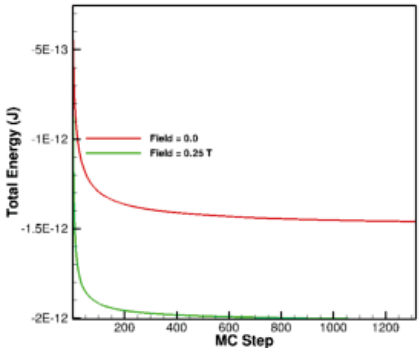

Figure 15: Total energy as a function of the MC simulation step with or without a superimposed 0.25 T field in the z-direction.

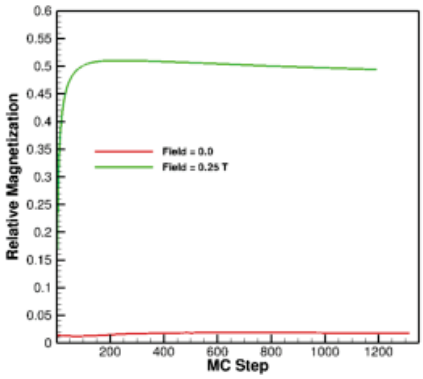

Figure 16: Relative magnetization as a function of the MC simulation step with or without a superimposed 0.25 T field in the z-direction.

Motor Design and Modeling

The development of unconventional motor technologies was accomplished by improvising upon promising technologies from previous work and initiating work on novel motor concepts. Previous research includes the design of various motor types, including the induction motor, switched reluctance motor, hybrid excitation motor, and flux coupling/field coil machines, with the latter two displaying the most potential. Novel motor designs were conceived and simulated, with consideration of various machine types such as switched reluctance, hybrid PM excitation, synchronous reluctance, and field coil excitation.

ORNL used advanced optimization algorithms to optimize machine design and controls. Electromagnetic FEA tools were used to implement basic models to determine performance and operational characteristics of new machine designs. Analytical models were used to determine additional performance metrics and associated control methods. A BFE motor without PMs, shown in Figures 17 and 18, was developed during a previous research project at ORNL. The motor includes auxiliary coils that provide a magnetic field similar to what PMs provide in conventional PM motors. A new design was developed in FY 2014 in which the excitation coils are integrated more effectively with the primary motor components, thereby greatly reducing the volume of the auxiliary coils. Among many design choices, another leading ORNL design is a novel type of sinusoidally driven synchronous reluctance (SDSR) motor. Unlike switched reluctance motors, SDSR motors can be driven by a conventional three-phase inverter and have much less torque ripple.

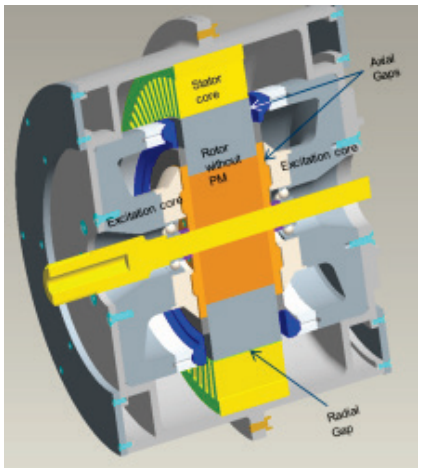

Figure 17: First-generation BFE cross-section overview.

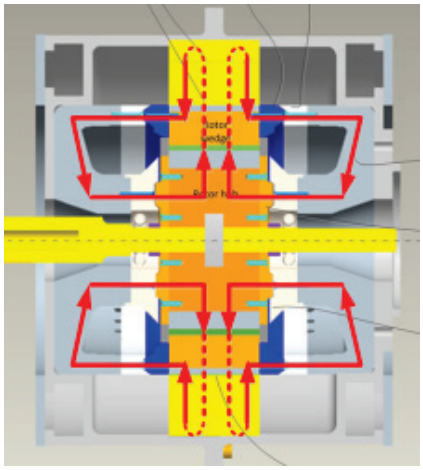

Figure 18: First-generation BFE cross-section side view.

Performance results for the new BFE and SDSR motor designs are summarized in Figures 19 and 20. In Figure 19, the peak torque operation curves of the BFE and SDSR ("SyncRel") are compared with that of the 2010 Prius. To facilitate straightforward comparisons, the BFE and SDSR motors were designed so that they occupy the same volume as the 2010 Prius. It can be seen that the torque production capability of the SDSR is only slightly lower than that of the Prius, and the BFE peak torque production is just slightly lower than that of the SDSR. A more clear comparison can be made by observing the peak power capability shown in Figure 20. Note that these performance characteristics represent designs that have been only coarsely optimized. Therefore, the slight performance discrepancy from that of the 2010 Prius is reassuring, especially in light of the absence of PMs. Detailed design optimizations in FY 2015 will yield higher performance.

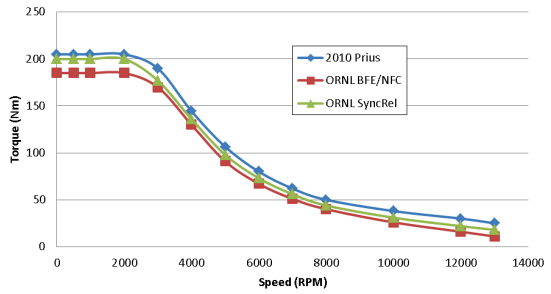

Figure 19: Comparison of simulated peak torque of various machines.

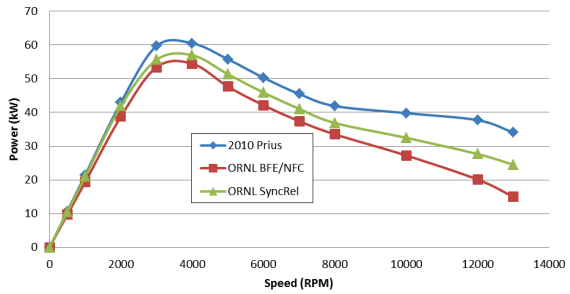

Figure 20: Comparison of simulated peak power of various machines.

The peak torque and power performance of the new BFE design is lower than that of the Prius and SDSR largely because of the additional current that is required for the field winding. Compounding the matter is the requirement that the field cross two additional air gaps in addition to the two crossings experienced in conventional electric motors. This inherently reduces the power density, specific power, and efficiency of the BFE design in comparison with a conventional PM motor. The simulated efficiency map of the BFE design with the highest field excitation current is shown in Figure 21.

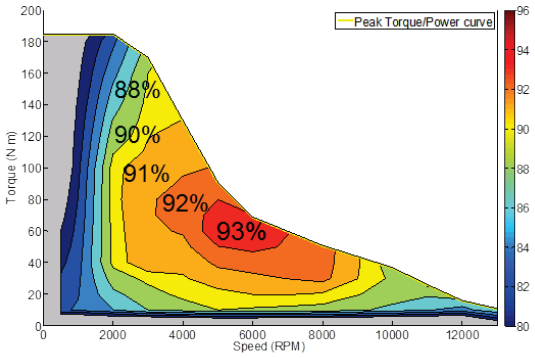

Figure 21: Simulated efficiency map for 2nd generation BFE with high field excitation level.

Simulated efficiency maps for medium-high, low-medium, and low field excitation levels are shown in Figures 22 and 23. Although the peak efficiency and overall efficiency levels of the BFE design are lower than those of the Prius and SDSR motors, the adjustable field level has the effect of shifting the operation region in which the peak efficiency occurs. For example, the motor efficiency at 2000 rpm and 10 Nm is about 87% for high auxiliary field excitation currents. For low field excitation currents, shown in Figure 23, the efficiency is above 91%, compared with an efficiency of about 88% for the Prius at the same operation point. PMs have high residual fields even at low and moderate operation points where the high fields are not required, and so the core losses associated with these residual fields can yield low efficiencies for these regions. Some motors without PMs may have higher efficiencies than PM motors at low and moderate loads and high speeds as a result of this phenomenon.

The addition of auxiliary field control increases the potential for higher efficiencies at low and moderate loads and high speeds. This is particularly important because low and moderate operation points are frequented throughout common driving cycles, as shown in Figure 24. These data, recorded by Argonne National Laboratory, indicate the tractive force vs vehicle speed associated with various driving cycles for the Nissan LEAF. This is a direct drive powertrain, so the operation map directly relates to the torque vs speed efficiency maps that were just discussed. It can be seen that low-efficiency regions of the PM machine are encountered frequently for all drive cycles. This phenomenon highlights the potential for non-PM and adjustable field motors to have higher overall efficiencies than PM motors, as efficiency is averaged over the entire drive cycle.

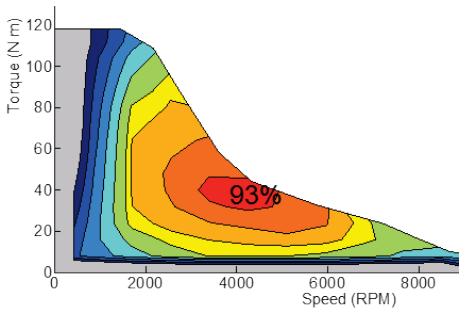

Figure 22: Simulated efficiency map for second-generation BFE with medium-high field excitation level.

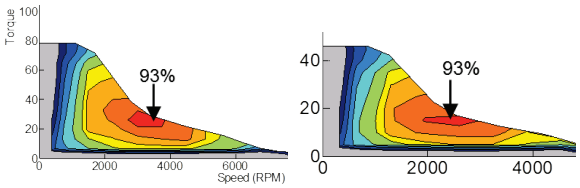

Figure 23: Simulated efficiency map for second-generation BFE with low-medium (left) and low (right) field excitation levels.

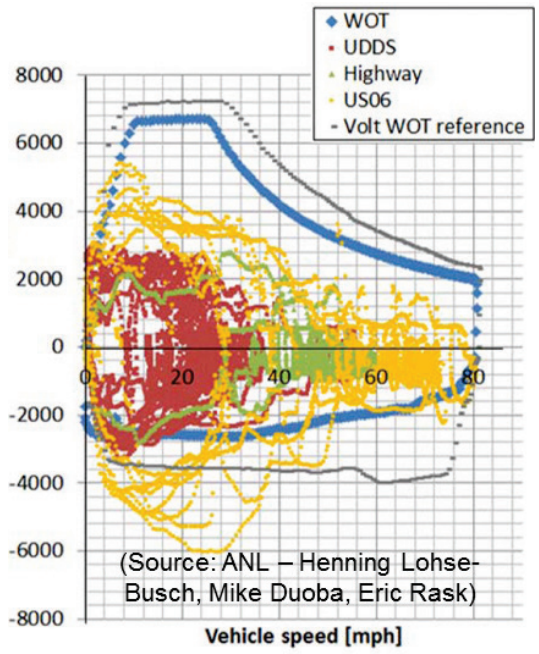

Figure 24: Required tractive force for Nissan LEAF measured for various drive cycles.

After coarse optimizations were performed on several designs that were validated in preliminary simulations, the design with the highest potential for success was selected for fabrication. The SDSR motor was selected based on its potential for higher power density and specific power and its simplicity of fabrication and assembly. Invention disclosures are being filed so details of the design can be discussed in the future. Fabrication and assembly of the novel SDSR was completed in FY 2014; images of the proof-of-principle prototype are shown in Figure 25. Unforeseen difficulties often arise during fabrication and assembly prototype motors, but the assembly process of the SDSR motor was accomplished without significant difficultly, which is a positive sign for manufacturability.

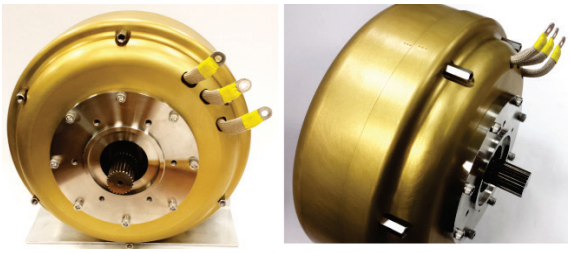

Figure 25: Proof-of-principle prototype assembly of novel synchronous reluctance motor.

Conclusions and Future Directions

Electrical steel with 6.5% Si has about 35% lower core losses than conventional electrical steel with 2–3% Si; therefore, the use of high-Si steel can increase peak motor efficiency by up to 2–5% and increase efficiency in other operation regions by 5–15%, particularly at high speeds. ORNL confirmed proposed methods and developed additional techniques to facilitate low-cost production of 6.5% Si sheet steel. A key factor in making it feasible to use 6.5% Si sheet steel for motor laminations is the implementation of softening techniques that allow the sheets to be rolled to the appropriate thicknesses and the laminations to be stamped. It is most common for the rolling operation to be carried out by the steel manufacturer, while stamping and other related processes are carried out by the motor manufacturer. ORNL's proposed methods address the need for two separate processing locations. These methods have been confirmed in simulations and with hardness testing on small samples. Future work on 6.5% Si steel will include simulations to determine the impacts of various compositions of trace elements, analysis to gain a better understanding of ordering (which causes brittleness), and more experimental analysis to further validate novel processing techniques.

Characterization of the impact of residual stress upon magnetic properties has revealed significant degradation near areas that have sustained mechanical deformation. The primary reason for interest in this phenomenon is to increase the understanding and model the impact of residual stress upon magnetization and core losses. An MC simulation environment has been developed to study the fundamental behavior and determine how a wide range of variables can impact the magnetization and loss mechanisms in electrical steel. A custom characterization system has been developed to perform large-scale assessments of these behaviors, and implementation of a system to perform detailed analyses on the magnetic domain scale is under way. These systems not only will help with the analysis of the impact of residual stress but also will advance the understanding of other factors that impact magnetization and loss behavior, such as rotational losses and the impact of pulse width modulation excitation. These areas will be included in efforts for FY 2015.

Motor modeling tools are under development to include the phenomena related to the advanced characterizations mentioned. When possible, advanced techniques will be implemented with commercial FEA packages and detailed optimization will be conducted with leading motor designs. Additionally, characterization of the proof-of-principle prototype will serve as an important feedback mechanism for model verification.

FY 2014 Publications/Presentations

[1] T. Burress, "Scalable non-–rare earth motor development," presented at the DOE VTO APEEM Kickoff Meeting, November 2013.

[2] T. Burress, "Scalable non–rare earth motors," presented at the DOE VTO Annual Merit Review and Peer Evaluation Meeting, June 2014.

[3] T. Burress, "Electric motor research for electric vehicles," presented at the IEEE Energy Conversion Congress and Exposition, September 2014.